(12) INTERNATIONAL APPLICATION PUBLISHED UNDER THE PATENT COOPERATION TREATY (PCT)

(19) World Intellectual Property Organization
International Bureau

(43) International Publication Date
29 July 2010 (29.07.2010)

PCT

(10) International Publication Number
WO 2010/085348 A1

(51) International Patent Classification:
A61B 5/00 (2006.01)

(21) International Application Number:
PCT/US2010/000166

(22) International Filing Date:
22 January 2010 (22.01.2010)

(25) Filing Language: English

(26) Publication Language: English

(30) Priority Data:
61/147,074 23 January 2009 (23.01.2009) US

(72) Inventor; and
(71) Applicant : **PERELMAN, Lev, T.** [US/US]; 68 Monmouth Street, Brookline, MA 02446 (US).

(74) Agent: **MORRIS, James, H.**; Wolf, Greenfield & Sacks, P.C., 600 Atlantic Avenue, Boston, MA 02210-2206 (US).

(81) Designated States *(unless otherwise indicated, for every kind of national protection available)*: AE, AG, AL, AM, AO, AT, AU, AZ, BA, BB, BG, BH, BR, BW, BY, BZ, CA, CH, CL, CN, CO, CR, CU, CZ, DE, DK, DM, DO, DZ, EC, EE, EG, ES, FI, GB, GD, GE, GH, GM, GT, HN, HR, HU, ID, IL, IN, IS, JP, KE, KG, KM, KN, KP, KR, KZ, LA, LC, LK, LR, LS, LT, LU, LY, MA, MD, ME, MG, MK, MN, MW, MX, MY, MZ, NA, NG, NI, NO, NZ, OM, PE, PG, PH, PL, PT, RO, RS, RU, SC, SD, SE, SG, SK, SL, SM, ST, SV, SY, TH, TJ, TM, TN, TR, TT, TZ, UA, UG, US, UZ, VC, VN, ZA, ZM, ZW.

(84) Designated States *(unless otherwise indicated, for every kind of regional protection available)*: ARIPO (BW, GH, GM, KE, LS, MW, MZ, NA, SD, SL, SZ, TZ, UG, ZM, ZW), Eurasian (AM, AZ, BY, KG, KZ, MD, RU, TJ, TM), European (AT, BE, BG, CH, CY, CZ, DE, DK, EE, ES, FI, FR, GB, GR, HR, HU, IE, IS, IT, LT, LU, LV, MC, MK, MT, NL, NO, PL, PT, RO, SE, SI, SK, SM, TR), OAPI (BF, BJ, CF, CG, CI, CM, GA, GN, GQ, GW, ML, MR, NE, SN, TD, TG).

Published:

— *with international search report (Art. 21(3))*

WO 2010/085348 A1

(54) Title: ENDOSCOPIC POLARIZED MULTISPECTRAL LIGHT SCATTERING SCANNING METHOD

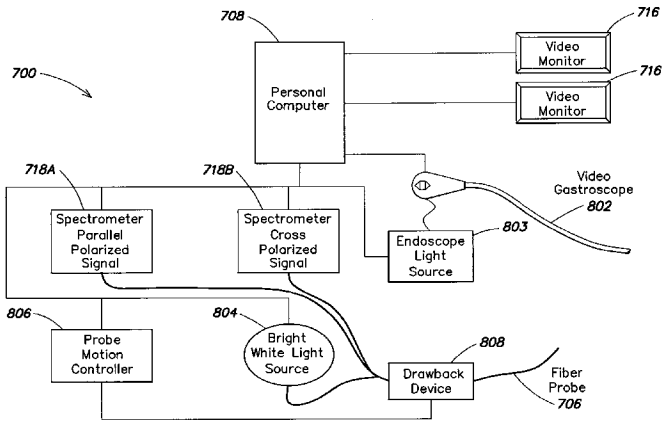

FIG. 8

(57) Abstract: Method and system for early detection of precancerous and other abnormal changes in tissue of various organs. The system comprises a combination of endoscopic scanning with light scattering spectroscopy and improves detection of abnormalities that may otherwise remain undetected. The system may include a probe that collects data of quality that is independent of a distance of the probe from the scanned tissue. During endoscopy, tissue of an organ is imaged using polarized multispectral light scattering scanning and results are presented to a user in a manner that allows detecting abnormal morphological and biochemical changes in the tissue. A determination of whether to perform biopsy may be performed while the endoscopy is being performed, which thus provides guided biopsy. An entire surface of the organ may be rapidly scanned and results of the scanning are analyzed with a reduced time delay.

ENDOSCOPIC POLARIZED MULTISPECTRAL LIGHT SCATTERING SCANNING METHOD

RELATED APPLICATIONS

This application claims the benefit under 35 U.S.C. § 119(e) of U.S. provisional application 61/147,074, filed January 23, 2009, entitled "POLARIZED LSS ENDOSCOPIC SCANNING INSTRUMENT," the content of which is incorporated herein in its entirety.

FIELD OF THE INVENTION

The present invention relates to imaging tissue of an organ using polarized multispectral light scattering scanning method to detect abnormal morphological and biochemical changes indicative of precancerous dysplasia or other tissue abnormalities.

BACKGROUND

Early detection of precancerous changes in various organs in the human body may improve results of treatment and ultimately save lives. Techniques used to detect such changes include visual endoscopy and collection of tissue samples (i.e., biopsy) at predetermined sites that are typically used to analyze tissue of organs for abnormal changes.

As an example, tissue of the esophagus may be examined using light scattering spectroscopy. Esophageal adenocarcinoma is a form of cancer the incidence of which is increasing rapidly in the United States. Almost 100% of cases of esophageal adenocarcinoma occur in patients with Barrett's Esophagus (BE), an otherwise benign condition in which metaplastic columnar epithelium replaces the normal squamous epithelium of the esophagus.

Although the prognosis of patients diagnosed with adenocarcinoma may be poor, the chances of successful treatment increase significantly if the disease is detected at the dysplastic stage. Once BE has been identified in a patient, the patient may be enrolled in an endoscopy/biopsy surveillance program, presuming that the patient is a candidate for surgery should high-grade dysplasia be detected. The surveillance of patients with BE for dysplasia may be challenging in at least three respects. First, dysplasia may not be visible during routine endoscopy. Thus, known testing techniques often require that numerous biopsy specimens be taken at random locations along the patient's esophagus for histopathologic examination of the excised tissue. Second, the histopathologic diagnosis of dysplasia is problematic because there

is poor interobserver agreement on the classification of a particular specimen, even among expert gastrointestinal pathologists. Third, reliance on the histopathologic examination imposes a time delay between endoscopy and diagnosis, which may severely limit the diagnostic accuracy of the endoscopic procedure.

SUMMARY OF INVENTION

Applicants have appreciated that techniques of detecting changes in tissue of an organ may be improved by employing multispectral light scattering scanning method together with endoscopy. The multispectral light scattering scanning may be used to collect data on one or more portions, or sites, of the organ and use the data to determine whether there are any changes in the tissue of the organ that may be indicative of a precancerous or other abnormal condition. In some embodiments, polarized multispectral light scattering scanning method is employed.

Embodiments of the invention provide a method that may be used to perform rapid optical scanning and multispectral imaging of the entire surface of the organ. Both internal and external surface of the organ may be scanned. The analysis of the data collected while scanning the surface of the organ may allow detecting otherwise invisible changes one or more portions of the organ affected by a certain degree of dysplasia. Thus, suspicious sites where a biopsy is desired to be taken for further analysis may be identified. Accordingly, the method may be used to guide the biopsy and sample of the tissue may be collected from the suspicious sites while the scanning is being performed.

Embodiments of the invention may enable fast and reliable spectroscopic detection and diagnosis of dysplasia in patients with BE during endoscopy. Exemplary embodiments may provide an instrument and method for safely, quickly, and reliably surveying the entire length of Barrett's esophagus for endoscopically invisible dysplasia, thereby avoiding harms and risks associated with random biopsy surveillance.

According to one aspect of the present invention, an instrument, method and system for examination of internal tissue using polarized light scattering spectroscopy (PLSS) is described. In one embodiment, an instrument is described that can be used to detect various conditions in esophageal tissue including, but not limited to: Barrett's esophagus (BE), low-grade dysplasia (LGD), high-grade dysplasia (HGD), and/or adenocarcinoma. The described instrument may be able to distinguish between various tissue conditions. The instrument may be used to examine gastrointestinal tissue *in vivo* and/or *ex vivo*.

In some embodiments, the instrument may permit non-contact scanning over regions of gastrointestinal tissue. The described instrument may be used to obtain data at spatially separated tissue locations, along a line and/or over a two-dimensional area, as the invention is not limited in this respect.

In one embodiment, an instrument includes a light scattering spectroscopy (LSS) probe configured to be inserted into the gastrointestinal tract of a patient. The probe includes illumination optics for illuminating tissue, and receiving optics for receiving light scattered by the tissue to be directed to one or more spectrometers. The illumination optics may be configured for illuminating tissue with collimated light and the receiving optics may be configured to collimate received light. A portion of the received light with a certain angular distribution may be collected. The probe may also include a polarizer for polarizing light scattered by the tissue. The probe may include a scanning assembly configured to move at least some of the illumination optics with respect to a non-scanning portion of the probe/and or with respect to a gastroscope. At least some of the illumination optics may rotate, tilt, pivot and/or translate with respect to the non-scanning portion of the probe and/or the gastroscope.

In one embodiment, an LSS instrument includes an LSS probe and one or more spectrometers for generating a spectrum of scattered light received by probe. The instrument may further include a control unit for controlling a direction of the illuminating beam from the polarizer. The control unit may interact with a scanning assembly of the probe to scan illuminating and/or receiving optics of the LSS probe.

According to another aspect of the invention, a method and system for obtaining diagnostic information from polarized LSS data of tissue is provided. The described method may be used to provide diagnostic information corresponding to separate tissue locations, corresponding to tissue located along a line and/or corresponding to tissue over a two-dimensional area, as the invention is not limited in this respect. The described system may be used to analyze spectral data obtained from one or more tissue locations *in vivo* or from tissue samples *ex vivo* to produce data indicating a diagnostic condition at each tissue location. The described system may be used to obtain a real-time map of a diagnostic condition over an area of tissue during an endoscopy. Thus, an entire surface of the organ may be rapidly scanned and results of the scanning are analyzed with a reduced time delay. The system may also include an imaging system for providing an image of the tissue during an endoscopy. The system may enable biopsies at locations where a certain tissue condition has been identified or is suspected

based on a map of nuclear tissue structure and/or a map of a diagnostic condition obtained by LSS. A map of nuclear tissue structure and/or a map of a diagnostic condition may be displayed along with an image of the same location during an endoscopy.

In one embodiment, a method is described that can be used to identify a tissue condition at various tissue locations during a procedure before a probe is removed from a patient. The described method may include providing information regarding a diagnostic condition over a two-dimensional area based on data obtained from an *in vivo* LSS instrument. The method may further include providing a two-dimensional map of a diagnostic condition and two dimensional image of an area of tissue.

Some embodiments of the invention provide a system for obtaining characteristics of tissue of an organ. The system may comprise a device such as a probe configured to scan the tissue of the organ, which may comprise an illumination optics system configured to illuminate at least one portion of the tissue of the organ with collimated light and a receiving system configured to receive light backscattered by at least one portion as a result of the illumination. The system may also comprise at least one spectrometer configured to generate at least one spectrum from the received light, an imaging unit configured to obtain at least one image of the at least one portion, an analysis unit configured to analyze the at least one spectrum to provide at least one characteristic of the at least one portion, and a user interface configured to present to a user information comprising the at least one image in association with at least one visual representation of the at least one characteristic, wherein the information is used to determine whether to take a tissue sample from the at least one portion.

BRIEF DESCRIPTION OF DRAWINGS

In the figures, each identical or nearly identical component that is illustrated in various figures is represented by a single reference character. For purposes of clarity, not every component is labeled in every figure, nor is every component of each embodiment or aspect of the invention shown where illustration is not necessary to allow those of ordinary skill in the art to understand the invention.

For purposes of clarity, not every component may be labeled in every drawing. In the drawings:

FIG. 1 is a schematic diagram of the proof-of-principle system used to perform LSS, in accordance with some embodiments of the invention;

FIG. 2 is a graph of typical Barrett's Esophagus (BE) nuclear size distributions for a non-dysplastic site (solid line) and a dysplastic site (dashed line) extracted using a light scattering spectroscopy (LSS) technique;

FIG. 3 is a graph of a reflectance spectrum of a nondysplastic BE site showing experimental data (solid line) and a model fit to the experimental data (dashed line),;

FIG. 4A is a graph of a reduced scattering coefficient as a function of wavelength for a representative nondysplastic BE site (solid line) and a corresponding linear fit (dashed line),;

FIG. 4B is a graph of slope and intercept obtained from a linear fit to wavelength-dependent tissue reduced scattering coefficients, μ_s', for nondysplastic (squares), low-grade dysplastic (solid diamonds), and high-grade dysplastic (circles) BE sites displayed on a log-log scale;

FIG. 5A is a graph of a spectrum of a polarized component of back scattered light from normal intestinal cells;

FIG. 5B is a graph of a spectrum of a polarized component of back scattered light from T84 intestinal malignant cells;

FIG. 5C is a graph of nuclear size distributions obtained from the spectra shown in Figs. 5A and 5B, where the distributions extracted from the LSS data are shown with solid lines and the distributions measured using light microscopy are shown with dashed lines;

FIG. 6 illustrates an LSS diagnostic plot of Barrett's esophagus (BE) data including: nondysplastic BE (NDB–circles); indefinite for dysplasia (IND–squares); low-grade dysplasia (LGD–triangles) high-grade dysplasia (HGD–diamonds); and an exemplary decision threshold for dysplasia (line), in accordance with some aspects of the invention;

FIG. 7 illustrates a polarized LSS endoscopic polarized scanning spectroscopic instrument (EPSS) in accordance with an embodiment of the invention;

FIG. 8 is a schematic block diagram of an EPSS system in accordance with some aspects of the invention;

FIG. 9 is a schematic perspective view of a portion of a scanning polarization probe in accordance with aspects of the invention;

FIG. 10 illustrates components of a control unit for a probe in accordance with some aspects of the invention.;

FIG. 11 illustrates a scanning polarization probe and control unit in accordance with aspects of the invention;

FIG. 12 illustrates a user interface for an endoscopic polarized scanning spectroscopic (EPSS) instrument, in accordance with other aspects of the invention;

FIG. 13 illustrates a user interface having parameters, which are extracted from data using a histographic algorithm relating tissue structure and or a tissue condition to LSS data, and that are presented in the form of pseudocolor maps overlaid on a video image of Barrett's esophagus (BE);

FIG. 14A illustrates a perspective view of a probe inserted through an instrument channel of a gastroscope (scope) with a tip of the probe extending approximately 2 cm from a distal end of the scope;

FIG. 14B illustrates the probe of Figure 14A forming a 2 mm diameter spot on a flat surface;

FIG. 15A schematically depicts an endoscope in the esophagus near the lower esophageal sphincter (LES) and a corresponding simulated view through the endoscope;

FIG. 15B schematically depicts a probe of the endoscope depicted in Fig. 15A advanced to a starting location of a scan and a corresponding simulated view through the endoscope where a white cone illustrates illumination by a light beam of the probe;

FIG. 15C schematically depicts a location of a beam of the probe at completion of the scan and a corresponding simulated view through the endoscope;

FIG. 15C schematically depicts a forceps biopsy guided by the optical probe and a corresponding simulated view through the endoscope;

FIG. 16 is a flowchart illustrating an endoscopic procedure using of a EPSS instrument, in accordance with some embodiments of the invention;

FIGs. 17A and 17B illustrate results of EPSS scanning of esophageal epithelium during screening endoscopy, n accordance with one embodiment of the invention;

FIGs. 18A and 18B illustrate spectra acquired during routine screening endoscopy, in accordance with one embodiment of the invention;

FIG. 19A illustrates EPSS maps comprising biopsy sites and pathology for subjects A through E, in accordance with one embodiment of the invention;

FIG. 19B illustrates biopsies taken during the initial and follow-up endoscopy procedures for subject A, overlaid on the EPSS map acquired during the initial procedure, in accordance with one embodiment of the invention; and

FIG. 20 illustrates an image of a location with invisible high-grade dysplasia (HGD) obtained using a high resolution endoscope (HRE) with Narrow Band Imaging (NBI), in accordance with one embodiment of the invention.

DETAILED DESCRIPTION

Embodiments of the invention provide a system and a method of detecting abnormal changes in tissues of organs using a combination of light scattering spectroscopy (LSS) with endoscopy. Employing a probe for performing the light scattering spectroscopy with either existing or specifically designed endoscopic devices results in improved detection of abnormalities in the tissues of organs that may otherwise remain undetected. In particular, this technique may improve early detection of certain morphological and histological changes which, albeit being potentially precancerous, may be amenable to treatments if detected early. Thus, lives of many patients may potentially be saved.

Some embodiments of the invention provide techniques for early detection of changes in the tissue of the esophagus that may be initial stages of the esophageal adenocarcinoma. Thus, in accordance with one aspect of the present invention, instruments, systems and methods for examining a portion of the gastrointestinal tract of a patient that is suspected to have Barrett's Esophagus (BE) using LSS are provided. However, embodiments of the invention are not limited to esophagus of any other organ of the gastrointestinal tract and may be applied to detection of abnormal changes is various organs of reproductive tract, respiratory tract and other systems.

A system in accordance with some embodiments of the invention may comprise an exemplary instrument that may use non-contact LSS to obtain information about a tissue condition in a patient's esophagus *in vivo*. The instrument may comprise illumination optics used for illuminating a portion, or a site, of the surface of the esophagus with one or more polarized light beams and receiving optics for receiving reflected light beams that result from backscattering of the incident polarized light beams from the surface of the illuminated site. In some embodiments, the instrument may include optics for collimating the incident polarized light beams and receiving optics for collimating the received light. Further, the instrument may include a probe with illuminating optics and/or receiving optics that may be moveable relative to a stationary portion of the probe, for scanning a line along tissue or for scanning an area of tissue.

The probe may be inserted into or otherwise associated with the instrument such as an endoscope. The probe and the illumination and receiving optics of the probe, in combination with an analysis technique developed to process data collected by the probe, may allow rapid scanning of a organ. It should be appreciated that embodiments of the invention are not limited to any particular probe and any suitable device may be substituted. Accordingly, large portions of the organ such as the esophagus may be scanned, which makes the method and system in accordance with the embodiments of the invention applicable in a clinical setting. Indeed, Applicants demonstrated that a system employing polarized LSS in accordance with some the embodiments of the invention provides reliable detection of precancerous changes in the esophagus, as discussed in more detail below. In some embodiments of the invention, two-dimensional scanning of the tissue may be performed. The instrument may be insensitive to a spacing between a probe tip and the tissue being examined. As a result, a quality of the detection may not be affected by peristaltic movements of organs of the gastrointestinal tract.

Some embodiments of the invention provide a system in which polarized light scattering spectroscopy is employed in combination a suitable endoscopic device. Thus, a polarized light scattering spectroscopy (PLSS) endoscopic instrument system may be employed. The PLSS may be defined as an optical technique that relates the spectroscopic properties of light elastically scattered by light scattering particles such as, for example, epithelial cell nuclei to their size, shape and refractive index.

To be suitable for use by a medical practitioner in a clinical setting, measurements collected using a EPSS device, or instrument, from a potion of the tissue in accordance with some embodiments of the invention, need to be easily interpreted as reliably indicative of certain conditions of the tissue. This description focuses, as an example, on screening the esophagus of patients with BE for presence of dysplasia of different degree and, possibly, carcinoma. If precancerous changes in the esophagus of such patient are detected early enough, chances of the patient's survival increase significantly. However, it should be appreciated that embodiments of the invention are not limited to detecting abnormal changes in tissue of the esophagus and the detection may be performed in tissue of various other organs from gastrointestinal tract, as well as various organs from reproductive, respiratory and other tracts.

Accordingly, Applicants have developed an analysis technique that allows extracting information on the underlying structure of the examined tissue from light diffusely scattered from the tissue (which comprises both transmitted light and backscattered light). The

information may comprise any suitable characteristics describing morphological and histological properties of tissue of the esophagus or any other organ. For example, the characteristics providing information about nuclear enlargement, crowding and hyperchromaticity may comprise epithelial nuclear size, nuclear size distribution, and chromatin density, respectively. Also, the characteristics may comprise information on the density of the collagen matrix, hemoglobin concentration and oxygen saturation of hemoglobin in the underlying tissue.

Further, the structural information on a certain site on the tissue may be mapped to a location of the site. The mapping may be presented to a user in any suitable format that allows the user to visually determine sites that may exhibit abnormal changes. As a result, better diagnosis may be possible. In some embodiments, the mapping may be presented to the user in real time – in response to illuminating the site, and collecting and processing the results during the endoscopy of the patient.

To provide the visual representation of the examined portion of the tissue as discussed above, in some embodiments of the invention, during endoscopic scanning of the surface of an organ such as the esophagus using the LSS probe (e.g., PLSS probe), images of the surface may simultaneously be taken. The images may be taken using any suitable device. As a result, information from the images may be combined with information provided by an analysis of data collected by the probe. In one embodiment, image information may be overlaid with a color-coded map, which may be semitransparent, representing diagnostic information derived using LSS. The imaging provides improved visual representation of the examined tissue and may thus lead to a more accurate diagnosis.

Applicants have developed a model for assessing the esophagus and demonstrated modeling clinical tissue reflectance in terms of the underlying tissue constituents such as scatterers and absorbers. In accordance with some embodiments of the invention, Applicants have created an analytical model, using the diffusion approximation, to describe the tissue reflectance spectrum collected by a finite sized probe with a certain effective radius.

Applicants' analysis indicates that the scattering coefficient of tissue decreases significantly during the development of dysplasia, suggesting that changes that are not observed histopathologically are taking place within the lamina propria and submucosa before the onset of invasion. The lamina propria is a layer of loose connective tissue which lies beneath the epithelium and together with the epithelium constitutes the mucosa. In the gastrointestinal tract,

the submucosa is the layer of dense irregular connective tissue that supports the mucosa, as well as joins the mucosa to the bulk of underlying tissue such as smooth muscle.

In some embodiments, a EPSS instrument employs collimated illumination and collection optics that enable the instrument to collect data for generating maps of epithelial tissue that may not be affected by the distance between a probe tip of the instrument and the mucosal surface. This may make the instrument less sensitive to peristaltic motion.

The system employing the PLSS may include, among any other suitable components, a computer programmed to produce structural tissue information or information regarding a tissue condition from *in vivo* spectroscopic data. The system may include any suitable display device for displaying information on the structure of the tissue and information that relates the structure to a corresponding diagnostic condition. For example, the system may include a display device for displaying a map of structural tissue information or a map of a tissue condition over an area. Accordingly, the system may enable *in vivo* detection and diagnosis of dysplastic tissue and/or adenocarcinoma during endoscopy for patients with Barrett's Esophagus. It should be appreciated that embodiments of the invention allow detecting dysplasia and other precancerous changes in tissues of other organs such as the lungs, colon, kidney, pancreas, urinary bladder, uterus, gall bladder, intestine and others.

Embodiments of the invention provide a method may be used to perform rapid optical scanning and multispectral imaging of the entire surface of the organ. The analysis of the data collected while scanning the surface of the organ may allow detecting otherwise invisible changes one or more portions of the organ affected by a certain degree of dysplasia. Thus, suspicious sites where a biopsy is desired to be taken for further analysis may be identified. Accordingly, the method may be used to guide the biopsy and a sample of the tissue may be collected from the suspicious sites while the scanning is being performed.

An embodiment of the invention describes EPSS instrument that provides a diagnostic screening tool that may enable a gastroenterologist to rapidly survey the region of Barrett's esophagus (BE) in a patient with this disease, and allow the gastroenterologist to determine with high probability and in real-time, regions of dysplasia and carcinoma. The instrument may distinguish between the categories of adenocarcinoma, high-grade dysplasia, low-grade dysplasia, indefinite for dysplasia and non-dysplastic BE. It may be able to perform measurements of the full length of the esophagus in about two minutes and provide the information in real time. Suspicious areas can then be biopsied and the diagnosis verified. The

instrument may reduce the need for performing either systematic or random biopsies for screenings or surveillance. Thus, it may provide a powerful tool for screening the large population of Barrett's esophagus patients for early precancerous changes.

An exemplary EPSS instrument may be based on the technique of light scattering spectroscopy (LSS), which has been demonstrated in a proof-of-principle study to be able to perform such measurements in the epithelial tissue of five different organs, including BE where these proof-of-principle studies were the most extensive and successful. The proposed technique may greatly reduce the time and labor involved in performing screening and obtaining diagnoses, cause less patient discomfort, require fewer biopsies, and help the pathologist to base a diagnosis on uniform quantitative criteria, making the diagnosis more consistent. Because of these advantages, embodiments of the invention may significantly improve the probability of detecting potential malignancies in the early stages, when cures are possible, and it may be highly cost effective.

Applicants have demonstrated that the developed system and method for detection of dysplasia in Barrett's esophagus provided by some embodiments of the invention are clinically useful. The system which may be referred to as endoscopic polarized scanning spectroscopy (EPSS) allows to rapidly survey a comparatively large area of the esophagus while simultaneously detecting changes on a cellular scale. This system comprises a combination of a scanning instrument that is suitable for use in endoscopy with a unit for polarized light scattering spectroscopy (PLSS). To assess performance of the EPSS system, Applicants have performed experiments in humans using the system, which is discussed in more detail below.

Not all patients with BE progress to adenocarcinoma. Some live their entire lives without undergoing malignant or neoplastic transformation. Others demonstrate a rapid progression to carcinoma, and will die of esophageal cancer if it is not diagnosed and treated in a timely manner. The standard of care for surveillance of patients with BE is still developing. Although periodic endoscopic surveillance of patients with Barrett's esophagus has been shown to detect carcinoma in its earlier stages, random biopsy surveillance has significant limitations. Dysplastic and early carcinomatous lesions arising in Barrett's esophagus are not visible macroscopically; therefore, surveillance may require extensive random biopsies of the esophagus and histologic examination of the excised tissue for dysplasia. Taking biopsy specimens at random locations for surveillance may be prone to sampling error (missed dysplastic lesions) and may have significant cost and risk. There also is significant interobserver

disagreement between pathologists in diagnosing dysplasia. Large sampling error, significant cost and risk, and disagreement between pathologists in diagnosing dysplasia in specimens limit the value of the current random biopsy endoscopic surveillance strategy.

Similarly, there is little agreement on the most appropriate management of HGD when it is found. Because of the marked variability (range 0-73%; most often quoted as 33%) in finding unsuspected carcinoma in patients with HGD, esophagectomy (surgical removal of part or all of the esophagus) is recommended by many clinicians to eliminate the risk of carcinoma or to detect and treat it at an early and treatable stage. However, this approach has been criticized because of the high morbidity and mortality associated with esophagectomy, the lack of a systematic biopsy protocol prior to surgery, and the variable natural history of the disease.

Dysplasia in the gastrointestinal tract is defined as neoplastic epithelium confined within an intact basement membrane. Dysplasia in BE can be classified as low or high-grade, based on criteria originally defined for dysplasia in inflammatory bowel disease. Low-grade dysplasia (LGD) is defined primarily by cytological abnormalities, including nuclear enlargement, crowding, stratification, hyperchromasia, mucin depletion and mitoses in the upper portions of the crypts. These abnormalities extend to the mucosal surface. High-grade dysplasia (HGD) is characterized by even more pronounced cytological abnormalities, as well as glandular architectural abnormalities including villiform configuration of the surface, branching and lateral budding of the crypts, and formation of the so-called back-to-back glands. When there is any doubt as to the significance of histological abnormalities in a specimen because of inflammation, ulceration or histological processing artifacts, the findings may be classified as indefinite for dysplasia (IND) in order to prevent unnecessary clinical consequences.

Optical techniques that have been explored for detecting dysplasia in BE include light scattering spectroscopy (LSS), diffuse reflectance spectroscopy, laser-induced fluorescence (LIF) spectroscopy, Raman spectroscopy and optical coherence tomography (OCT). These techniques have been explored for significantly enhancing the probability of detecting dysplasia during an endoscopy and potentially reducing harm from random biopsy surveillance by distinguishing between dysplastic and non-dysplastic tissue *in vivo*.

Laser Induced Fluorescence (LIF) spectroscopy during endoscopy is believed to measure the abnormal concentrations of certain endogenous fluorophores such as porphyrins in dysplastic and malignant tissue. LIF using tissue autofluresence has shown some promise for the detection of HGD. However, diagnostic algorithms for analysis of the LIF data from tissue

autofluoresence have not been able to correctly classify sites with LGD and focal HGD. Other fluorescence spectroscopy studies using exogenous fluorophores have also reported some positive results for detecting high-grade dysplasia. However, focal high-grade and low-grade lesions have not been detected reliably using this technique.

Raman spectroscopy is based on changes induced by light in the vibrational and rotational states of molecular bonds. Raman scattering can occur in response to a wide range of wavelengths, including visible, UV, and near-infrared. Because most biologic molecules are Raman-active, Raman spectroscopy could potentially be used to determine the biochemical status of tissues. Unfortunately, the intensity of a Raman emission spectrum is extremely low, typically a million times weaker than the background fluorescence that results when tissue is excited by ultraviolet and visible wavelengths of light. Thus, Raman spectra are normally obscured by a broad band of fluorescence when light in the visible range is used to excite tissue.

Despite these limitations, a Raman spectroscopy system has been used *in vivo* in gastrointestinal endoscopy. Raman spectra were obtained in 5 seconds with a low signal-to-noise ratio. However, analysis of the acquired data revealed only small differences between normal and diseased tissues and indicated the need for a system and analysis algorithm that more clearly distinguishes between normal and diseased tissue.

Optical coherence Tomography (OCT) provides two-dimensional cross-sectional images of the gastrointestinal tract of a patient. Like endoscopic ultrasound, OCT provides true anatomic images corresponding to the layers of the gastrointestinal tract (e.g. mucosa, submucosa, muscularis propria, and serosa/adventitia). However, by using light instead of ultrasound waves, the resolution of OCT is nearly 10-fold greater than that of high frequency endoscopic ultrasound, and approaches that of light microscopy. Preliminary reports concerning OCT in patients with BE indicate that Barrett's and normal squamous epithelium can be readily differentiated by OCT. However, because the most characteristic changes in malignant transformation of BE are happening on the cellular and sub-cellular scale, resolution of OCT is not sufficient yet to observe those changes. Whether OCT might be used to detect early-stage cancer or HGD in the future is uncertain.

Although the above results indicate the diagnostic potential of LIF, and Raman spectroscopy and OCT, further improvements in accuracy and methodology may be needed to provide useful clinical tools. Most of the diagnostic algorithms employed have used only simple diagnostic indices, such as intensity ratios, although a few have employed full spectral methods.

Further, none of these methods permits direct interpretation of changes in tissue structure and composition from obtained data. Diagnostic correlations have been largely empirical. A major limitation of the techniques reviewed in this section may be the current inability to detect changes in tissue on cellular and sub-cellular scale, the level on which many structural changes due to dysplasia occur.

For example, precancerous changes in the mucosae of various organs including the esophagus share common histological and cytological features. These features manifest themselves as morphological and biochemical alterations that are mainly confined to cellular epithelial layer. To detect those features a technique is needed, which would target microscopic properties of cells and subcellular organelles. Light scattering is sensitive to those changes. Promising results cited herein and discussed below demonstrate that LSS can provide such information in BE.

Before embodiments of the invention including methods instruments and systems are described in detail with respect to Figs. 7 through 15C, an explanation is provided of how data obtained from polarized light scattering spectroscopy relates to structural information of cells in tissue.

Light Scattering Techniques for Tissue Characterization

Although single scattering of collimated light has been used to study cells and subcellular structures in suspension, this approach cannot be directly used in tissue, because light incident on tissue is randomized by multiple scattering. Nevertheless, diffusely scattered light from tissue (both transmitted light and backscattered light) contains information about the tissue's underlying structure. However, because of randomization, the information in diffusely scattered light from tissue is averaged over several transport lengths. On the other hand, light scattering in the thin layer at the epithelial tissue surface is not completely randomized, and information about individual scatterers in this layer can be retained, even if the layer thickness is significantly smaller than a transport length.

Different studies have demonstrated a relationship between light scattering, tissue structure and a tissue condition, as described below. In measurements of reduced scattering and absorption coefficients of liver tissue, most of the scattering has been attributed to mitochondrial content of the hepatocytes. In measurements of the variation in the refractive index of fibroblasts, evidence was found of a broad distribution of scatterers ranging from 2 to 0.2 μm. It

has been shown that refractive indices of the cell nucleus and membranes are significantly higher than those of other subcellular structures and that nuclei provide the main contribution to forward scattering in lymphocytes. It has also been shown that the nucleus scatters predominantly in the forward direction, while smaller particles scatter at larger angles. Scattering studies on cell suspensions have shown that scattering takes place at the structures within the cells rather than from the cell surface. Most of these studies were carried out on cell suspensions. Recently, polarized backscattering from tissue was used to obtain images of biological cell suspensions. It was shown that in fibroblasts, mitochondria are the strongest scatterers. Differences in mitochondria size and concentration were observed between healthy and diseased cells and tissues.

Applicants have developed a new method of tissue analysis and diagnosis based on LSS and applied it to detection of dysplasia in BE. Applicants collected and analyzed clinical spectra to extract tissue characteristics related to the underlying optical parameters of the epithelial cells in BE. These tissue characteristics may include the size distribution of epithelial cell nuclei and nuclear density. Unlike simple diagnostic indices, these characteristics contain information about the disease state of the tissue. These characteristics may provide better diagnostic indices, because they contain more information regarding the tissue, and also because they permit direct interpretation of tissue composition.

Results with a Single Point Probe

The ability of LSS to distinguish various stages of dysplasia in patients with BE has been demonstrated by the Applicants in proof-of-principle studies using a single point probe. The data in these studies was reduced offline, and then compared with data from biopsies taken at corresponding locations. Locations were chosen randomly. After data was obtained, information about cell nuclear morphology in the LSS data needed to be extracted.

There are two principal techniques for extracting this information–subtraction of diffuse background using diffuse reflectance spectroscopy and polarization background subtraction. Diffuse reflectance spectroscopy has the advantages of retaining information about the biochemical and morphological organization of the submucosa, such as the density of the collagen matrix, and the degree of angiogenesis. Polarization background subtraction has the advantage of being less sensitive to tissue variability. The results of studies using these two techniques are discussed below.

Basic Principles of Light Scattering Spectroscopy

Applicants have developed a light scattering technique for measuring the size distribution and density of epithelial cell nuclei. As is discussed below, enlarged nuclei are primary indicators of cancer, dysplasia and cell regeneration in BE. Applicants' results, summarized below, demonstrate that the technique may accurately diagnose dysplasia clinically in the BE.

The organs of the body are lined with a thin, highly cellular surface layer of epithelial tissue, which is supported by underlying, relatively acellular connective tissue. In healthy tissues, the epithelium often includes a single, well-organized layer of cells with en-face diameter of 10-20 μm and height of 25 μm. In dysplastic epithelium, the cells proliferate and their nuclei enlarge and appear darker (hyperchromatic) when stained. LSS may be used to measure these changes. The details of the method have been published in an article by Perelman LT, Backman V, Wallace M, et al. (Observation of Periodic Fine Structure in Reflectance from Biological Tissue: A New Technique for Measuring Nuclear Size Distribution. *Phys. Rev. Lett.* 1998;80:627-30), which is hereby incorporated in its entirety, in the Appendix.

In an example, when an incident beam of light irradiates an epithelial layer of tissue, a portion of this light is backscattered from the epithelial nuclei, while the remainder may be transmitted to deeper tissue layers, where it undergoes multiple scattering and becomes randomized before returning to the surface. Epithelial nuclei can be treated as spheroidal Mie scatters with refractive index, n_n which is higher than that of the surrounding cytoplasm, n_c. Normal nuclei have a characteristic size of l = 4-7 μm. In contrast, the size of dysplastic nuclei varies widely and can be as large as 20 μm, occupying almost the entire cell volume. In the visible range, where the wavelength of light $\lambda << l$, the Van de Hulst approximation can be used to describe the elastic scattering cross section of the nuclei:

$$\sigma_s(\lambda, l) = \frac{1}{2}\pi d^2 \left\{ 1 - \frac{\sin(2\delta/\lambda)}{\delta/\lambda} + \left[\frac{\sin(\delta/\lambda)}{\delta/\lambda} \right]^2 \right\}, \qquad (1)$$

with $\delta = \pi d(n_n - n_c)$.

Equation (1) reveals a component of the scattering cross section which varies periodically with inverse wavelength. This, in turn, gives rise to a periodic component in the tissue reflectance. Since the frequency of this variation (in inverse wavelength space) is proportional to particle

size, the nuclear size distribution can be obtained from the Fourier transform of the periodic component.

To test this relationship, Applicants studied the spectra of elastic light scattering from densely packed unstained monolayers of isolated normal intestinal epithelial cells and intestinal epithelial T84 malignant cell line, affixed to glass slides in buffer solution and placed on top of a $BaSO_4$ diffusing plate, used to simulate the diffuse reflectance from underlying tissue. The spectra were then inverted to yield nuclear size distributions. The extracted and measured distributions for both normal and T84 cell samples were in very good agreement, indicating the validity of the above physical picture and the accuracy of the Applicant's method of extracting information.

Application of Light Scattering Spectroscopy to Barrett's Esophagus

Applicants observed similar periodic fine structure in diffuse reflectance from BE of human subjects undergoing gastroenterological endoscopy procedures. A schematic diagram of the proof-of-principle system 100 used to perform LSS is shown in FIG. 1. It should be appreciated that the system is shows by way of example only. System 100 comprises a fiber optic probe 102 associated with endoscope 104. A cross-sectional view 106 of fiber optic probe 102 comprising optical fibers is shown as an insert in FIG. 1. Probe 102 may be used to scan a portion, or a site, of tissue shown by way of example only as *in vivo* tissue 108.

In FIG. 1, a light source for fiber optic probe 102 is shown by way of example only as xenon lamp 110. Spectra of light backscattered from the portion of tissue 108 may be analyzed in a device shown by way of example only as spectrograph (spectroscope) 112. Operation of lamp 110 and spectrograph 112 may be controlled by controller 114 which is associated with a computing device 116. It should be appreciated that system 100 may comprise any other suitable components. In addition, for the convenience of the representation, not all component shown in FIG. 1 are labeled.

In this example, immediately before performing biopsy at a particular site, the reflectance spectrum from the site was collected using an optical fiber probe (e.g., fiber optic probe 102). The probe was inserted into the accessory channel of the endoscope (e.g., endoscope 104) and brought into gentle contact with the mucosal surface of the esophagus, shown in FIG. 1 as the portion of tissue 108. The probe 102 delivered a weak pulse of white light to the tissue and collected the diffusely reflected light. The probe tip sampled tissue over a

circular spot approximately 1 mm^2 in area. The pulse duration was 50 milliseconds, and the wavelength range was 350-650 nm. The optical probe caused a slight indentation at the tissue surface that remained for 30-60 seconds. Using this indentation as a target, the site 108 was then carefully biopsied, and the sample was submitted for histologic examination. This insured that the site examined spectroscopically matched the site evaluated histologically.

The reflected light was spectrally analyzed, and the spectra were stored in a computer (e.g., computer 114 or in any other suitable computer). The spectra include a large background from submucosal tissue, on which is superimposed a small (2%-3%) component that is oscillatory in wavelength because of scattering by cell nuclei in the mucosal layer. The amplitude of this component may be related to the surface density of epithelial nuclei (number of nuclei per unit area). Because, in this example, the area of tissue probed is fixed at about 1 mm^2, this parameter may be a measure of nuclear crowding. The shape of the spectrum over the wavelength range may be related to nuclear size.

Examples of nuclear size distributions extracted from the small oscillatory components for non-dysplastic and dysplastic BE sites appear in FIG. 2 which shows typical size distributions of nuclear volume verses nuclear diameter for a non-dysplastic site (solid line) and for a dysplastic site (dashed line). As can be seen, the difference between the distributions for non-dysplastic and dysplastic sites is pronounced. The distribution of nuclei from the dysplastic site is much broader than that from the non-dysplastic site , and the peak diameter is shifted from ~7 μm for the non-dysplastic site to about ~10 μm for the dysplastic site. In addition, both the relatively number of large cell nuclei (>10 μm) and the total number of nuclei are significantly increased. As shown by FIG. 2 LSS spectral data provides a quantitative measure of the density of nuclei close to the mucosal surface.

However, single scattering events cannot be measured directly in biological tissue. Because of multiple scattering, information about tissue scatterers is randomized as light propagates into the tissue, typically over one effective scattering length (0.5-1 mm, depending on the wavelength). Nevertheless, the light in the thin layer at the tissue surface is not completely randomized. In this thin region, the details of the elastic scattering process can be preserved. Therefore, the total signal reflected from a tissue can be divided into two parts: single backscattering from the uppermost tissue structures such as cell nuclei, and a background of diffusely scattered light. The background signal from diffusely scattered light may be removed to analyze the single scattering component of the reflected light,. This can be achieved

either by modeling using diffuse reflectance spectroscopy or by polarization background subtraction.

Polarization background subtraction may have the advantage of being less sensitive to tissue variability. However, the diffuse reflectance spectroscopy may have its own advantages because it can provide valuable information about biochemical and morphological organization of submucosa and degree of angiogenesis. In addition, diffuse reflectance spectroscopy can be used in combination with polarization background subtraction to extract additional potentially valuable information. Although an exemplary probe, an exemplary instrument, and an exemplary system are described herein as an LSS probe, an LSS instrument and an LSS system that uses polarization background subtraction, exemplary embodiments may be configured for LSS and/or diffuse reflectance spectroscopy, as embodiments of the invention are not limited in this respect.

Diffuse Reflectance Spectroscopy of Barrett's Esophagus

Applicants collected reflectance data for BE and developed a method for accurately modeling clinical tissue reflectance in terms of the underlying tissue scatterers and absorbers. This method provides both direct physical insight and quantitative information about the tissue constituents that give rise to the reflectance spectra. The method is summarized here. Additional details can be found in two references (Georgakoudi I, Jacobson BC, Van Dam J, et al. Fluorescence, reflectance and light scattering spectroscopies for evaluating dysplasia in patients with Barrett's esophagus. *Gastroentorolgy* 2001;120:1620-9 and Zonios G, Perelman LT, Backman V, et al. Diffuse Reflectance Spectroscopy of Human Adenomatous Colon Polyps In Vivo. *Applied Optics* 1999;38:6628-37), each of which is incorporated herein in its entirety, in the Appendix.

Applicants created an analytical model, using the diffusion approximation, to describe the tissue reflectance spectrum collected by a finite sized probe with an effective radius r_c. Biological tissue is treated as a homogeneous medium with wavelength–dependent absorption coefficient μ_a and reduced scattering coefficient μ Incident photons are scattered and absorbed in the tissue, with the surviving scattered photons eventually escaping from the tissue surface. A fraction of the escaping diffusely reflected light is collected by the probe.

A simple analytical expression for the diffuse reflectance collected by the probe is

$$R = \frac{1}{2}a'\left[e^{-x} + e^{-\eta x} - \frac{e^{-r_1 x}}{r_1} - \frac{e^{-\eta r_2 x}}{r_2}\right], \qquad (2)$$

with

$$a' = s/(a+s), \quad x = \sqrt{3(1-a')}, \quad r_1 = \sqrt{1+(a+s)^2}, \quad r_2 = \sqrt{1+[(a+s)/\eta]^2},$$

$$\eta \cong 5.3, \quad a = \mu_a r_c, \quad s = \mu_s' r_c.$$

For a given probe geometry there is an -optimal value of r_c , the effective probe radius, which can be determined by calibrating Eq. (2) using the reflectance measurement of a tissue phantom with known optical properties. For the visible tissue reflectance spectra collected in BE, hemoglobin (Hb) was found to be the only significant light absorber. To account for both oxygenated and deoxygenated forms of Hb, the total absorption coefficient, $\mu_a(\lambda)$ is given by

$$\mu_a(\lambda) = \ln 10 c_{Hb}\left[\alpha\varepsilon_{HbO_2}(\lambda) + (1-\alpha)\varepsilon_{Hb}(\lambda)\right] \qquad (3)$$

where α is the Hb oxygen saturation parameter and c_{Hb} the total hemoglobin concentration. The wavelength dependent extinction coefficients (i.e., the ε's) of both forms of hemoglobin are known.

To test the above model, the reflectance spectra of a series of tissue phantoms with known absorption and scattering properties were measured. Aqueous suspensions of polystyrene spheres were used to simulate scatterers, and hemoglobin was used for absorption. Concentrations and bead size were chosen to provide absorption and scattering properties that covered the range for human BE tissue. Mie theory was used to obtain the reduced elastic scattering cross-section, as $\mu_s'(\lambda)$, of the spheres.

The phantom reflectance spectra were accurately modeled by Eq. (2), using the known absorption and scattering coefficients. By fitting Eq. (2) to experimental phantom data obtained using various values of Hb concentration, oxygen saturation, scatterer size, and scatterer density, the values of these parameters were recovered with accuracy of better than 10% over the full range of the four parameters. This established that the experimental spectra are adequately described by Eq. (2), and that this expression could be used in an inverse manner to extract the parameters from the spectra with reasonable accuracy.

Diffuse reflectance spectra were collected from BE sites as described below. The clinical data were analyzed using Eq. (2) and the known spectra of oxy- and deoxy-hemoglobin to extract values of Hb concentration and saturation, and μ_s'. For biological tissue, the reduced scattering coefficient (μ_s') is the sum of contributions from the various tissue scatterers. Detailed

information about these individual scatterers may not be available. Therefore, the reduced scattering coefficient may be defined as follows:

$$\mu_s'(\lambda) = \rho_s \sigma_s'(\lambda), \qquad (4)$$

with □, the *effective* scattering density and □□(□) the effective reduced scattering cross section. With this, tissue scattering properties are modeled in an average way, as if tissue contained a single well-defined type of scatterer. In general, □□(□) depends on the refractive index, shape and size of the scatterer, as well as on the refractive index of the surrounding medium. Mie scattering theory is used to evaluate □□(□), assuming the scatterers to be homogeneous spheres of diameter d_s and relative refractive index n, □□(□) .

FIG. 3 shows typical diffuse reflectance spectra from one nondysplastic BE site. As shown, model fits are excellent. Both the absorption dips and scattering slopes are sensitive functions of the fit parameters, providing an inverse algorithm that is sensitive to such features. An inverse algorithm was applied to the clinical spectra, obtaining values of the four parameters for each site probed. These parameters provide valuable information about the tissue properties.

This analysis establishes that the reduced scattering coefficient, μ_s', of Barrett's esophagus tissue changes gradually during the progression from nondysplastic , to low-grade dysplasia , to high-grade dysplasia, as shown in FIG. 4A. For example, at 400 nm, the μ_s' of high-grade dysplastic (HGD) tissue (1.3 ± 0.2 mm^{-1}) is lower than that of low-grade dysplastic (LGD) tissue (1.8 ± 0.3 mm^{-1}), which, in turn, is lower than that of nondysplastic BE (NDB) tissue (3 ± 1.6 mm^{-1}). Additionally, the wavelength dependence of μ_s' changes during the development of dysplasia. To describe these changes, a straight line is fit to μ_s' (□). The intercept of the line at 0 nm and the slope of the line can be used as additional two LSS diagnostic parameters as shown in FIG. 4B.

Applicants' analysis indicates that the scattering coefficient of tissue decreases significantly during the development of dysplasia, suggesting that changes that are not observed histopathologically are taking place within the lamina propria and submucosa before the onset of invasion. Recently, it has been shown that an increased level of cysteine and serine proteases is found in gastric and colorectal cancerous and precancerous lesions. Applicants' findings related to the decrease in the value of the scattering coefficient during the progression of dysplasia are consistent with the presence of such enzymes, which could result in a less dense collagen matrix, for instance. The change in the slope of μ_s' as a function of wavelength suggests that the mean

size of the tissue scattering particles is changing. Crowding of the cells and nuclei of the epithelial layer may be responsible for this change.

Thus, Applicants observed that diffuse reflectance spectroscopy can be used to obtain quantitative information about structural composition of connective tissue *in vivo*. Diffuse reflectance spectroscopy may provide additional quantitative information about tissue scatterers and absorbers.

Polarization Background Subtraction

When tissue is illuminated with a polarized light, the light backscattered from the superficial epithelial layer of the tissue retains its polarization, i.e. it is polarized parallel to the incoming light. The light backscattered from the deeper tissues becomes depolarized and contains about equal amounts of parallel and perpendicular polarizations. By subtracting the signal with parallel polarization from the signal with perpendicular polarization (or vice versa), the signal contribution from scattering off of deeper tissues can removed and the resulting signal is proportional only to the signal from the superficial epithelial layer, which contains the information about early precancerous changes.

FIGs. 5A through 5C demonstrate that polarization background subtraction can efficiently cancel the diffuse component of the scattering signal and the residual signal can be analyzed using standard LSS procedure. FIG. 5A shows a spectrum of intensity of a polarized component of backscattered light as a function of wavelength for normal intestinal cells, and FIG. 5B shows a spectrum for T84 intestinal malignant cells. FIG. 5C shows distributions of cell nuclei extracted from the spectra where the solid line is the distribution extracted from the spectral data and the dashed line is the distribution measured using light microscopy. As illustrated by FIG. 5C, spectra of polarized components of backscattered light provide information about nuclear size distributions, which can be used to differentiate normal cells from malignant cells.

Clinical Detection of Dysplasia in Barrett's Esophagus Using Light Scattering Spectroscopy

The first clinical application of this method was conducted at the Brigham and Women's Hospital and the West Roxbury Veterans Administration Medical Center. The protocol was approved by the Institutional Review Boards of both hospitals. Data were collected from 16 patients with known BE undergoing standard surveillance protocols. After informed consent,

consecutive patients undergoing surveillance endoscopy for a diagnosis of Barrett's esophagus or suspected carcinoma of the esophagus were evaluated by systematic biopsy. In surveillance patients, biopsy specimens were taken in 4 quadrants, every 2 cm of endoscopically visible Barrett's mucosa. In patients with suspected adenocarcinoma, biopsy specimens for this study were taken from the Barrett's mucosa adjacent to the tumor. Measurements were performed using a proof-of-principle LSS system shown in FIG. 1. The results are summarized below.

Table 1

	□	% Agreement
Pathologist 1 vs. colleagues	0.31	66
Pathologist 2 vs. colleagues	0.22	62
Pathologist 3 vs. colleagues	0.34	65
Pathologist 4 vs. colleagues	0.37	65
Spectroscopy vs. pathology, average diagnoses	0.57	80
Spectroscopy vs. pathology, consensus diagnoses	0.63	90

Additional details can be found in an article by Wallace M., Perelman L.T., Backman V., et al. (Endoscopic Detection of Dysplasia in Patients With Barrett's Esophagus Using Light Scattering Spectroscopy: A Prospective Study. *Gastroentorolgy* 2000;119:677-82), which is incorporated herein in its entirety, in the Appendix.

Table 1 shows interobserver agreement between individual pathologists and the average diagnoses of the 3 other pathologists and agreement between the multivariate LSS model and the average diagnosis of all 4 pathologists. To establish diagnostic criteria, 8 samples were selected as a "modeling set", and the extracted nuclear size distributions were compared to the corresponding histology findings. From this, sites were classified as dysplasia if more than 30% of the nuclei were enlarged, with "enlarged" defined as exceeding a 10 μm threshold diameter, and classified as non-dysplasia otherwise. The remaining 68 samples were analyzed using this criterion. Averaging the diagnoses of the four pathologists, the sensitivity and specificity of detecting dysplasia were both 90%, with dysplasia defined as low grade dysplasia (LGD) or high-grade dysplasia (HGD), and non-dysplasia defined as (non-dysplasia Barrett's) NDB or indefinite for dysplasia (IND). The sensitivity and specificity were excellent, given the limitations of interobserver agreement among pathologists.

To further study the diagnostic potential of LSS, the entire data set was then evaluated adding a second criterion, the population density of surface nuclei (number per unit area), as a measure of crowding. The resulting binary plot is shown in FIG. 6, in which NDB is shown with circles, IND is shown with squares, LGD is shown with solid triangles, and HGD is shown with solid diamonds. The plot reveals a progressively increasing population of enlarged and crowded nuclei with increasing histological grade of dysplasia, with the NDB samples grouped near the lower left corner and the HGD samples at the upper right. Using logistic regression, the samples were then classified by histologic grade as a function of the two diagnostic criteria.

The percentage agreements between LSS and the average and consensus diagnoses (at least 3 pathologists in agreement) were 80% and 90%, respectively. This is much higher than that between the individual pathologists and the average diagnoses of their 3 colleagues, which ranged from 62 to 66%, and this was also reflected in the kappa statistic values appearing in Table 1.

Applicants' results demonstrate that LSS can be used in a minimally invasive instrument for accurately and reliably classifying invisible dysplasia in BE *in vivo*.

Endoscopic Polarized Spectroscopic Scanning Instrument

While methods of illuminating a single point of tissue of an organ may allow detecting changes in the tissue, scanning and/or wide field modalities may be required for guiding biopsy in realistic clinical settings. EPSS is distinguished among other techniques of detecting precancerous changes in various organs (e.g., esophagus, colon, pancreas, biliary duct, cervix, stomach, small intestine, large intestine, rectum and others) by its ability to locate dysplasia in tissue which otherwise shows no visible abnormalities or lesions. By elucidating microscopic subcellular structure with macroscopic spectral measurements, EPSS may locate dysplastic tissue independent of any visual cues.

As discussed above, LSS-based detection of dysplasia in BE has been demonstrated successfully by the Applicants using a simple proof-of-principle instrument that was capable of collecting single-point data at randomly selected sites, which then were biopsied. The data was processed offline, and a comparison with the biopsy results was made at a later time. The high correlation between spectroscopic results and pathology was sufficiently promising to justify development of a clinical LSS endoscopic scanning instrument.

Reference is now made to FIG. 7, which illustrates an exemplary EPSS system 700 in

accordance with aspects of the invention. The EPSS system 700 includes a polarized LSS endoscopic scanning instrument 702 that may comprise an endoscope 704, a probe 706 (e.g., fiber optic probe 102 shown in FIG. 1) and any other suitable components. Endoscope 704 may comprise any suitable components. Thus, endoscope 704 may comprise one or more components (e.g., an imaging unit) for imaging (e.g., video imaging) surface that is being scanned. Similarly, probe 706 may comprise any suitable components. It should be appreciated that embodiments of the invention are not limited to any particular endoscope or a probe.

In some embodiments, the EPSS system 700 may be compatible with existing endoscopes and may scan any esophageal area chosen by the physician and executes software necessary to obtain quantitative, objective data about tissue structure and composition, which can be translated into diagnostic information in real time, thus providing the location of otherwise invisible HGD *in vivo* and serving as a guide for biopsy. In other embodiments, the EPSS system 700 may incorporate its own dedicated endoscope. The EPSS 700 may be used to scan large areas of the esophagus. The system enables the physician to take confirming biopsies at suspicious sites, reduces the number of biopsies taken at non-dysplastic sites, reduces the time and labor involved in screening and diagnosis, causes less subject discomfort and ensures reliable detection of pre-cancerous lesions.

In some embodiments, the EPSS system 700 may include a computing device 708. (e.g. a computer) comprising one or more processors 710 and other suitable components. Computing device 708 may be configured to execute, by one or more processors 710, code to generate analysis data comprising image and diagnostic information. The information may comprise quantitative, objective information about tissue structure and composition from obtained spectroscopic data. By way of example only, computer 708 is shown to comprise analysis unit 714 which may be used to execute the code to generate the analysis data. The code may be stored in analysis unit 714, in other component of computing device 708, or in any other suitable location. In some embodiments, the analysis data may be stored externally to computer 708. In addition, analysis unit 714 may be associated with one or more spectrometers, with processor 710 or with any other suitable component.

The system 700 may also comprise probe control unit 712 used to control operation of probe 706. The system 700 may also include at least one display device 716 for displaying image and diagnostic information. Display device 716 may comprise any suitable user interface to present the image and diagnostic information and any other suitable information to a user.

In this example, the code executing on the computing device 708 (e.g., the code in analysis unit 714), may permit spectroscopy data to be translated into diagnostic information in real time during an endoscopy procedure. The diagnostic information may be displayed to a physician on the display device 716 during the procedure enabling the physician to take confirming biopsies at suspicious sites and reduce the number of biopsies taken at non-dysplastic sites.

In some embodiments of the invention, the outer surface of probe 706 (e.g., the EPSS probe) may be made of any suitable material. For example, the probe may be made of stainless steel, parylene-coated torque tube which provides rotary and linear scanning via probe control unit 712 with stepper motors. In one embodiment, two stepper motors (e.g., a liner drive motor and a rotary drive motor) may be employed. The probe 706 may comprise of a delivery fiber and receiver fiber polarized in parallel and a second receiver fiber polarized orthogonally. The probe 706 may also comprise a parabolic mirror at the probe distal tip that may collimate the illumination beam and ensure maximum overlap of the three visual fields at around 11 mm from the probe axis, the radius of a typical adult human esophagus. Light may be emitted approximately 70 degrees proximal to the probe axis to avoid specular reflections. The system 700 may also include one or more spectrometers 718 for analyzing spectra of light backscattered from tissue illumined during scanning.

Although an embodiment of the EPSS system 700 is discussed primarily with respect to using the polarization technique to extract diagnostic information about dysplasia, embodiments of the system may also be used to sum the two polarizations to permit the application of diffuse reflectance spectroscopy, which can provide information about early stages of adenocarcinoma.

In some embodiments, a EPSS system may allow a user to scan the esophagus or any other organ of a patient to obtain quantitative, objective data about tissue structure and composition over a two-dimensional area. The contained data about the tissue may be translated into diagnostic information. The diagnostic information may be used to guide biopsy in real time.

In some embodiments, a EPSS instrument employs collimated illumination and collection optics that enable the instrument to collect data for generating maps of epithelial tissue that may not be affected by the distance between a probe tip of the instrument and the mucosal surface. This may make the instrument less sensitive to peristaltic motion.

In some embodiments, a EPSS system may incorporate a polarizer for removing unwanted background in the LSS signal and single backscattering in the diffuse reflectance spectroscopy signal. In some embodiments, the EPSS system may be used in both an LSS signal mode and in a diffused reflectance spectroscopy mode. In some embodiments, a EPSS system may combine both LSS information and diffuse reflectance spectroscopy information to provide a diagnostic assessment to a clinician.

As shown in the schematic block schematic of FIG. 8, an exemplary EPSS system 700 may comprise fiberoptic probe 706. During a procedure the fiberoptic probe 706 is inserted into an instrument channel of a device 702 such as a gastroscope 802. Gastroscope 802 is shown as a video gastroscope to indicate that gastroscope 802 is configured to collect image data (e.g., video images) on scanned portions of tissue. The device may be associated with a light source shown by way of example only as endoscope light source 803. Light source 803 may be coupled in any suitable manner (e.g., optically) with gastroscope 802. The system 700 may also include spectrometers 718 such as a spectrometer 718A for a parallel polarized signal, and a spectrometer 718B for a cross polarized signal. The system 700 may also comprise a light source 804, shown by way of example only as bright white light source, for supplying light to the probe. It should be appreciated that, although light source 804 is labeled as a bright white light source, exemplary systems may include additional or other types of light sources of different wavelength bands, as embodiments the invention are not limited in this respect.

The system 700 may also include a probe motion controller 806 (e.g., probe control unit 712) for controlling a scanning motion of a portion of the probe with respect to the gastroscope 802. The probe motion controller 806 may control operation of the probe automatically. However, the probe may be controlled manually, or in any combination of manual and automatic controlling. The system 700 may also include a device referred to as drawback device 808 for translating the probe with respect to a gastroscope. The system 700 may use, for example, commercially available gastroscopes and video processors. A standard personal computer 708 may be adapted to control the system. Commercially available spectrometers may also be adapted for use with the system.

As described above, a probe of the EPSS system may be configured to scan with respect to a gastroscope 802. Further details regarding an exemplary scanning polarization probe 900 (e.g., probe 706) are described with respect to FIG. 9. At its proximal end, the scanning polarization probe 900 may be coupled to light source 720 and spectrometer 718A. During a

clinical procedure a distal end portion 902d of the probe 900 may be passed through a 2.8 mm diameter working channel of a standard gastroscope 704 to access the esophagus. All exposed probe materials may be biocompatible and sterilizable by an acceptable method. In one exemplary embodiment, the length of the probe may be 3 meters with a trifurcation section of approximately 1 meter. The probe 900 may comprise 3 optical fibers 74 with SMA proximal connectors 905 (shown in FIG. 11) to attach one large 400 μm core diameter delivery optical fiber 904a to a broadband light source and two collection fibers 904b, 904c to the spectrometer channels. See also FIG. 11. The delivery fiber 904a carries light to the distal end portion 902d tip of the probe. At the probe's distal end portion 902d, light exiting the fiber passes through a linear polarizer 906 and then a rotating mirror 908, which may be a parabolic mirror (parabolic reflector), projects the light about the circumference of the esophagus. In one exemplary embodiment, the probe may project a 1 - 3 mm (depending on the distance of the probe from the esophageal wall) spot of linearly polarized white light (wavelengths from 400 to 800 nm), at an angle of incidence of ~17° to 20°, onto the esophageal wall from the center of the esophagus.

The probe 900 may be configured to enable rotating (scanning) the beam (i.e. moving the nominal 2 mm spot) continuously about the circumference of the esophagus and/or retracting with the same 2 mm steps to cover a BE section of interest. The mirror 908 may be coupled to a rotating shaft 80. The rotating shaft 910 may have an aperture through which the incident light beam passes. The probe 900 may also include a protective cover 912 for protecting an end portion of the rotating shaft 910.

In some embodiments of the invention, the probe 900 may be rotated and retracted using, for example, a probe motion controller unit 806. In one embodiment, the controller unit 806 may include two stepper motors 807a, 807b located inside a control box 1002, as shown in FIG. 10. The controller unit 806 may itself be controlled by a computer, for example using a software interface such as LABVIEW or any other suitable software, hardware or combination thereof. The commands of the controller unit 806 may be synchronized with the scanning of the illumination fibers and the data captured by the spectrometers. The assembled scanning polarization probe 900 and control box 1002 are shown in FIG. 11.

User Interface

As described above, a EPSS system may include a computing device and a display for interacting with a user. The system may be programmed to execute code for providing a user

interface 1200 of the polarized LSS endoscopic scanning instrument, as shown in FIG. 12. The user interface 1200 may include pseudocolor maps that provide information about cellular and subcellular structure. Such information may include, but is not limited to: nuclear size distributions and nuclear density on the mucosal surface and/or indentifying areas suspicious for dysplasia, in accordance with aspects of the invention.

The left panel 1202 shows the visual image of the esophagus acquired over a standard video input of the endoscope. The middle panel 1204 shows same image overlaid with a semitransparent color-coded map 1208 representing LSS derived diagnostic information. In FIG. 13, which shows an enlarged image of the middle panel 1204, where green spots (appearing light colored and unlabeled) represent the non-dysplastic areas and red spots, three of which are circled and labeled as 1212, represent the areas which are suspicious for dysplasia. Thus, sites suspicious for dysplasia may be identified. The bottom left panel 1214 shows the diffuse spectrum collected from one particular spot with white dots 1215 representing the experimental data and a solid (red) curve 1216 representing the model fit. The bottom right panel 1218 of the PLSS endoscopic scanning instrument interface window is also capable of displaying the residual of the parallel and perpendicular polarization spectra. These residual spectra represent a single scattering part of the signal and are diagnostically significant.

The histological algorithm described above may be used to convert the sum and the residual of the parallel and perpendicular polarization spectra into histological properties of the illuminated spot. The residual spectra are mainly originated in the epithelium and are analyzed to yield (1) epithelial nuclear size, (2) nuclear size distribution and (3) increase in chromatin density, thereby providing information about nuclear enlargement, crowding and hyperchromaticity. As described above, to extract nuclear size distributions, Applicants developed an algorithm that treats the experimentally observed LSS spectrum as a sum of the LSS spectra of cells nuclei and smaller individual organelles within the scanning spot of the instrument. The sum of two polarizations provides the diffuse reflectance spectrum yielding information about (4) the density of the collagen matrix, (5) hemoglobin concentration and (6) oxygen saturation of hemoglobin in the underlying tissue.

Histological/Biochemical Algorithm

Applicants have developed a histological algorithm that converts the detected LSS signal into the histological properties of the illuminated spot. The backscattering spectra which contain

the diagnostic information can be extracted and analyzed to yield (1) epithelial nuclear size, (2) nuclear size distribution and (3) increase in chromatin density, thereby providing information about nuclear enlargement, crowding and hyperchromaticity. In addition, diffuse reflectance spectra can be been analyzed to yield information about (4) the density of the collagen matrix, (5) hemoglobin concentration and (6) oxygen saturation of hemoglobin in the underlying tissue. Applicants have also developed a diagnostic algorithm that translates these histological properties into diagnostic information. This algorithm may be implemented in as computer executable code for data analysis that executes on a computer associated with the EPSS system, on a different computer or computing device or on a remote server system, as the invention is not limited in this respect.

The information may be presented in the form of maps color-coded for probable diagnoses. These maps may be presented to the physician in real time, independently and/or overlaid on the visual images of the esophagus, and may be used to guide biopsies.

For rapid extraction of histological and biochemical tissue parameters, Applicants developed an inverse algorithm based on least-squares minimization. Because there can be multiple minima, biologically relevant intervals need to determined for each of the model parameters, and the intervals used as constraints in the minimization procedure to improve data extraction. In addition, Applicants have employed methods which deal with multiple minima (such as simulated annealing), and select the most suitable. Applicants' algorithm was tested on phantoms and then used in clinical data analysis.

Using the polarization technique described above, spectra of the parallel component $I_{//}(\square)$ and perpendicular component $I_{\perp}(\square)$ at each point on the BE surface were measured. The residual of the parallel and perpendicular components $I_{LSS}(\square) = I_{//}(\square) - I_{\perp}(\square)$ was processed using the LSS algorithm, and the sum of those components $I_{DRS}(\square) = I_{//}(\square) + I_{\perp}(\square)$ was processed using the diffuse reflectance spectroscopy algorithm.

Applicants have shown that spectroscopic features of light backscattered from the epithelium can be used to extract important information about the stage and progression of dysplasia. Although nuclear size distributions are correlated with HGD, LDG and NGD in exemplary embodiment described herein, nuclear size distributions and nuclear densities may be correlated with other pathological diagnoses, and diagnostic thresholds may be defined for various tissue conditions as well as for various stages of precancerous conditions, as the invention is not limited in this respect.

The experimentally measured LSS spectrum is a linear combination of the LSS spectra of epithelial cell nuclei and other subcellular organelles of various sizes and refractive indices. The experimental residual spectrum $I_{LSS}(\square)$ can be expressed as an integral over the organelles' diameters δ and relative refractive index n,

$$I_{LSS}(\lambda) = C(\lambda) \int_0^{\delta_{max}} d\delta \int_{n_{min}}^{n_{max}} S(\lambda,\delta,n) F(\delta,n) dn + \varepsilon(\lambda), \qquad (5)$$

where $S(\lambda,\delta,n)$ is the LSS spectrum of a single scatterer with diameter δ (within the range from 0 to δ_{max}) and refractive index n (within the range from n_{min} to n_{max}, $F(\delta,n)$ is the organelle size and refractive index distribution, and $\varepsilon(\lambda)$ is the experimental noise. Applicants' goal was to determine that part of distribution $F(\delta,n)$ which describes the cell nuclei. The calibration function, $C(\lambda)$, takes into account characteristics of the instrument. It should be noted that because of light collimation, $C(\lambda)$ is independent of the distance to the target, and thus precise positioning of the optical head relative to the esophageal walls may not be needed. Equation (5) can be written as a discreet sum over organelles' diameters and refractive indexes:

$$I_K = C_k \sum_{i=1}^{N} \sum_{j=1}^{M(i)} F_{ij} \cdot S_{ij} + E_k, \qquad (6)$$

where F_{ij} is a discreet two-dimensional distribution,

$$S_{ijk} = \int_{\delta_i}^{\delta_{i+1}} d\delta \int_{n_j(i)}^{n_{j+1}(i)} S(\lambda_k,\delta,n) dn,$$

noise E_k is the sum of the experimental noise, errors associated with inaccuracy of the model, and discrimination errors, N is the number of discreet sizes, $M(i)$ is the number of refractive indices for the sizes i, and λ_k are discreet points across the spectral range, where k is changing from 1 to p. The number of unknowns in Eq. (6) is determined by the range of the diameters δ_R to δ_{max} and the range of refractive indices n_{min} to n_{max}, and is

equal to $q = \sum_{i=1}^{N} M(i)$.

Since a certain amount of noise E_k is present, it is not feasible to calculate the distribution F_{ij} by directly inverting the matrix S_{ijk}. Therefore in order to solve equation (6) the following function may be minimized:

$$\Phi = \sum_{k=1}^{p} w_k \left(I_k - C_k \sum_{i=1}^{N} \sum_{j=1}^{M(i)} F_{ij} S_{ijk} \right)^2 \qquad (7)$$

where w_k is a weight function determined from noise analysis, and the sum is calculated over all spectral points. Minimizing Φ requires inverting the ill-conditioned matrix $A_{nm} = \sum_{k=1}^{p} w_k \sum_{i=1}^{N} \sum_{j=1}^{M(i)} S_{ijk} S_{nmk}$. Thus, additional prior information about the distribution function F_{ij} may be employed such as that the distribution function cannot be negative $F_{ij} \geq 0$. This is an important constraint, which makes the solution of problem (7) stable. The linear least squares with non-negativity constraints algorithm is used to invert the size and refractive index distribution.

By increasing the number of elements q in distribution F_{ij}, the discreet representation of F_{ij} may be made more accurate. However, at the same time the condition number of the matrix A_{nm} is significantly increasing with the increase of q, making the problem more unstable. Thus, q needs to be optimized. To do so, the amount of information present in the light scattering spectra should be evaluated.

The spectroscopic range of an exemplary system is from 400 nm to 800 nm with a resolution of 2 nm. This constitutes a bandwidth of 400 nm for $p = 200$ independent spectral points. Thus, the highest number of points across the range of sizes and refractive indices q should be limited by 200. Since the Mie scattering calculations showed that: (1) the LSS spectra of small scatterers (smaller than 1 μm) are predominantly smooth, and (2) the shape of the LSS spectra of small scatterers is almost independent of the refractive index, the number of points needed to describe the contribution of the small particles is significantly smaller than p. Calculations show that 20 points is enough to describe the contribution of submicron organelles in epithelial cells. Because the nuclear size distribution is relatively smooth, approximately 15 points can be used to describe the size distribution of large particles (from 1 μm to 10 μm), which includes nuclei. Unlike spectra of the small particles, LSS spectra of the large particles are affected by the refractive index and 4 points are used to describe variation of the refractive indexes. The rest of the points in the distribution can be reserved to describe the shape of the nuclei, which initially is described by their elongation.

In experiments with mixtures of subcellular organelles of various sizes, Applicants tested some ideas described above. Applicants were able to accurately and consistently reconstruct the

organelle size distributions and verify those distributions with electron microscopy. Using a similar approach, Applicants also reconstructed the nuclear size distribution in cell monolayers. Some significant improvements of this approach include (1) taking into account polarization of light, (2) describing the shape of the nuclei and (3) speeding up the analysis to be able to guide biopsy in real time.

In addition, as discussed above, Applicants developed a quantitative model of diffuse reflectance and applied it to the analysis of clinical reflectance spectra of BE.

Endoscopic Procedure with EPSS instrument

In one embodiment, a EPSS system may work with commercially available gastroscopes. An exemplary measurement procedure 1600, which is shown as a flowchart in FIG. 16, is as follows:

Step 1. Insert Endoscope. The endoscope (e.g., gastroscope 802) may be inserted, in block 1602, into an organ such as the esophagus until it is about 2 cm from the lower esophageal sphincter (LES) 2114, as shown in FIG. 15A. The edge of the field of view may be about 2 cm from the LES 2114. The endoscope's view of the LES 1514 is shown on the simulated video monitor 1500 in FIG. 15A.

Step 2. Advance probe. At block 1604, the probe's light source may be turned on and the probe 706 may be positioned – i.e., advanced through the endoscope's instrument channel 805 until it is close to the LES (FIG. 15B), extending no more than 2.5 cm from the endoscope tip as shown in FIG. 14. The starting location of the spot 1516 is seen in the endoscope's video image 1500, as depicted in FIG. 15B. The spot has a nominal diameter of 2 mm. While looking at the video images, the endoscopist may articulate the tip of the scope slightly to insure that the probe is fairly centered in the esophagus.

Step 3. Scan. When the starting location is correct, the scanning sequence is initiated, at block 1606. The LSS scanning may progress from the gastro-esophageal junction to the mouth. No biopsies are taken on the scan. The "flying spot" automatically indexes around the esophagus circumferentially in 30 angular increments to make one 360 degree sweep. The probe 706 may then be automatically moved proximally by 2 mm, and the angular sweep is repeated. This step

and repeat process continues until a 2 cm wide band has been scanned (total time --- 20 sec.). The position 1518 of the flying spot at the end of the scan is shown in FIG. 15C.

Step 4. Data capture and documentation of suspicious sites. At each scanned location, spectral data is captured by two spectrometers, as shown in block 1608 of FIG. 16. Furthermore, as discussed above, one or more images (e.g., video images) of each scanner location, or a site, may be collected. At block 1620, the results may then be displayed. For example, distilled results of the spectral scan may be shown on the computer monitor in real time as the scan progresses, in the form of a false-color map overlaid, or superimposed, on a video image of Barrett's esophagus (FIG. 13). The diagnostic algorithm has been developed to work in real time and to alert a user such as an endoscopist or other medical practitioner when spectra indicating BE or dysplasia are found. Thus, the user may be provided with an indication of whether to obtain a tissue sample from an examined site.

Step 5. Forceps biopsy. At block 1612, it may be determined whether biopsy is required, based on analysis of the results displayed at block 1610. If it is determined that the biopsy is required, the process 1600 continues to block 1614, where, while observing the live image, as well as the stored image for reference, biopsy forceps 1522 may be advanced through the endoscope's second instrument channel 807 (see also FIG. 14A). The scope 802 may be articulated as needed to guide the forceps. In the locations suspicious for dysplasia as indicated by the instrument the endoscopist will collect forceps biopsies. Figure 15D shows the forceps 1522 taking a biopsy and the view through the gastroscope 802. It should be appreciated that even though, in FIG. 16, blocks 1606-1618 illustrate respective steps of process 1600 in certain order, the steps may be performed in any suitable order and one or more of the steps may be performed simultaneously. Thus, as discussed above, displaying the results at block 1610 may be performed simultaneously with performing biopsy at block 1614.

When it is determined, at block 1612, that the biopsy is not required, process 1600 may continue to block 1616 where it may be determined whether more portions of the esophagus need to be scanned. If it is determined that more portions of the esophagus need to be scanned, process 1600 may return to block 1606 to scan more portions, as discussed above. The determination may be performed automatically or in any other suitable manner.

Step 6. Move proximally, repeat. If it is determined, at block 1616, that the endoscopist wishes to scan more of the esophagus, the endoscope is pulled back proximally in 2 cm increments and the scanning process is repeated, from block 1606.

In some embodiments, standard endoscopic Narrow Band Imaging (NBI) may be employed in combination with the Polarized LSS Endoscopic Scanning Instrument to allow data collection simultaneously with the noninterrupted visual observation of the gastrointestinal tract. In addition, as discussed above, embodiments of the invention are not limited to detection of abnormal changes in organs of gastrointestinal tract and may be applied to various organs of reproductive tract, respiratory tract and other systems.

It should be appreciated that the above processing described in connection with FIG. 16 is exemplary only and similar technique may be used to detect abnormal morphological and biochemical changes in various others organs of gastrointestinal, reproductive, respiratory and other tracts. Moreover, scanning of internal and external surfaces of the organs may be performed, in accordance with some embodiments of the invention.

Multispectral Scanning During Endoscopy for Guiding Biopsy

As discussed above, Applicants have demonstrated that the EPSS system provided by some embodiments of the invention is suitable for use in a clinical setting. Described below are some results of endoscopy experiments performed by Applicants on freshly resected bovine esophagi and in humans. The experiments were performed using a system such as one shown in FIGs. 7-12, with particular exemplary setting as described below. Furthermore, during the endoscopy, images of the examined tissue and collected information were displayed on a display device comprising a user interface similar to the one shown in FIG. 13.

In one experiment, performance of the EPSS system instrument was assessed using freshly resected bovine esophagi. An endoscope was inserted into a vertically mounted bovine esophagus which was then scanned point-by-point and resulting data was recorded. Histological specimens were taken at the EPSS data collection sites. Comparing nuclear sizes revealed by the H&E image (i.e., the image generated from a sample stained using hematoxylin and eosin stain, as known in the art) with the EPSS result, showed reasonable agreement, as shown in FIGs. 17A and 17B.

FIGs. 17A and 17B illustrate EPSS scanning of esophageal epithelium during screening endoscopy. In particular, FIG. 17A illustrates a tip of probe 706 (e.g., probe 900) extended

from working channel of the endoscope 704 during scan; arrows 1702 and 1704 indicate linear (1702) and rotary (1704) motions of probe tip before and during each scan, respectively. FIG. 17B illustrates frame capture, obtained and displayed via the EPSS user interface, of an image acquired by the endoscope video channel showing the actual EPSS probe tip during scanning of the esophageal epithelium of a patient with Barrett's esophagus during a clinical procedure. The scanning illumination spot 1706 may be seen on the esophagus wall at the upper right of the image. In this example, the EPSS probe tip diameter is 2.5 mm.

In another experiment, Applicants performed clinical measurements using the EPSS system during endoscopic procedures for individuals with suspected dysplasia who had consented to participate in the study, at the (IEC) Beth Israel Deaconess Medical Center (BIDMC) Interventional Endoscopy Center. Subjects reporting to the IEC at BIDMC underwent initial screening at other institutions and were referred with confirmed Barrett's esophagus and suspicion of dysplasia. The procedure, indications, preparation and potential complications were explained to the subjects, who indicated their understanding and signed the corresponding consent forms. Applicants' protocol was reviewed by the BIDMC Institutional Review Board and the requisite approvals obtained.

In this experiment, Applicants employed a high resolution endoscope (HRE) with Narrow Band Imaging (NBI) such as, for example, an Olympus GIF-H180 gastroscope manufactured by the Olympus America, Inc. A gastroenterologist introduced the gastroscope, which had an EPSS polarized fiber optic probe in the working channel, through the mouth. The EPSS performed optical scanning of each complete, continuous region of the luminal esophageal wall chosen for examination by the gastroenterologist. Data obtained from the optical scans for each linear and angular position of the probe tip as parallel and perpendicular polarization reflectance spectra, corrected for light source intensity and lineshape, was recorded.

The following algorithm was used to distinguish non-dysplastic Barrett's esophagus from sites of HGD and LGD. The backscattering spectrum at each individual spatial location, m, was extracted by subtracting perpendicular from parallel polarized reflectance spectra, $S_m^{BS}(\lambda) = S_m^{\parallel}(\lambda) - S_m^{\perp}(\lambda)$. The backscattering spectra were then normalized to remove amplitude variations due to peristalsis,

$$S_m(\lambda) = \frac{S_m^{BS}(\lambda)}{\sqrt{\sum_{\lambda} S_m^{BS}(\lambda)^2}} \qquad (8)$$

where $S_m(\lambda)$ is the normalized spectrum and the summation is performed over all spectral points □ The root mean square normalized spectrum was calculated as follows,

$$\bar{S}(\lambda) = \sqrt{\frac{1}{N}\sum_{m=1}^{N} S_m(\lambda)^2} \qquad (9)$$

where N is the total number of scanned positions. For each measurement site m, the difference of the normalized spectrum $S_m(\lambda)$ from the root mean square normalized spectrum $\bar{S}(\lambda)$, was calculated, squared and summed over all spectral points to obtain a diagnostic parameter Δ_m at each site

$$\Delta_m = \frac{1}{2}\sum_{\lambda}\left(S_m(\lambda) - \bar{S}(\lambda)\right)^2 \qquad (10)$$

If this diagnostic parameter was greater than 0.1 (which is 10% of the mean squared spectrum summed over all spectral points) the site was considered to be dysplastic. In this example, the calibration was not performed.

The above analysis is straightforward and may therefore be performed in near real time. By extracting the nuclear size distributions from the backscattering spectra for each individual spatial location, Applicants have found that this is approximately equivalent to a contribution of more than 25% from enlarged nuclei over 9 microns in diameter. The pseudo-color maps based on this rule were then drawn and shown to the physician in each case where the EPSS instrument was used to guide the biopsy.

For the longitudinal coordinate, the starting position was measured by the distance from the upper incisors. The probe is then retracted in 2 mm steps. The starting position of the azimuthal coordinate is observable by the bright spot on the esophagus and then the data is collected every 12°. For guiding biopsy upon return examination, these coordinates are provided to the gastroenterologist. Also, the esophagus has many landmarks, which may be observable under NBI. For every map location the gastroenterologist is provided with a freeze frame image which can be used to aid in locating the guided biopsy spot using these landmarks. The same freeze frame image shows the EPSS illuminated spot where the spectrum was acquired. The EPSS spot in relation to the landmarks is used to reduce the potential problems due to peristaltic motion. Using the longitudinal and azimuthal coordinates of an EPSS mapped site, along with the associated landmarks and freeze frame image showing the illuminated spot on the esophageal wall, it may be estimated the gastroenterologist may return to the same spot within a

5 mm radius upon a subsequent examination. However, it should be noted that the follow up case presented in this example may not exemplify the intended application of the instrument in accordance with some embodiments of the invention. In practice, biopsies would be performed as dysplastic sites are first identified and mapped by EPSS, during the same procedure and not in a follow-up procedure. Hence biopsies would be guided in the initial exam, in the sense that EPSS would identify a dysplastic site where a confirmative biopsy should be performed, rather than performing biopsies in a predetermined, "blind" pattern.

Two observations may support the clinical feasibility of the above method. First, spectroscopic data collected during clinical procedures confirm that the polarization technique may be very effective in removing unwanted background signals. For example the perpendicular polarization spectral component, originating in the deeper tissue layers, exhibits standard diffuse reflectance features, with hemoglobin absorption bands clearly observable in the 540-580 nm region. The parallel polarization spectral component, in addition to diffuse features, exhibits a very clear oscillatory structure, characteristic of diagnostically important nuclear scattering originating in the uppermost epithelial layer, as shown in FIG. 18A. This figure illustrates parallel (solid line) and perpendicular (dotted line) polarization spectra collected with the EPSS instrument from a single spatial location in a subject with Barrett's esophagus.

Second, the issue of peristaltic motion may be addressed by EPSS. During a procedure, it is difficult to maintain a fixed distance between the optical probe head and the esophageal surface, due to peristaltic motion and other factors. Therefore, an important feature of the EPSS instrument may be its ability to collect spectra of epithelial tissue that are not affected by the orientation or distance of the distal probe tip to the mucosal surface. This may be achieved with collimated illumination and collection optics. Thus, a probe may be positioned at a distance within a range of distances from an examined site. Analysis of parallel polarization spectra collected at ten different locations from the same subject during a standard clinical procedure (FIG. 18B) showed that although amplitudes of the spectra differ from site to site, the spectral shape is practically unchanged. The fluctuation of the normalized difference of the perpendicular and parallel spectra in the 600 to 800 nm spectral range which carries the diagnostic information is substantially less than 10% for non-dysplastic sites, regardless of the distance of the probe from the esophageal wall.

Applicants have collected a total of 10,800 EPSS spectra in eight procedures, covering the entire scanned regions of the esophagus in seven subjects. Further, Applicants have validated the capabilities of the method by comparing EPSS data with subsequent pathology at each site where biopsies were taken. For the first two subjects, pathology was reported per quadrant not per biopsy, and so the data was not used.

For the other subjects, 95 biopsies were collected according to the standard-of-care. The locations of biopsied tissue sites were recorded by their distances from the upper incisors and their angles relative to the start of the EPSS scan (FIGs. 19A and 19B). Pathological examination revealed a total of 13 dysplastic sites of which 9 were HGD and 4 were low grade dysplasia (LGD). The rest of the sites were diagnosed as non-dysplastic.

FIGs. 19A and 19B illustrate visual representations, or maps, produced from EPSS data that are overlaid with circles indicating biopsy sites and confirmed pathology. For illustration purposes only, two circles, 1902 and 1904, indicating respective biopsy sites, are marked in FIG. 19A. Vertical axis indicates angle of rotation in degrees from start of each rotary scan; horizontal axis indicates distance in cm from upper incisors. In FIG. 19A, exemplary map areas colored with different shades of grey are shown. The maps may be presented to a user in a color format. Accordingly, in FIG. 19A, different shades of grey, from the lightest to the darkest, may represent blue-, green-, pink- and red-colored areas of the map, respectively. Blue and green map areas represent epithelium that is unlikely affected by dysplasia; red and pink map areas represent epithelium that is suspicious for dysplasia, as determined by EPSS. Two of the map areas colored in red are marked as 1906 and 1908.

Further, in FIG. 19A, highlighted solid, dashed and solid without highlighting circles indicate biopsy sites of HGD, LGD and non-dysplastic Barrett's esophagus, respectively, as determined by pathology. FIG. 19A illustrates EPSS maps comprising biopsy sites and pathology for subjects A through E. FIG. 19B illustrates biopsies taken during the initial and follow-up endoscopy procedures for subject A, overlaid on the EPSS map acquired during the initial procedure. Three follow-up biopsies were guided by the EPSS map and pathology confirmed HGD for each (indicated at 360°).

The diagnoses for each EPSS location were extracted from the residuals of the parallel and perpendicular backscattered spectral components collected by the EPSS instrument. The results may be presented as pseudo-color maps, as shown in FIG. 19A.

Double blind comparison of the EPSS maps with the biopsy reports revealed 11 true positive sites, 3 false positive sites, 80 true negative sites, and 1 false negative site (FIG. 19A). Thus, in this example, EPSS measurements are characterized by sensitivity of 92% and specificity of 96%.

The third Barrett's esophagus subject (the first in whom individually marked biopsies were taken, subject A in FIG. 19A) underwent endoscopy and biopsy, concurrent with EPSS. Visual endoscopic examination using HRE with NBI did not reveal any areas suspicious for dysplasia. Pathology of tissue biopsies taken in the pattern prescribed by the standard-of-care revealed no dysplasia and the subject was dismissed. However, the EPSS scan indicated several probable sites of focal dysplasia, which were located in regions where biopsies were not taken. Hence, subject A was recalled and several biopsies were taken in the vicinity of each site indicated by EPSS plus a repeat of the standard-of-care protocol. Video capture was acquired in subject A at one of the locations where invisible dysplasia was missed by visual examination by HRE with NBI but located by EPSS and confirmed later by pathology. As shown in FIG. 20, a freeze frame of the endoscopic video image of a site identified by EPSS as suspicious for dysplasia demonstrates that the site is visually indistinguishable from the surrounding non-dysplastic tissue even under HRE with NBI. This site is marked by an arrow 2000 in FIG. 20.

Pathology confirmed HGD at all three EPSS directed sites and one additional HGD at a point located between two EPSS indicated sites (FIG. 19B). The latter site, considered a false negative, is very close to the sites indicated by EPSS and may arise from imperfect correspondence of actual biopsy site with EPSS mapped site. This subject will now be given appropriate treatment. Standard-of-care procedures, even when diligently performed by highly skilled and experienced gastroenterologists, can miss focal dysplasias because these procedures biopsy only a very small fraction of esophageal tissue, blindly according to the prescribed protocol. The capability of EPSS to examine the entire esophageal epithelium millimeter-by-millimeter enables detection of dysplastic cells and guidance of confirmative biopsy, greatly increasing the probability of early detection and treatment and in all likelihood, of saving lives.

Pathology found HGD in biopsies from subjects B and E, who need to be treated. No suspicious sites were found in subject C, as shown in FIG. 19A. However, EPSS found a number of suspicious sites in subject D, while standard-of-care biopsies located no abnormal pathology. Subject D may be recalled for further examination.

The frequency of dysplasia in the subject sample is consistent with that of the pre-screened population referred to the BIDMC IEC for confirmation and treatment but is higher than would be expected in the general Barrett's esophagus subject population. In fact, the frequency of HGD detection in the general population of Barrett's esophagus subjects underscores the importance of having more comprehensive and effective methods for gastroesophageal cancer screening.

The Applicants' experiments described above demonstrated that the system employing a combination of endoscopy with polarized light scattering spectroscopy, in accordance with some embodiments of the invention, is well suited for use in clinical settings. The system employs imaging of an examined site of the tissue, where the resulting images are associated (e.g., overlaid with or otherwise combined) with maps (e.g., color-coded maps) representing structural characteristics of the tissue at the site. Thus, a user such as a medical practitioner may be presented with such mapping for diagnosis of suspicious sites. The user may be presented with the mapping, or other suitable representation of the results of the scanning, either during the scanning procedure itself (e.g., in "real time") or after the results have been collected and stored. When the results are presented to the user during the scanning procedure, as each site is being illuminated, imaged, and the resulting spectra of backscattered light are analyzed, the user may perform biopsy at the sites that are identified as suspicious. Accordingly, during the scanning, the biopsy may be guided – i.e., it may only be performed for sites that are identified as potentially exhibiting abnormal changes, which contrasts with performing biopsy in a predetermined pattern. As a result, burden on a patient may be alleviated.

In the system, the probe associated with the endoscopic instrument is rotatable and enables scanning of area of 360° of the examined organ such as the esophagus, used as an example organ throughout this description. The probe may be non-contact. Employing of such probe allows rapid scanning of the entire surface of the organ such as the esophagus.

It has been shown that the system may allow detecting sites suspicious for dysplasia that are undetectable using other existing methods. Indeed, the screening of several patients showed that a site that is detected as suspicious for dysplasia using the Applicants' system is visually indistinguishable from the surrounding non-dysplastic tissue even under HRE with NBI. This early detection of a potentially precancerous change in the tissue may improve a chance of a successful treatment of a respective patient.

Having now described some illustrative embodiments of the invention, it should be apparent to those skilled in the art that the foregoing is merely illustrative and not limiting, having been presented by way of example only. Numerous modifications and other illustrative embodiments are within the scope of one of ordinary skill in the art and are contemplated as falling within the scope of the invention. In particular, although many of the examples presented herein involve specific combinations of method steps, system element, instrument elements and/or probe elements, it should be understood that those acts and those elements may be combined in other ways to accomplish the same objectives. Acts, elements and features discussed only in connection with one embodiment are not intended to be excluded from a similar role in other embodiments.

What is claimed is:

VOLUME 80, NUMBER 3 PHYSICAL REVIEW LETTERS 19 JANUARY 1998

Observation of Periodic Fine Structure in Reflectance from Biological Tissue: A New Technique for Measuring Nuclear Size Distribution

L. T. Perelman,[1] V. Backman,[1] M. Wallace,[2] G. Zonios,[1] R. Manoharan,[1] A. Nusrat,[3] S. Shields,[4] M. Seiler,[4] C. Lima,[1] T. Hamano,[1] I. Itzkan,[1] J. Van Dam,[2] J. M. Crawford,[5] and M. S. Feld[1]

[1]*G. R. Harrison Spectroscopy Laboratory, Massachusetts Institute of Technology, Cambridge, Massachusetts 02139*

[2]*Gastroenterology Division, Brigham and Women's Hospital, Boston, Massachusetts 02115*

[3]*Department of Pathology, Brigham and Women's Hospital, Boston, Massachusetts 02115*

[4]*U.S. Veterans Hospital, West Roxbury, Massachusetts 02132*

[5]*Department of Pathology, Yale University School of Medicine, New Haven, Connecticut 06520-8023*

(Received 9 July 1997)

We report observation of a fine structure component in backscattered light from mucosal tissue which is periodic in wavelength. This structure is ordinarily masked by a diffusive background. We have identified the origin of this component as being due to light which is Mie scattered by surface epithelial cell nuclei. By analyzing the amplitude and frequency of the fine structure, the density and size distribution of these nuclei can be extracted. These quantities are important indicators of neoplastic precancerous changes in biological tissue. [S0031-9007(97)05049-7]

PACS numbers: 87.64.–t, 42.62.Be, 87.64.Ni

Biological tissue is a turbid optical medium, in which light transport is dominated by elastic scattering [1–3]. The primary scattering centers are thought to be the collagen fiber network of the extracellular matrix, the mitochondria, and other intracellular substructures, all with dimensions smaller than optical wavelengths [3]. However, larger structures, such as cell nuclei, typically 5–15 μm in diameter, can also scatter light.

Single scattering of collimated light is used widely to study cells and subcellular structures in suspension [4]. This approach cannot be used in tissue, since light is then randomized by multiple scattering. Nevertheless, diffusely scattered light from tissue contains information about its underlying structures [5]. Both transmitted [6] and backscattered [7] photons can be used to measure particle size. However, because of randomization, this information is averaged over several transport lengths. On the other hand, the light in the thin layer at the tissue surface is not completely randomized and information about individual scatterers can be retained, even if the layer thickness is significantly smaller than a transport length. In this Letter, we exploit this fact to extract the density and size distribution of cell nuclei near the tissue surface.

Mucosal tissues, which line the hollow organs of the body, generally consist of a thin surface layer of epithelial cells supported by underlying, relatively acellular connective tissue. In healthy tissues, the epithelium often consists of a single, well-organized layer of cells with the diameter of 10–20 μm and the height of 25 μm. In cancerous and precancerous (dysplastic) epithelium, the cells proliferate and the cell nuclei enlarge and appear darker (hyperchromatic) when stained [8].

Epithelial nuclei are spheroidal Mie scatterers with refractive index higher than that of the surrounding cytoplasm [9,10]. Normal nuclei have a characteristic diameter $l = 4–7$ μm. In contrast, dysplastic nuclei can be as large as 20 μm in height, occupying almost the entire cell volume. In the visible range, the wavelength $\lambda \ll l$ and the Van de Hulst approximation [11] can be used to describe the optical scattering cross section of the nuclei:

$$\sigma_s(\lambda, l) = \frac{1}{2}\pi l^2\left[1 - \frac{\sin(2\delta/\lambda)}{\delta/\lambda} + \left(\frac{\sin(\delta/\lambda)}{\delta/\lambda}\right)^2\right], \quad (1)$$

where $\delta = \pi l n_c(n - 1)$, where n_c is the refractive index of cytoplasm and n is the refractive index of the nuclei relative to that of cytoplasm. Thus, the scattering cross section of the nuclei exhibits a periodicity with wavelength [12]. As shown below, this gives rise to a periodic component in the reflectance from the tissue.

Consider a beam of light incident on an epithelial layer of tissue. A portion of this light is backscattered from the epithelial nuclei, while the remainder is transmitted to deeper tissue layers, where it undergoes multiple scattering and becomes randomized. All of the diffusive light which is not absorbed in the tissue eventually returns to the surface, passing once more through the epithelium, where it is again subject to scattering from the cell nuclei. Thus, the emerging light will consist of a large diffusive background plus the component of forward scattered and backscattered light from the nuclei in the epithelial layer. For a thin slab of epithelial tissue containing nuclei with size distribution $N(l)$ [number of nuclei per unit area (mm^2) and per unit interval of nuclear diameter (μm)], the approximate solution of the transport equation for the reflectance $R(\lambda)$ collected by an optical probe with acceptance solid angle Ω_c is given by the following

expression:

$$\frac{R(\lambda)}{\overline{R}(\lambda)} = e^{-\tau(\lambda)} + \frac{1 - e^{-\tau(\lambda)}}{\langle I_d(\lambda, \mathbf{s})\rangle_{\Omega_c}} \times \langle\langle I_i(\lambda, -\mathbf{s}')p(\lambda, \mathbf{s}, -\mathbf{s}')\rangle_{\Omega_i} + \langle I_d(\lambda, \mathbf{s}')p(\lambda, \mathbf{s}, \mathbf{s}')\rangle_{2\pi}\rangle_{\Omega_c}, \quad (2)$$

where $I_i(\lambda, \mathbf{s})$ is the intensity of the incident light delivered in solid angle Ω_i, $I_d(\lambda, \mathbf{s})$ is the intensity of the light emerging from the underlying tissue, and $\langle f(\mathbf{s}, \mathbf{s}')\rangle_\Omega = \int_\Omega f(\mathbf{s}, \mathbf{s}')\, d\mathbf{s}'$ for any function f and solid angle Ω, where $\mathbf{s}$ is a unit vector pointing outward from the tissue surface in an arbitrary direction. The quantity $\overline{R}(\lambda) = \langle I_d(\lambda, \mathbf{s})\rangle_{\Omega_c}/\langle I_i(\lambda, \mathbf{s})\rangle_{\Omega_c}$ is the reflectance of the diffusive background. The "optical distance" $\tau(\gamma) = \int_0^\infty \sigma_s(\lambda, l)N(l)\, dl$ [13] and scattering phase function $p(\lambda, \mathbf{s}, \mathbf{s}') = \frac{1}{\tau}\int_0^\infty p(\lambda, l, \mathbf{s}, \mathbf{s}')\sigma_s(\lambda, l)N(l)\, dl$ both depend on $N(l)$; for a sphere, $p(\lambda, l, \mathbf{s}, \mathbf{s}')$ is determined by Mie theory [11]. The first term in Eq. (2) describes the attenuation of the diffusive background, and the terms in brackets describe backscattering of the incident light and forward scattering of diffusive background by the epithelial cell nuclei, respectively.

For small Ω_c, the forward scattering and backscattering terms in Eq. (2) can be expanded in $\tau(\lambda)$. The forward scattering term oscillates in phase with $\tau(\lambda)$, as required by the optical theorem [12], whereas the backscattering term is out of phase. Thus, Eq. (2) shows that the epithelial nuclei introduce a periodic fine structure component into the reflectance with a wavelength dependence similar to that of the corresponding scattering cross section. Its periodicity is approximately proportional to nuclear diameter, and its amplitude is a function of the size and the number of nuclei in the epithelial layer. These quantities can be determined by analyzing the reflectance $R(\lambda)$.

To investigate the effects described by Eq. (2), elastic light scattering from normal and T84 tumor human colonic cell monolayers (10 and 15 sites, respectively) was studied. The cells, approximately 15 μm long, were affixed to glass slides in buffer solution and placed on top of a $BaSO_4$ diffusing (and highly reflective) plate. The tumor cells were grown in a confluent manner; normal cells were allowed to settle on a glass slide and the remaining nonattached cells were washed out. In both cases, the cells were densely packed. The diameters of the normal cell nuclei ranged from 5 to 7 μm, and those of the tumor cells from 7 to 16 μm. The $BaSO_4$ plate was used to simulate the diffuse reflectance from underlying tissue.

In the experiments, an optical fiber probe was used to deliver white light from a xenon arc flashlamp to the samples and collect the return reflectance signal. The probe tip, 1 mm in diameter, consisted of a central delivery fiber surrounded by six collection fibers (200 μm core fused silica, NA = 0.22, $\Omega_i = \Omega_c = \pi\text{NA}^2$), all of which were covered with a 1 mm thick quartz optical shield [14].

Figures 1(a) and 1(b) show the normalized reflectance $R(\lambda)/\overline{R}(\lambda)$ from normal and T84 tumor cell samples, respectively. Distinct spectral features are apparent. For comparison, the reflectance spectrum from the $BaSO_4$ plate by itself is also shown [Fig. 1(c)]. This spectrum lacks structure and shows no prominent features.

To obtain information about the nuclear size distribution from the reflectance data, Eq. (2) needs to be inverted. The nuclear size distribution, $N(l)$, can then be obtained from the Fourier transform of the periodic component of the optical distance $\tau - \tau_0 \cong [1 - R(\lambda)/\overline{R}(\lambda)]/q$, where parameter $q \approx 0.15$ depends on the

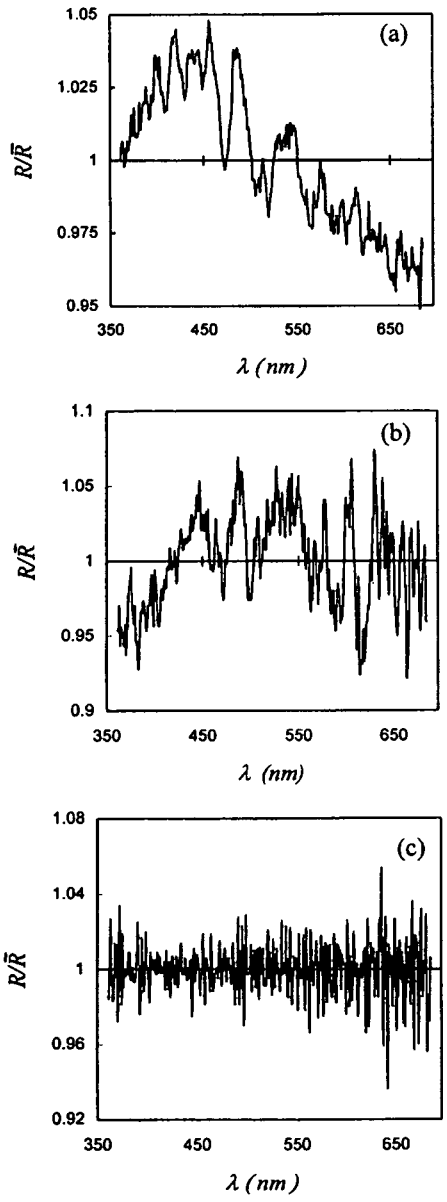

FIG. 1. Reflectance spectrum from cell monolayers. (a) Normal colon cells ($\overline{R} = 0.46$); (b) T84 cells ($\overline{R} = 0.38$); (c) $BaSO_4$ diffusing plate ($\overline{R} = 1.0$). See text for details.

probe geometry and the angular distribution of the incident and reflected light. By introducing the effective wave number $k = 2\pi n_c(n - 1)/\lambda - k_0$, we obtain

$$N(l) \cong \frac{2}{ql\pi^2}\left|\int_0^K\left(\frac{R(k)}{\bar{R}(k)} - 1\right)e^{ikl}(k + k_0)\,dk\right|, \quad (3)$$

where $k_0 = 2\pi n_c(n - 1)/\lambda_{\max}$ and $K = 2\pi n_c(n - 1)(\lambda_{\min}^{-1} - \lambda_{\max}^{-1})$.

Equation (3) was used to analyze the data. In order to remove spurious oscillations, $N(l)$ was further processed by convolving it with a Gaussian filtering function. The solid curves of Figs. 2(a) and 2(b) show the resulting nuclear size distributions of the normal and T84 cell monolayer samples extracted from the spectra of Figs. 1(a) and 1(b). A nucleus-to-cytoplasm relative refractive index of $n = 1.06$ and cytoplasm refractive index of $n_c = 1.36$ were used. The dashed curves show the corresponding size distributions measured morphometrically via light microscopy [15]. The extracted and measured distributions are in good agreement for both normal and T84 cell samples, indicating the validity of the above physical picture and the accuracy of our method of extracting information.

We have observed this periodic fine structure in diffuse reflectance from esophagus and colon mucosa of human subjects undergoing gastroenterological endoscopy procedures. We consider here the case of Barrett's esophagus, a chronic condition in which irritation transforms normal esophagus epithelium into a thin monolayer of columnar cells similar to those used in the cell culture experiments. Such patients have an increased risk of developing dysplastic change, but such change is not visible with an endoscope.

Data were collected as in the cell culture studies. The optical fiber probe was inserted into the biopsy channel of the endoscope and brought into contact with the tissue surface. The fine structure component, which is the scattering signature of the cell nuclei, is typically less than 5% of the total signal and is ordinarily masked by the background of diffusely scattered light from underlying tissue, which itself exhibits spectral features due to absorption and scattering [Fig. 3(a)]. Its spectral features are dominated by the characteristic absorption bands of hemoglobin and scattering of collagen [16]. In order to observe the fine structure, this background must be removed using an appropriate model. The absorption length μ_a^{-1} ranges from 0.5 to 250 mm as the wavelength is varied, and the effective scattering length $(\mu_s')^{-1}$ ranges from 0.1 to 1 mm [3]. Thus, both scattering and

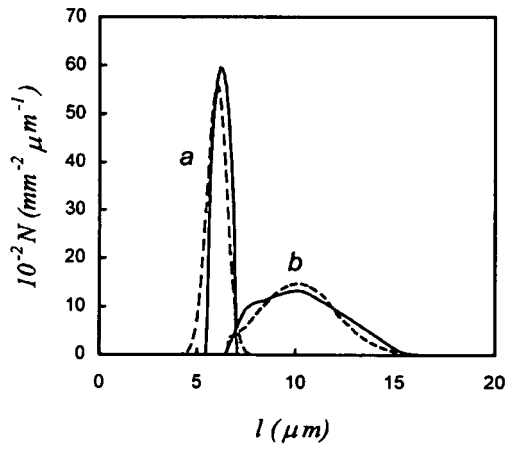

FIG. 2. Nuclear size distributions from data of Fig. 1. (a) Normal colon cells; (b) T84 cells. In each case, the solid line is the distribution extracted from the data, and the dashed line is the distribution measured using light microscopy.

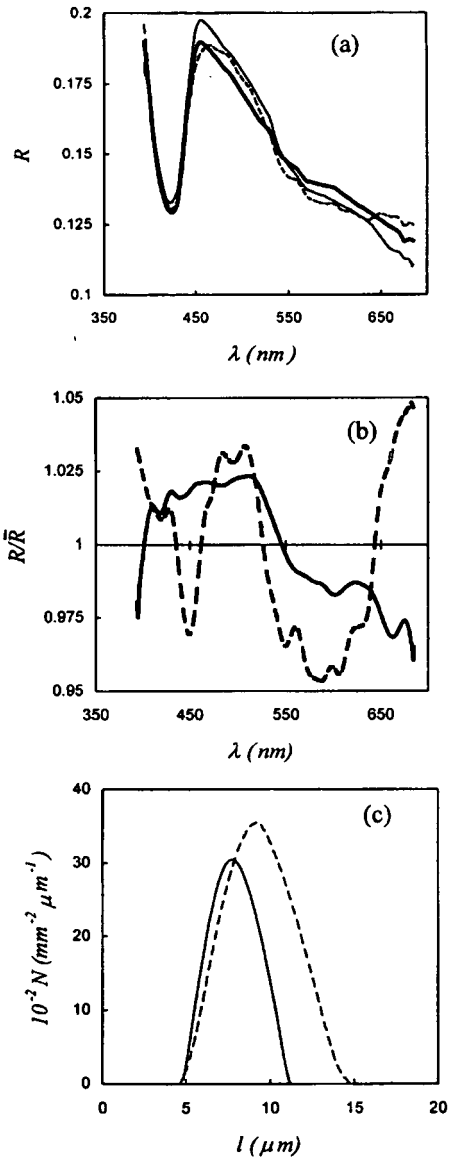

FIG. 3. Reflectance from Barrett's esophagus. (a) Diffuse reflectance from a nondysplastic site (solid line), a dysplastic site (dashed line), and the model fit (thick solid line); (b) corresponding fine structures; (c) resulting nuclear size distributions.

absorption have to be taken into account in modeling the background signal.

We employed a simple physical model to describe this background. Light incident on the tissue is assumed to be exponentially attenuated, and that, at any given depth z, an amount of light proportional to the reduced scattering coefficient $\mu_s'(\lambda)$ is scattered back towards the surface and further exponentially attenuated. Since light attenuation depends on both scattering and absorption, the attenuation coefficient is assumed to be the sum of the absorption coefficient $\mu_a(\lambda)$ and an effective scattering coefficient $\mu_s^{(e)}(\lambda) = \beta\mu_s'(\lambda)$. The parameter β was determined by comparison with Monte Carlo simulations and more accurate models of light transport, and was found to be $\beta \cong 0.07$ [1,17]. Since light only penetrates $\sim$1 mm into the tissue, most of the diffusely scattered return light is confined to the mucosal layer. The following approximate expression for the diffusive light from underlying tissue impinging on the epithelial cell layer is then obtained [7]:

$$I_d(\lambda, \mathbf{s}) = F(\mathbf{s})\langle I_i(\lambda, \mathbf{s})\rangle_{\Omega_i} \frac{1 - \exp[-(\mu_s^{(e)} + c\mu_a)L]}{1 + c(\mu_a/\mu_s^{(e)})}, \quad (4)$$

where function $F(\mathbf{s}) = \frac{\Delta + (\mathbf{s}\cdot\mathbf{n})}{\pi(2\Delta+1)}$ describes the angular dependence of light emerging from the mucosal layer, $\mathbf{n}$ is a unit vector normal to the surface of the tissue, $\Delta = 0.7104$ [18], L is a parameter representing the thickness of the mucosal layer, and c is the relative concentration of hemoglobin. Because both oxygenated and deoxygenated hemoglobin are present, the total hemoglobin absorption is modeled as $\mu_a = (1 - \alpha)\mu_a^{(\mathrm{Hb})} + \alpha\mu_a^{(\mathrm{HbO_2})}$, with oxygen saturation parameter α ($0 \leq \alpha \leq 1$).

Figure 3(a) shows the reflectance spectra from two Barrett's esophagus tissue sites, independently diagnosed by two expert pathologists as nondysplastic (solid line) and dysplastic (dashed line), respectively. As can be seen, the differences in these unprocessed spectra are small. To analyze them, Eq. (4) was first fit to the broad features of the data by varying the parameters c, a, and L. As seen in Fig. 3(a), the resulting fits are quite accurate. After removing this coarse structure by calculating $R(\lambda)/\overline{R}(\lambda)$, the periodic fine structure is seen clearly [Fig. 3(b)]. Note that the fine structure from the dysplastic tissue site exhibits higher frequency content than that from the nondysplastic site. Equation (3) was then employed to extract the respective nuclear size distributions, yielding Fig. 3(c). As can be seen, the difference between nondysplastic and dysplastic tissue sites is pronounced. The distribution of nuclei from the dysplastic site is much broader than that from the nondysplastic site and the peak diameter is shifted from $\sim$7 mm to $\sim$10 mm. In addition, both the relative number of large nuclei (>10 mm) and the total number of nuclei are significantly increased. We further note that the method provides a quantitative measure of the density of nuclei close to the mucosal surface. These findings have been confirmed in a multipatient study, the results of which will be published elsewhere.

The ability to measure nuclear size distribution *in vivo* has valuable applications in clinical medicine. Enlarged nuclei are primary indicators of cancer, dysplasia, and cell regeneration in most human tissues. In addition, measurement of nuclei of different sizes can provide information about the presence of particular cells, and can thus serve, for example, as an indicator of inflammatory response of biological tissue. This suggests that different morphology/pathology at the mucosal surface will give rise to distinct patterns of nuclear size distributions. Additional studies are necessary to correlate the results of this work with pathology findings.

We thank D. Menemenlis for fruitful discussions. This work was supported by NIH Grants No. P41RR02594 and No. CA53717.

[1] L. T. Perelman, J. Wu, I. Itzkan, and M. S. Feld, Phys. Rev. Lett. **72**, 1341 (1994).
[2] M. A. O'Leary, D. A. Boas, B. Chance, and A. G. Yodh, Phys. Rev. Lett. **69**, 2658 (1992).
[3] A. G. Yodh and B. Chance, Phys. Today **48**, No. 3, 34 (1995).
[4] M. R. Melamed, T. Lindmo, and M. L. Mendelsohn, *Flow Cytometry and Sorting* (Wiley-Liss, New York, 1990).
[5] J. R. Mourant, T. Fuselier, J. Boyer, T. M. Johnson, and I. Bigio, Appl. Opt. **36**, 949 (1997).
[6] P. D. Kaplan, A. D. Dinsmore, A. G. Yodh, and D. J. Pine, Phys. Rev. E **50**, 4827 (1994).
[7] G. Zonios, L. T. Perelman, V. Backman, R. Manoharan, J. Van Dam, and M. S. Feld (to be published).
[8] R. S. Cotran, S. L. Robbins, and V. Kumar, *Robbins Pathological Basis of Disease* (Saunders, Philadelphia, 1994).
[9] J. Beuthan, O. Minet, J. Helfmann, M. Herrig, and G. Muller, Phys. Med. Biol. **41**, 369 (1996).
[10] P. M. A. Slot, A. G. Hoekstra, and C. G. Figdor, Cytometry **9**, 636 (1988).
[11] H. C. van de Hulst, *Light Scattering by Small Particles* (Dover, New York, 1957).
[12] R. G. Newton, *Scattering Theory of Waves and Particles* (McGraw-Hill, New York, 1969).
[13] A. Ishimaru, *Wave Propagation and Scattering in Random Media* (Academic Press, Orlando, 1978).
[14] J. F. Brennan, G. I. Zonios, T. D. Wang, R. P. Rava, G. B. Hayes, R. R. Dasari, and M. S. Feld, Appl. Spectrosc. **47**, 2081 (1993).
[15] Because of insufficient morphometric data, the nuclear size distribution for the normal cell culture sample of Fig. 2 is depicted as a Gaussian distribution with mean diameter and standard deviation determined from the light microscopy measurements.
[16] G. I. Zonios, R. M. Cothren, J. T. Arendt, J. Wu, J. Van Dam, J. M. Crawford, R. Manoharan, and M. S. Feld, IEEE Trans. Biomed. Eng. **43**, 113 (1996).
[17] J. Wu, M. S. Feld, and R. P. Rava, Appl. Opt. **32**, 3585 (1993).
[18] P. M. Morse and H. Feshbach, *Methods of Theoretical Physics* (McGraw-Hill, New York, 1953).

GASTROENTEROLOGY 2001;120:1620–1629

Fluorescence, Reflectance, and Light-Scattering Spectroscopy for Evaluating Dysplasia in Patients With Barrett's Esophagus

IRENE GEORGAKOUDI,* BRIAN C. JACOBSON,† JACQUES VAN DAM,† VADIM BACKMAN,* MICHAEL B. WALLACE,§ MARKUS G. MÜLLER,* QINGGUO ZHANG,* KAMRAN BADIZADEGAN,‖ DON SUN,¶ GORDON A. THOMAS,* LEV T. PERELMAN,* and MICHAEL S. FELD*

*G.R. Harrison Spectroscopy Laboratory, Massachusetts Institute of Technology, Cambridge, Massachusetts; †Division of Gastroenterology, Department of Medicine, Brigham & Women's Hospital, Harvard Medical School, Boston, Massachusetts; §Digestive Disease Center, Medical University of South Carolina, Charleston, South Carolina; ‖Department of Pathology, Children's Hospital, Harvard Medical School, Boston, Massachusetts; ¶Statistics Department, Lucent Technologies, Inc., Bell Laboratories, Murray Hill, New Jersey

Background & Aims: The aim of this study was to assess the potential of 3 spectroscopic techniques (fluorescence, reflectance, and light-scattering spectroscopy) individually and in combination, for evaluating low- and high-grade dysplasia in patients with Barrett's esophagus (BE). *Methods:* Fluorescence spectra at 11 excitation wavelengths and a reflectance spectrum were acquired in approximately 1 second from each site before biopsy using an optical fiber probe. The measured fluorescence spectra were combined with the reflectance spectra to extract the intrinsic tissue fluorescence. The reflectance spectra provided morphologic information about the bulk tissue, whereas light-scattering spectroscopy was used to determine cell nuclear crowding and enlargement in Barrett's epithelium. *Results:* Significant differences were observed between dysplastic and nondysplastic BE in terms of intrinsic fluorescence, bulk scattering properties, and levels of epithelial cell nuclear crowding and enlargement. The combination of all 3 techniques resulted in superior sensitivity and specificity for separating high-grade from non–high-grade and dysplastic from nondysplastic epithelium. *Conclusions:* Intrinsic fluorescence, reflectance, and light-scattering spectroscopies provide complementary information about biochemical and morphologic changes that occur during the development of dysplasia. The combination of these techniques (Tri-Modal Spectroscopy) can serve as an excellent tool for the evaluation of dysplasia in BE.

Adenocarcinoma of the lower esophagus develops almost exclusively in patients with Barrett's esophagus (BE), a condition characterized by the presence of metaplastic columnar epithelium.[1] Although the prognosis of patients diagnosed with adenocarcinoma is poor, the chances of successful treatment increase significantly if the disease is detected at the dysplastic stage.[2] The surveillance of patients with BE for dysplasia is challenging in 2 respects. First, dysplasia is not visible during routine endoscopy.[3] Thus, numerous random biopsy specimens are required. Second, the histopathologic diagnosis of dysplasia is problematic because there is poor interobserver agreement on the classification of a particular specimen, even among expert gastrointestinal pathologists.[4,5]

Optical techniques, such as fluorescence,[6–13] reflectance, and light-scattering[14] spectroscopies or optical coherence tomography[15–18] may significantly enhance the endoscopist's ability to detect these early dysplastic changes in BE. Indeed, fluorescence spectroscopy studies using exogenous fluorophores, such as Photofrin (QLT, Vancouver, Canada) and aminolevulinic acid–induced protoporphyrin IX, show that there is a significant difference between the measured red fluorescence of the carcinomatous and nondysplastic tissue as a result of the preferential accumulation of the drug.[10–13] Initial autofluorescence spectroscopy studies performed at 410 nm excitation report promising results for detecting high-grade dysplasia.[6–9] However, focal high-grade and low-grade lesions could not be detected reliably.

The aim of this study is to show that a combination of spectroscopic techniques can improve the sensitivity and accuracy of dysplasia detection in patients with BE. We show that fluorescence, reflectance, and light-scattering spectroscopies provide complementary information about the biochemical, architectural, and morphologic state of tissue and the corresponding changes that occur during the progression of dysplasia.

The need for using reflected light to correct for the effects of hemoglobin absorption on the measured integrated tissue fluorescence intensity has been recognized

Abbreviations used in this paper: BE, Barrett's esophagus; EEM, excitation-emission matrix; LSS, light-scattering spectroscopy; NADH, reduced nicotinamide adenine dinucleotide; PC, principal component.

0016-5085/01/$35.00
doi:10.1053/gast.2001.24842

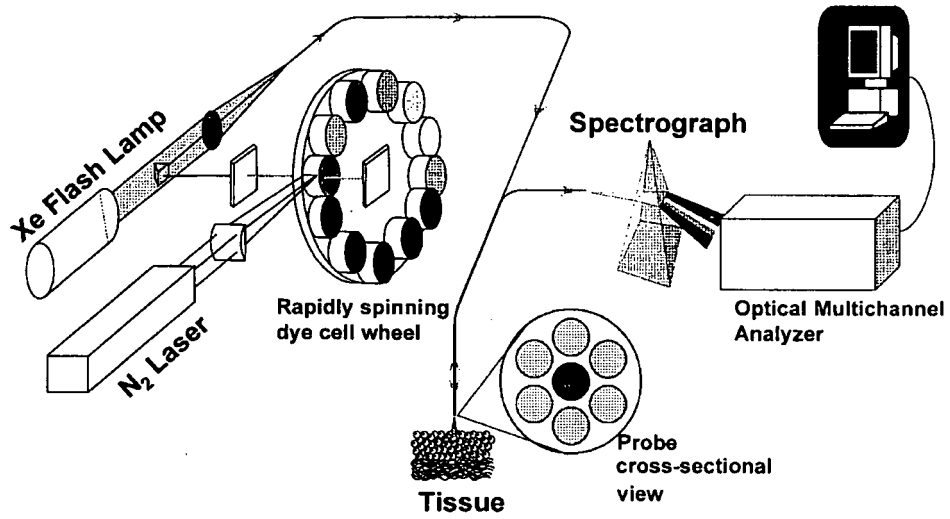

Figure 1. Schematic of fast EEM instrument. During endoscopy, the probe was inserted into the accessory channel of the endoscope and brought into gentle contact with the tissue, thus providing a fixed delivery-collection geometry. The reflected and fluorescence light was collected by the probe and coupled to a spectrograph and detector. The average of 3 sets of spectra from each site was used for analysis. Immediately after spectral acquisition, the probe was removed and a slight demarcation remained on the tissue for 30–60 seconds as a result of the probe contact. This endoscopically apparent marker was used as a guide for taking a biopsy specimen from the same site at which spectra were acquired. The biopsy specimen was interpreted and classified by an experienced gastrointestinal pathologist. If a dysplastic lesion was suspected, the specimen was reviewed and the diagnosis confirmed by a second gastrointestinal pathologist, in accordance with the standard of care. Data were analyzed from 26 nondysplastic BE sites (9 patients), 7 low-grade (4 patients), and 7 high-grade (5 patients) dysplastic sites.

and implemented by several groups in animal studies.[19–21] We illustrate, for the first time to our knowledge in a clinical setting, how the combination of fluorescence and reflectance spectroscopies can be applied to remove distortions introduced by scattering and absorption into the entire measured tissue fluorescence spectrum. The undistorted fluorescence can serve as a sensitive indicator of tissue biochemistry, whereas reflectance and light-scattering spectroscopies provide morphologic information on tissue architecture and epithelial cell nuclei. This is the first report of the simultaneous use of all 3 spectroscopic techniques for characterizing tissue and diagnosing disease. Our results show that the combined use of all 3 techniques (Tri-Modal Spectroscopy) provides superior results compared with the results of each technique individually, in terms of detecting not only high-grade, but also low-grade, dysplastic changes in BE.

Materials and Methods

The study was conducted at the Brigham and Women's Hospital and the West Roxbury Veterans Administration Medical Center. The protocol was approved by the Institutional Review Boards of both hospitals, as well as by the Committee On the Use of Humans as Experimental Subjects of the Massachusetts Institute of Technology. Data were collected from 16 patients with known BE undergoing standard surveillance protocols.

Measurements were performed using a fast excitation-emission matrix (EEM) instrument developed in our laboratory.[22] The excitation light source of this fast EEM system consisted of a 337-nm nitrogen laser (model VSL-337MD; Laser Science, Inc., Franklin, MA) pumping 10 dye cuvettes precisely mounted on a rapidly rotating wheel. In this manner, 11 different excitation wavelengths were obtained between 337 and 620 nm and coupled into the delivery fiber of a 1-mm diameter optical fiber probe. For the reflectance measurements, white light (350–700 nm) from a Xe flash lamp (Perkin Elmer Optoelectronics, Salem, MA) was coupled into the same probe. The probe was composed of 6 collection fibers surrounding the central light delivery fiber, and it was covered with a protective, transparent optical shield[23] (Figure 1).

Three types of spectroscopic information were acquired in less than 1 second. Fluorescence spectra at 11 different excitation wavelengths, reflectance spectra, and light-scattering spectra were obtained. Each type of spectrum was analyzed in a manner that provided information about biochemical and morphologic changes that occur during dysplastic transformation.

Fluorescence spectroscopy can provide valuable information about changes that take place in tissue biochemistry during the development of dysplasia. However, the measured tissue fluorescence spectra can be distorted significantly by unrelated scattering and absorption events. To remove these distortions, the fluorescence spectra were analyzed in combination with information from the corresponding reflectance spectra.[24,25] The success of this simple model is predicated on the fact that fluorescence and reflectance spectra collected from a specific

site using the same light delivery/collection geometry undergo similar distortions. By extracting the intrinsic (undistorted) tissue fluorescence, changes in tissue biochemistry were isolated in a more sensitive and specific manner.

Principal component (PC) analysis[26] and logistic regression[27,28] were used to determine the correlation between spectral features of the intrinsic fluorescence and histopathologic diagnosis. PC analysis is a statistical tool that generates a minimal set of basis spectra (PCs) from an experimental data set. These PCs can be combined linearly to describe accurately the experimental spectra. PCs are numbered in a manner that corresponds to the amount of variance they represent in the data. Thus, the first PC accounts for the spectral features that vary the most, and subsequent PCs represent features with progressively smaller variance. Usually, only a relatively small number of PCs are required to fit the spectra to within the accuracy of the noise. Only PCs that described meaningful and significant spectral changes were included in the second step of our statistical analysis.

To analyze this relatively small data set in an unbiased manner, leave-one-out cross-validation[29,30] was used. Specifically, the PCs of the intrinsic fluorescence spectra that described the spectral features that change during the progression of dysplasia were selected. The corresponding scores (the coefficients describing the contributions of the principal components to the overall spectra) were used to determine our ability to distinguish (1) high-grade dysplasia from low-grade dysplastic and nondysplastic BE, and (2) dysplastic (low- and high-grade) from nondysplastic BE. To achieve that in an unbiased manner, the following cross-validation procedure was performed. The scores from a particular site were eliminated, and logistic regression was used to form a decision surface that classified the remaining sites in a manner that optimized agreement with the histopathological classification. The resulting decision surface was then used to classify the excluded site. This process was repeated for each of the sites. This method, known as leave-one-out or jackknife cross-validation, provided optimal use of a relatively small data set to validate the performance of a decision surface without bias.[29,30] The decision surface varied minimally during this procedure, indicating the robustness of the technique. Sensitivity and specificity values were determined by comparing the spectroscopic classification with histopathology. Statistical analysis was performed using Matlab statistics software (The MathWorks, Inc., Natick, MA).

The measured reflectance spectra were analyzed using a model based on a diffusion theory, which expressed the reflected light as a function of the absorption (μ_a) and reduced scattering (μ_s') coefficients of tissue.[31] This analysis provided information about the architecture and morphology of mainly the connective tissue,[32] i.e., the lamina propria and the submucosa, because the collected light originated within 500–700 μm from the tissue surface and the epithelium in Barrett's esophagus consists mainly of a single cell layer. A linear fit was performed to describe the wavelength dependence of μ_s'. The diagnostic value of the slope and intercept of this line was determined by correlating the results of logistic regression and cross-validation with histopathological classification, as in the intrinsic fluorescence case.

Light-scattering spectroscopy (LSS) was used to characterize the epithelial cell nuclei.[33,34] LSS spectra were extracted from the reflectance data by subtracting the diffuse component provided by the model of Zonios et al.[31] The LSS signal comprised a small fraction of the reflected light and was caused by photons that were singly backscattered by the cell nuclei. The intensity of the LSS spectrum varied in wavelength in an oscillatory manner. The frequency of these oscillations are proportional to the size of the scatterers (cell nuclei), and the depth of the modulations is proportional to the density of the scatterers, which in this case is indicative of nuclear crowding.[33] These variations were analyzed using a model based on the theory of light scattering to determine the number and size of the epithelial cell nuclei.[33] Logistic regression and cross-validation were then used to compare the spectroscopic classification with that of histopathology. To optimize sensitivity and specificity, the posterior probability threshold for separating high-grade dysplasia from non–high-grade dysplasia sites was set to 0.3.

Finally, results from all 3 spectroscopic techniques were combined to determine whether the number of correctly classified sites could be improved. Specifically, a site was assigned a classification that was consistent with the results from at least 2 of the 3 analysis methods, and this classification was compared with histopathology.

Results

Extracting the Intrinsic Tissue Fluorescence

Figure 2*A* shows a typical fluorescence spectrum excited with 337 nm light from a nondysplastic BE site (solid line). There are 2 peaks, which might be attributed to the presence of 2 different tissue fluorophores. However, note that the fluorescence intensity decrease between these 2 peaks occurs in the 420-nm wavelength range, where hemoglobin absorbs light very efficiently. The effects of hemoglobin absorption are clearly observed in the corresponding reflectance spectrum, which exhibits minima at approximately 420, 540, and 580 nm, corresponding to oxyhemoglobin absorption peaks (Figure 2*B*).

When the measured fluorescence spectrum of Figure 2*A* is processed in combination with the corresponding reflectance spectrum of Figure 2*B* as discussed in Materials and Methods, the intrinsic (undistorted) tissue fluorescence spectrum at the particular excitation wavelength is obtained (Figure 2*A*, dashed line). Note that this spectrum consists of a single broad peak.

Significant differences are observed in the modeled intrinsic tissue fluorescence of nondysplastic and dysplastic BE sites excited at 337 nm (Figure 3*A* and *B*) and 397

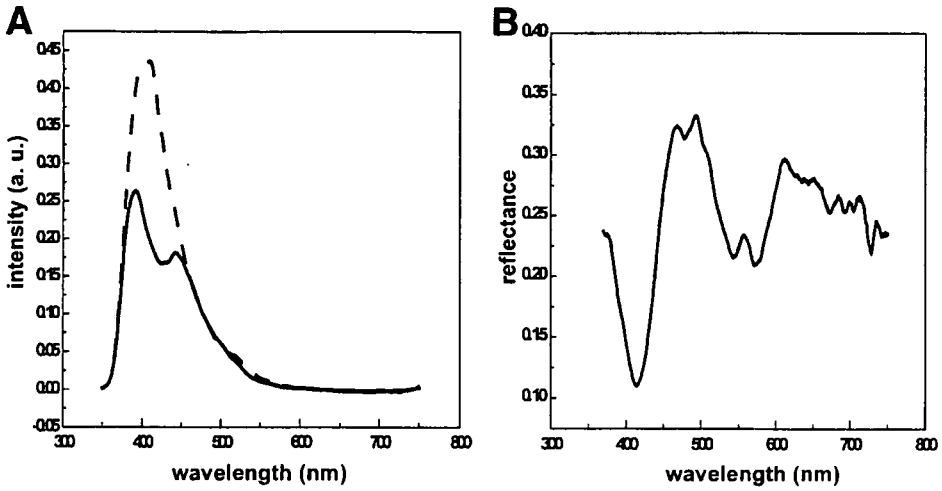

Figure 2. (*A*) Fluorescence from a nondysplastic BE site, 337-nm excitation. Measured spectrum, solid line; extracted intrinsic fluorescence, dashed line. (*B*) Corresponding reflectance spectrum.

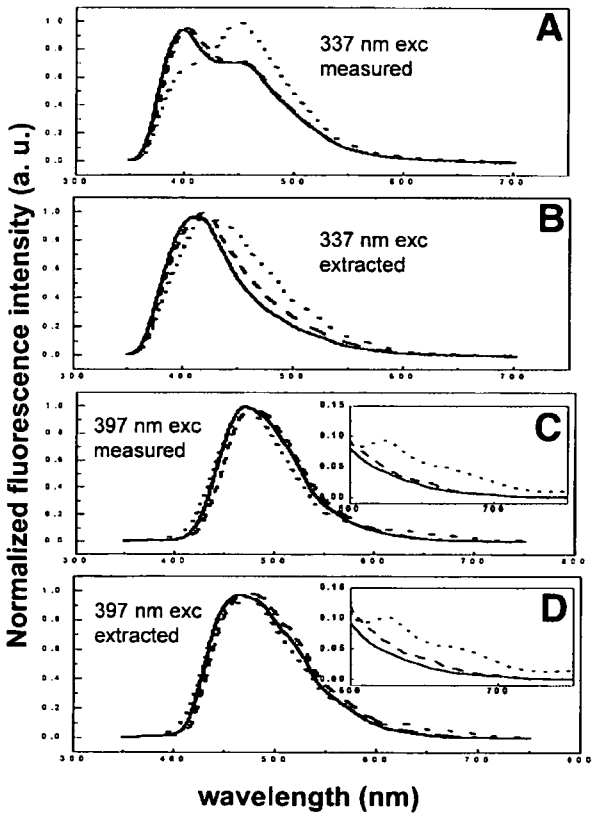

Figure 3. Mean fluorescence spectra from nondysplastic (*solid lines*), low-grade (*dashed lines*), and high-grade dysplastic (*dotted lines*) BE sites. Measured and corresponding extracted intrinsic fluorescence for excitation at 337 nm and 397 nm are shown. The insets in (*C*) and (*D*) show a magnified view of the corresponding spectra in the 600–750-nm region. Spectra are normalized to their peak intensities. Note the significant line-shape changes.

nm (Figure 3*C* and *D*). At 337-nm excitation, the line-shape of the dysplastic sites broadens and shifts to the red region of the spectrum during the progression from nondysplastic, to low-grade, to high-grade dysplasia. At 397-nm excitation, the fluorescence increases in the red region of the spectrum for the dysplastic BE sites. Similar changes are observed at 412-nm excitation (data not shown).

These differences can be exploited to develop algorithms for detecting dysplasia in BE. Specifically, principal component analysis, logistic regression, and leave-one-out cross-validation are used to determine the sensitivity and specificity with which we can separate (1) nondysplastic from dysplastic (low- and high-grade) tissue, and (2) high-grade dysplasia from low-grade and nondysplastic BE epithelium. In each case, the scores of 1 of the first 2 principal components extracted from the intrinsic fluorescence spectra at 337-, 397-, and 412-nm excitation are used (Figures 4 and 5). The selected principal components describe the observed spectral differences already discussed. From this analysis, sites with high-grade dysplasia can be differentiated from low-grade and nondysplastic sites with high levels of sensitivity and specificity (Table 1). Additionally, dysplastic and nondysplastic epithelia can be distinguished with very high sensitivity and specificity (Table 1).

Reflectance Spectroscopy

As discussed in Materials and Methods, the reflectance spectra can be analyzed using a mathematical model to obtain detailed information about the scattering and absorption properties of the bulk tissue. A typical reflectance spectrum with the corresponding fit obtained using this model is shown in Figure 6.

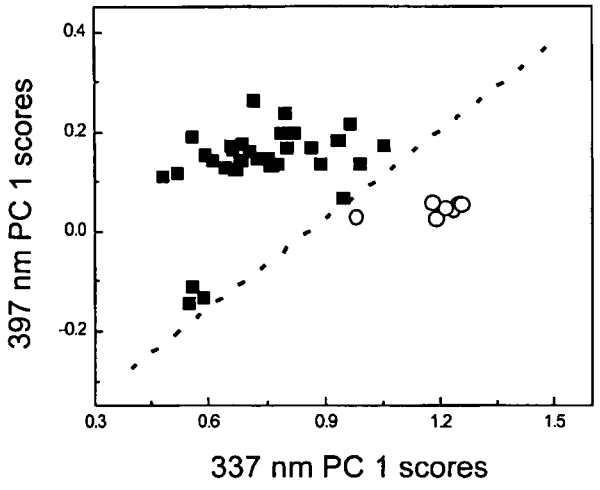

Figure 4. Scores of 2 principal components extracted from decomposition of intrinsic fluorescence spectra at 337- and 397-nm excitation used to distinguish high-grade dysplasia (○) from nondysplastic and low-grade dysplasia (■) BE sites. At 337-nm excitation, decomposition was performed in the 460–520-nm region of the intrinsic fluorescence spectra because this is the wavelength range within which spectral differences are most pronounced. Similarly, at 397-nm excitation, principal components were extracted from the intrinsic fluorescence spectra between 600 and 650 nm. PC 1, first principal component. The dotted line represents the logistic regression decision line for the entire data set.

Table 1. Accuracy of Spectroscopic Classification of Nondysplastic, Low-grade, and High-grade Dysplastic Tissue in BE

	HGD vs. LGD and NDB		LGD and HGD vs. NDB	
	Sensitivity	Specificity	Sensitivity	Specificity
Intrinsic fluorescence (IF)	100%	97%	79%	88%
Diffuse reflectance (DR)	86%	100%	79%	88%
Light scattering (LS)	100%	91%	93%	96%
Combination of IF, DR, and LS	100%	100%	93%	100%

HGD, High-grade dysplastic; LGD, low-grade dysplastic; NDB, nondysplastic Barrett's esophagus.

This analysis shows that the reduced scattering coefficient, μ_s', of Barrett's esophagus tissue changes gradually during the progression from nondysplastic, to low-grade, to high-grade dysplasia. For example, at 400 nm, the μ_s' of high-grade dysplastic tissue (1.3 ± 0.2 mm^{-1}) is lower than that of low-grade dysplastic tissue (1.8 ± 0.3 mm^{-1}), which, in turn, is lower than that of nondysplastic BE tissue (3 ± 1.6 mm^{-1}). Additionally, the wavelength dependence of μ_s' changes during the development of dysplasia. To describe these changes, a straight line is fit to $\mu_s'(\lambda)$ and the intercept at 0 nm and slope of this line are used as diagnostic parameters (Figure 7). Using logistic regression and leave-one-out cross-validation, the sensitivity and specificity for classifying tissue in accordance with histopathology are determined.

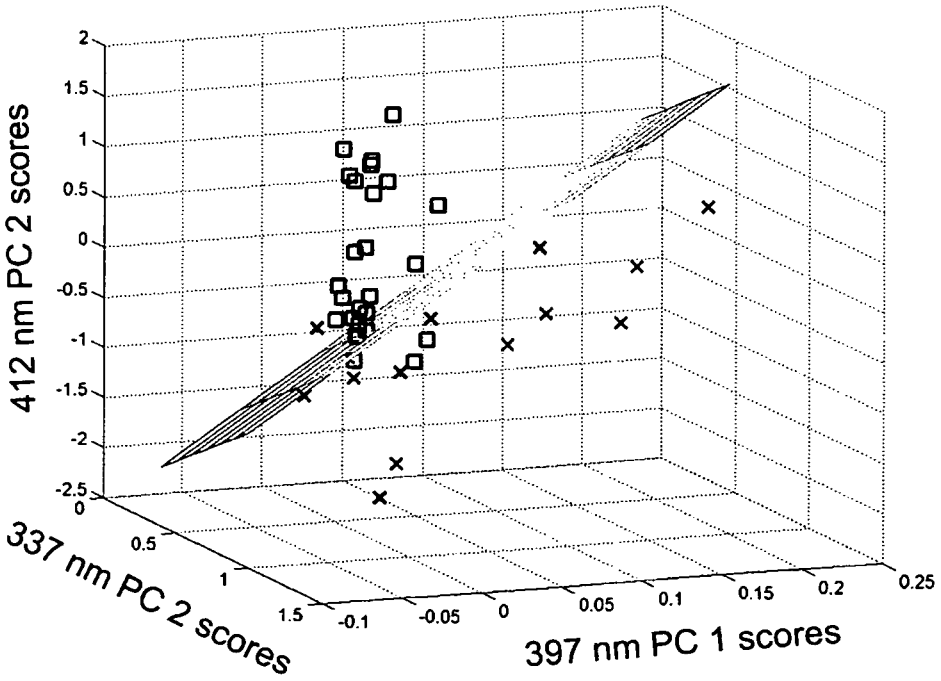

Figure 5. Scores of 3 principal components extracted from decomposition of the intrinsic fluorescence spectra excited at 337 (460–520-nm emission), 397 (600–650-nm emission), and 412 nm (360–750-nm emission) used to distinguish dysplastic (low- and high-grade; ×) from nondysplastic (□) BE sites. PC 1, first principal component; PC 2, second principal component. The logistic regression decision plane for the entire data set is also shown.

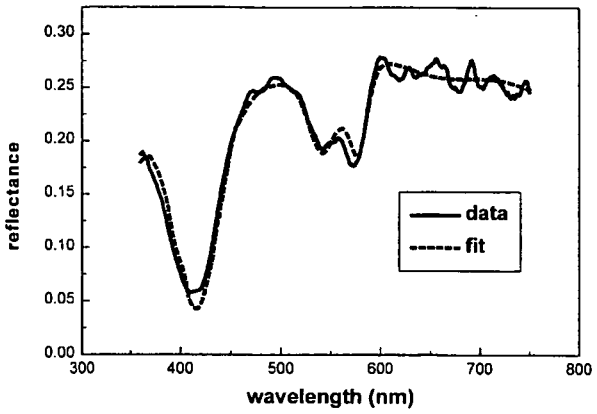

Figure 6. Reflectance spectrum of a nondysplastic BE site. *Solid line*, experimental data; *dashed line*, model fit.

This method results in slightly lower overall sensitivity and specificity values than those achieved with the intrinsic fluorescence spectra (Table 1).

Light-Scattering Spectroscopy

The reflectance spectra are further processed in a manner that allows extraction and analysis of the reflected light scattered from the epithelial cell nuclei. The results of this analysis are displayed in Figure 8. The ordinate of this figure represents the number of nuclei per square millimeter, indicative of the degree of nuclear crowding, and the abscissa represents the percentage of enlarged nuclei, defined as nuclei having a diameter >10 μm. Note that the nondysplastic samples are concentrated in the lower left-hand corner, indicating cell nuclei that are small and free of crowding. As dysplasia progresses, the data points move to the upper right, indicating nuclear enlargement and crowding, in agreement with the findings of histopathology. This technique is superior in terms of separating the dysplastic (low- and high-grade) from the nondysplastic BE sites (Table 1).

Combination of Spectroscopic Techniques for Optimal Diagnosis

The ability to characterize dysplastic and nondysplastic tissue in BE is improved by combining the information provided by each one of the spectroscopic techniques, obtained simultaneously with our system. When a spectroscopic classification is consistent with at least 2 of the 3 analysis methods, high-grade dysplasia is identified with very high sensitivity and specificity, and dysplastic tissue is distinguished from nondysplastic tissue with very high specificity, while maintaining high sensitivity (Table 1).

Discussion

Spectroscopic techniques use information contained in light signals to assess the state of biological tissue. Optical fiber technology allows spectroscopy to be applied as a diagnostic tool for a wide range of tissues that are accessible endoscopically. Indeed, the use of spectroscopy as a means of improving the physician's ability to detect precancerous (dysplastic) and early cancerous lesions is pursued actively in many organs, such as the oral cavity,[35–38] the cervix,[39,40] the lung,[41,42] the breast,[43] and the gastrointestinal tract.[6–14,44–46] Depending on the technique used, specific information can be acquired about tissue biochemical, architectural, and morphologic features. Microscopic changes in these features that occur during the progression of dysplasia may be detectable spectroscopically before the manifestation of macroscopic changes that are visible endoscopically. Additionally, spectroscopic techniques are noninvasive, allowing study of the tissue in its native state, free of

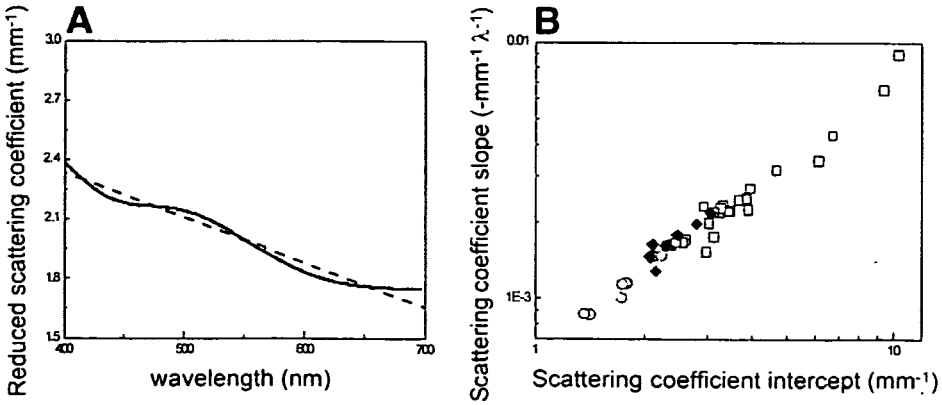

Figure 7. (*A*) Reduced scattering coefficient as a function of wavelength for a representative nondysplastic BE site (*solid line*) and corresponding linear fit (*dashed line*). (*B*) Slopes and intercepts of linear fit to the wavelength-dependent tissue reduced scattering coefficient, μ_s', for nondysplastic (□), low-grade (◆), and high-grade (○) dysplastic BE sites. A log-log scale is used to facilitate visualization of all the data points.

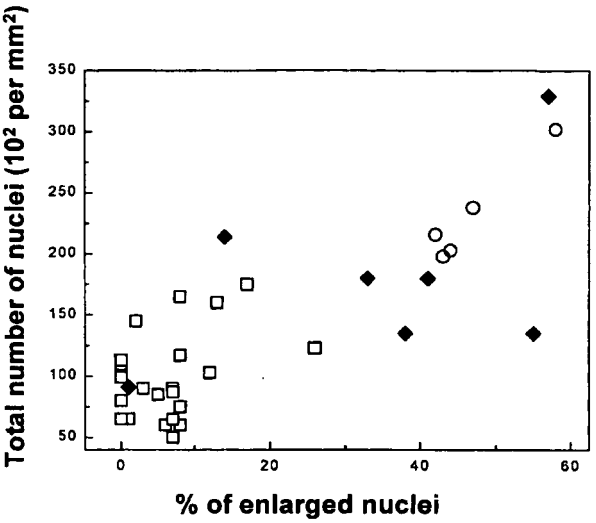

Figure 8. Total number of nuclei/mm² plotted as a function of percentage of enlarged nuclei (diameter >10 μm), as determined from the light-scattering model analysis. Nondysplastic BE, □; low-grade dysplasia, ◆; high-grade dysplasia, O.

artifacts introduced by cutting and chemically processing the tissue. In principle, spectroscopic signals can be analyzed in real time, thus guiding the physician to biopsy areas that are likely to yield significant pathology or possibly allowing the physician to make an immediate decision on the type of intervention that is required for the successful treatment of the patient. Furthermore, the spectroscopic signals carried by light can be used as objective guides for assessing a particular tissue site, especially in areas in which the intra- and interobserver agreement on the classification of disease is not very good.

In this report, we show the ability of 3 different spectroscopic techniques (fluorescence, reflectance, and light scattering) to characterize biochemical and morphologic changes that occur during the progression of dysplasia in BE. We show the different types of information that can be acquired and the way this information can be used to assist the physician in classifying a particular tissue area. The accuracy of these techniques is evident from the high sensitivity and specificity with which we can distinguish not only high-grade, but also low-grade dysplastic changes (Table 1). To our knowledge, this is the first report of a study in which multiple spectroscopic techniques are combined to provide superior results for the detection of early dysplastic changes and the classification of tissue in a manner that is consistent with histopathologic findings.

Fluorescence spectroscopy is under development in many areas as a diagnostic tool. The targets of fluorescence spectroscopy consist of tissue biochemicals such as reduced nicotinamide adenine dinucleotide (NADH), flavin adenine dinucleotide, collagen, elastin, and porphyrins. Exogenous or exogenously induced chromophores that have been shown to accumulate preferentially in the diseased areas can also be used. Promising results for the detection of high-grade dysplasia using tissue autofluorescence excited at 410 nm have been obtained by Vo-Dinh et al.[6-9] The difference between the measured integrated intensity-normalized fluorescence and the mean normalized fluorescence from normal esophageal tissue was used for the diagnostic algorithm. The main spectral features that resulted in good differentiation between high-grade dysplastic and nondysplastic tissues were the presence of decreased fluorescence around 470–480 nm and increased fluorescence in the red region of the spectrum for the high-grade dysplastic tissues. However, this algorithm could not classify correctly sites with low-grade or focal high-grade dysplasia.

In this study, we obtain fluorescence spectra at 11 different excitation wavelengths between 337 and 610 nm. Thus, instead of a single fluorescence spectrum, we have an EEM. EEMs can be used to identify the excitation wavelengths at which tissue classification is optimized. Additionally, EEMs can assist in identifying the origins of the measured fluorescence signals in a more reliable manner. Nevertheless, as shown in Figures 2 and 3, these measured EEMs can be distorted significantly by tissue scattering and absorption. To eliminate artifactual changes introduced by changes in scattering or absorption, rather than by tissue biochemistry, we use the corresponding reflectance spectra, which are affected in a similar manner by scattering and absorption events. Once the distorted measured tissue fluorescence spectra are rectified using the reflectance, we observe that tissue fluorescence excited at 337 nm broadens and shifts to longer wavelengths in a very consistent manner as the tissue progresses from nondysplastic to low-grade to high-grade dysplasia (Figure 3). These spectral changes are consistent with the presence of increased NADH levels in dysplastic tissue. Our findings at 397- and 412-nm excitation are consistent with the results of Vo-Dinh et al.[6-9] with respect to the differences in the red fluorescence, which is attributed to endogenous porphyrins. The spectra corresponding to the high-grade dysplasia sites appear slightly distorted around 470 nm, even after correcting for the effects of scattering and absorption. This suggests that this difference arises as a result of biochemical changes rather than absorption changes.

To demonstrate the level of significant changes that are observed in tissue fluorescence during the development of dysplasia, we use the scores of 1 of the first 3 principal components, which collectively describe over 99% of the variance observed in the intrinsic fluorescence spectra excited at 337, 397, and 412 nm. Subsequently, we use logistic regression and leave-one-out cross-validation to estimate and validate in an unbiased manner the sensitivity and specificity with which we can distinguish (1) high-grade dysplasia from low-grade and nondysplastic tissue, and (2) dysplastic (low- and high-grade) from nondysplastic tissue. We find that when we attempt to separate high-grade dysplasia from low-grade and nondysplastic tissue, spectroscopic classification is consistent with histopathology in all but 1 case. Additionally, we can distinguish dysplastic from nondysplastic tissue with very high sensitivity and specificity.

While these initial results are very promising, our ultimate goal is to decompose the intrinsic tissue fluorescence EEMs into EEMs of specific biochemicals, and thus to correlate the observed changes with particular changes in tissue biochemistry. Such knowledge of the events that take place during the progression of dysplasia should lead to improved detection capabilities and to improved understanding of dysplasia in general.

Reflectance spectroscopy can be used not only to remove the distortions observed in the measured tissue fluorescence spectra, but also to provide very detailed and potentially useful information about morphologic and architectural features of the tissue. Specifically, we show in Figure 6 that we can describe the observed tissue reflectance spectra in terms of 2 parameters that are determined by tissue scattering and absorption. For example, changes in the concentration or the oxygen saturation of hemoglobin, the main absorber in the visible spectrum for this tissue type, will result in concomitant changes in the absorption coefficient of tissue. Alterations in the architecture of the connective tissue collagen fibers, one of the main contributors of tissue scattering in diffuse reflectance measurements,[32] will lead to a modified tissue scattering coefficient. Indeed, our analysis suggests that the scattering coefficient of tissue decreases significantly during the development of dysplasia, suggesting that changes that are not observed histopathologically are taking place within the lamina propria and submucosa before the onset of invasion. Recently, it has been shown that an increased level of cysteine and serine proteases is found in gastric and colorectal cancerous and precancerous lesions.[47] Our findings related to the decrease in the value of the scattering coefficient during the progression of dysplasia are consistent with the presence of such enzymes, which could result in a less dense collagen matrix, for instance. The change in the slope of μ_s' as a function of wavelength suggests that the mean size of the tissue scattering particles is changing. Crowding of the cells and nuclei of the epithelial layer may be responsible for this change. As shown in Table 1, we can use the observed changes in tissue scattering to classify tissue quite successfully.

Light-scattering spectroscopy is a novel technique that can be used to obtain information about the number and the size of nuclei of the epithelial cell layer. Epithelial cell nuclei are the primary targets of reflected light that is singly scattered before it is collected by our probe. The intensity and oscillations of this singly backscattered light are characteristic of the number and size of its target nuclei. We have used this technique to characterize precancerous and early cancerous changes in the colon, the oral cavity, the bladder, and BE.[14,34] We include the results of this technique for the data set of this particular study to illustrate the information that can be acquired and combined with fluorescence and reflectance spectroscopies. We find that light-scattering spectroscopy outperforms the other 2 methods in terms of its ability to separate the dysplastic from the nondysplastic BE sites.

The combination of all 3 techniques is an extremely sensitive and specific tool for the detection of dysplasia in BE and provides superior results to any 1 of the techniques alone. In this case, the spectroscopic classification is in agreement with the histopathological one for all 7 high-grade dysplastic sites and 33 non–high-grade sites. Additionally, all sites are classified correctly as dysplastic or nondysplastic, with the exception of 1 site. The observed improvement is expected because each of the techniques examines different features of tissue biochemistry and morphology that can be altered during the development of dysplastic changes. We note that in a larger data set, less than perfect agreement is to be expected.

These very promising and substantial results demonstrate the ability of spectroscopic techniques to provide useful information for disease classification in a noninvasive manner. Although each of the techniques discussed in this article shows great potential as a means of detecting dysplasia in BE, their combination should allow us to create a comprehensive picture of the biochemical and morphologic state of tissue. Specifically, decomposition of the intrinsic tissue fluorescence EEMs into EEMs of biochemicals such as NADH and collagen will provide details about tissue biochemistry. Reflectance and light scattering spectroscopy yield morphologic information

related to the connective tissue and the epithelial cell nuclei. Because this information is free from artifacts introduced by tissue excision and processing, it can help advance the understanding of the processes that lead to the progression of dysplasia. Development of software for performing data analysis using all 3 types of spectroscopic information in real time at endoscopy will allow us to test the applicability of these techniques as a guide to performing biopsies in the near future. Extension of these methods to imaging modalities will enable large tissue areas to be studied rapidly.

References

1. Antonioli D. The esophagus. In: Henson D, Alobores-Saavdera J, eds. The pathology of incipient neoplasia. Philadelphia: Saunders, 1993:64–83.
2. Van Sandick JW, van Lanschot JJB, Kuiken BW, Tytgat GNJ, Offerhaus GJA, Obertop H. Impact of endoscopic biopsy surveillance of Barrett's esophagus on pathological stage and clinical outcome of Barrett's carcinoma. Gut 1998;43:216–222.
3. Cameron AJ. Management of Barrett's esophagus. Mayo Clin Proc 1998;73:457–461.
4. Reid BJ, Haggitt RC, Rubin CE, Roth G, Surawicz CM, Van Belle G, Lewin K, Weinstein WM, Antonioli DA, Goldman H, McDonald W, Owen D. Observer variation in the diagnosis of dysplasia in Barrett's esophagus. Hum Pathol 1988;19:166–178.
5. Petras RE, Sivak MV, Rice TW. Barrett's esophagus. A review of the pathologist's role in diagnosis and management. Pathol Annual 1991;26:1–32.
6. Panjehpour M, Overholt BF, Schmidhammer JL, Farris C, Buckley PF, Vo-Dinh T. Spectroscopic diagnosis of esophageal cancer: new classification model, improved measurements system. Gastrointest Endosc 1995;41:577–581.
7. Vo-Dinh T, Panjehpour M, Overholt BF, Farris C, Buckley RP, Sneed R. In vivo diagnosis of the esophagus using differential normalized fluorescence (DNF) indices. Lasers Surg Med 1995; 16:41–47.
8. Panjehpour M, Overholt B, Vo-Dinh T, Haggitt R, Edwards D, Buckley FP. Endoscopic fluorescence detection of high-grade dysplasia in Barrett's esophagus. Gastroenterology 1996;111:93–101.
9. Vo-Dinh T, Panjehpour M, Overholt BF. Laser-induced fluorescence for esophageal cancer and dysplasia diagnosis. Ann N Y Acad Sci 1998;838:116–122.
10. Stepp H, Sroka R, Baumgartner R. Fluorescence endoscopy of gastrointestinal diseases: basic principles, techniques, and clinical experience. Endoscopy 1998;30:379–386.
11. Messmann H, Knüchel R, Bäumler W, Holstege A, Schölmerich J. Endoscopic fluorescence detection of dysplasia in patients with Barrett's esophagus, ulcerative colitis, or adenomatous polyps after 5 aminolevulinic acid-induced protoporphyrin IX sensitization. Gastrointest Endosc 1999;49:97–101.
12. Braichotte DR, Wagnières GA, Bays R, Monnier P, van den Bergh HE. Clinical pharmacokinetic studies of Photofrin by fluorescence spectroscopy in the oral cavity, the esophagus, and the bronchi. Cancer 1995;75:2768–2778.
13. Staël von Holstein C, Nilsson AMK, Andersson-Engels S, Willén R, Walther B, Svanberg K. Detection of adenocarcinoma in Barrett's oesophagus by means of laser induced fluorescence. Gut 1996;39:711–716.
14. Wallace MB, Backman V, Perelman LT, Crawford JM, Fitzmaurice M, Seiler M, Badizadegan K, Shields SJ, Itzkan I, Dasari RR, Van Dam J, Feld MS. Endoscopic detection of dysplasia in patients with Barrett's esophagus using light-scattering spectroscopy. Gastroenterology 2000;119:677–682.
15. Bouma BE, Tearney GJ, Compton CC, Nishioka NS. High-resolution imaging of the human esophagus and stomach in vivo using optical coherence tomography. Gastrointest Endosc 2000;51: 467–474.
16. Sivak MV Jr, Kobayashi K, Izatt JA, Rollins AM, Ung-Runyawee R, Chak A, Wong RC, Isenberg GA, Willis J. High-resolution endoscopic imaging of the GI tract using optical coherence tomography. Gastrointest Endosc 2000;51:474–479.
17. Pitris C, Jesser C, Boppart SA, Stamper D, Brezinski ME, Fujimoto JG. Feasibility of optical coherence tomography for high-resolution imaging of human gastrointestinal tract malignancies. J Gastroenterol 2000;35:87–92.
18. Wallace M, Van Dam J. Enhanced gastrointestinal diagnosis: light-scattering spectroscopy and optical coherence tomography. Gastrointest Endosc Clin N Am 2000;10:71–80.
19. Mayevsky A, Chance B. Repetitive patterns of metabolic changes during cortical spreading depression of the awake rat. Brain Res 1974;65:529–533.
20. Mayevsky A, Chance B. Intracellular oxidation-reduction state measured in situ by a multichannel fiber-optic surface fluorometer. Science 1982;217:537–540.
21. Renault G, Raynal E, Sinet M, Muffat-Joly M, Berthier J, Cornillault J, Godard B, Pocidalo J. In situ double-beam NADH laser fluorimetry: choice of a reference wavelength. Am J Physiol 1984; 246(Heart Circ Physiol 15):H491–H499.
22. Zângaro RA, Silveira L, Manoharan R, Zonios G, Itzkan I, Dasari RR, Van Dam J, Feld MS. Rapid multiexcitation fluorescence spectroscopy system for in vivo tissue diagnosis. Appl Optics 1996;35:5211–5219.
23. Cothren RM, Hayes GB, Kramer JR, Sacks B, Kittrell C, Feld MS. A multifiber catheter with an optical shield for laser angiosurgery. Lasers Life Sci 1986;1:1–12.
24. Wu J, Feld MS, Rava RP. Analytical model for extracting intrinsic fluorescence in turbid media. Applied Optics 1993;32:3585–3595.
25. Zhang Q, Müller MG, Wu J, Feld MS. Turbidity-free fluorescence spectroscopy of biological tissue. Optics Lett 2000;25:1451–1453.
26. Jackson JE. A user's guide to principal components. New York: Wiley, 1991.
27. Fisher L, VanBelle G. Biostatistics: a methodology for the health sciences. New York: Wiley, 1993.
28. Pagano M, Gauvreau K. Principles of biostatistics. Belmont, CA: Duxbury Press, 1993.
29. Schumacher M, Hollander N, Sauerbrei W. Resampling and cross-validation techniques: a tool to reduce bias caused by model building? Stat Med 1997;16:2813–2827.
30. Van Houwelingen JC, Le Cessie S. Predictive value of statistical models. Stat Med 1990;9:1303–1325.
31. Zonios G, Perelman LT, Backman V, Manoharan R, Fitzmaurice M, Van Dam J, Feld MS. Diffuse reflectance spectroscopy of human adenomatous colon polyps in vivo. Appl Optics 1999;38: 6628–6637.
32. Saidi IS, Jacques SL, Tittel FK. Mie and Rayleigh modeling of visible-light scattering in neonatal skin. Appl Optics 1995;34: 7410–7418.
33. Perelman LT, Backman V, Wallace M, Zonios G, Manoharan R, Nusrat A, Shields S, Seiler M, Lima C, Hamano T, Itzkan I, Van Dam J, Crawford JM, Feld MS. Observation of periodic fine structure in reflectance from biological tissue: a new technique for measuring nuclear size distribution. Phys Rev Lett 1998;80: 627–630.
34. Backman V, Wallace M, Perelman LT, Arendt JT, Gurjar R, Müller MG, Zhang Q, Zonios G, Kline E, McGillican T, Shapsay S, Valdez T, Badizadegan K, Crawford JM, Fitzmaurice M, Kabani S, Levin

HS, Seiler M, Dasari RR, Itzkan I, Van Dam J, Feld MS. Detection of preinvasive cancer cells. Nature 2000;406:35–36.
35. Inaguma M, Hashimoto K. Porphyrin-like fluorescence in oral cancer: in vivo fluorescence spectral characterization of lesions by use of a near-ultraviolet excited autofluorescence diagnosis system and separation of fluorescent extracts by capillary electrophoresis. Cancer 1999;86:2201–2211.
36. Betz CS, Mehlmann M, Rick K, Stepp H, Grevers G, Baumgartner R, Leunig A. Autofluorescence imaging and spectroscopy of normal and malignant mucosa in patients with head and neck cancer. Lasers Surg Med 1999;25:323–234.
37. Gillenwater A, Jacob R, Ganeshappa R, Kemp B, El-Naggar AK, Palmer JL, Clayman G, Mitchell MF, Richards-Kortum R. Noninvasive diagnosis of oral neoplasia based on fluorescence spectroscopy and native tissue autofluorescence. Arch Otolaryngol Head Neck Surg 1998;124:1251–1258.
38. Dhingra JK, Perrault DF, McMillan K, Rebeiz EE, Kabani S, Manoharan R, Itzkan I, Feld MS, Shapshay S. Early diagnosis of upper aerodigestive tract cancer by autofluorescence. Arch Otolaryngol Head Neck Surg 1996;122:1181–1186.
39. Mitchell MF, Cantor SB, Ramanujam N, Tortolero-Luna G, Richards-Kortum R. Fluorescence spectroscopy for diagnosis of squamous intraepithelial lesions of the cervix. Obstet Gynecol 1999; 93:462–470.
40. Ramanujam N, Mitchell MF, Mahadevan-Jansen A, Thomsen SL, Staerkel G, Malpica A, Wright T, Atkinson N, Richards-Kortum R. Cervical precancer detection using a multivariate statistical algorithm based on laser-induced fluorescence spectra at multiple excitation wavelengths. Photochem Photobiol 1996;64:720–735.
41. Hung J, Lam S, LeRiche JC, Palcic B. Autofluorescence of normal and malignant bronchial tissue. Lasers Med Surg 1991;11:99–105.
42. Lam S, MacAulay C, Hung J, LeRiche J, Profio AE, Palcic B. Detection of dysplasia and carcinoma in situ with a lung imaging fluorescence endoscope device. J Thor Cardiovasc Surg 1993; 105:1035–1040.
43. Alfano RR, Tang GC, Pradhan A, Lam W, Choy DSJ, Opher E. Fluorescence spectra from cancerous and normal human breast and lung tissues. IEEE J Quantum Electron 1987;23:1806–1811.
44. Cothren RM, Richards-Kortum R, Sivak MV, Fitzmaurice M, Rava RP, Boyce GA, Doxtader M, Blackman R, Ivanc TB, Hayes GB, Feld MS, Petras RE. Gastrointestinal tissue diagnosis by laser-induced fluorescence spectroscopy at endoscopy. Gastrointest Endosc 1990;36:105–111.
45. Schomacker KT, Frisoli JK, Compton CC, Flotte TJ, Richter JM, Deutsch TF, Nishioka NS. Ultraviolet laser-induced fluorescence of colonic polyps. Gastroenterology 1992;102:1155–1160.
46. Mycek MA, Schomacker KT, Nishioka NS. Colonic polyp differentiation using time-resolved autofluorescence spectroscopy. Gastrointest Endosc 1998;48:390–394.
47. Herszenyi L, Plebani M, Carraro P, De Paoli M, Roveroni G, Cardin R, Foschia F, Tulassay Z, Naccarato R, Farinati F. Proteases in gastrointestinal neoplastic diseases. Clin Chim Acta 2000;291: 171–187.

Received June 27, 2000. Accepted February 8, 2001.

Address requests for reprints to: Irene Georgakoudi, Ph.D., Massachusetts Institute of Technology, G.R. Harrison Spectroscopy Laboratory, 77 Massachusetts Avenue, Room 6-014, Cambridge, Massachusetts 09139. e-mail: ireneg@mit.edu; fax: (617) 253-4513.

Supported by National Institutes of Health grants P41RR02594 and CA53717, and by an NIH NRSA fellowship (to I.G.).

Diffuse reflectance spectroscopy of human adenomatous colon polyps *in vivo*

George Zonios, Lev T. Perelman, Vadim Backman, Ramasamy Manoharan, Maryann Fitzmaurice, Jacques Van Dam, and Michael S. Feld

Diffuse reflectance spectra were collected from adenomatous colon polyps (cancer precursors) and normal colonic mucosa of patients undergoing colonoscopy. We analyzed the data by using an analytical light diffusion model, which was tested and validated on a physical tissue model composed of polystyrene beads and hemoglobin. Four parameters were obtained: hemoglobin concentration, hemoglobin oxygen saturation, effective scatterer density, and effective scatterer size. Normal and adenomatous tissue sites exhibited differences in hemoglobin concentration and, on average, in effective scatterer size, which were in general agreement with other studies that employ standard methods. These results suggest that diffuse reflectance can be used to obtain tissue information about tissue structure and composition *in vivo*.

OCIS codes: 170.6510, 170.7050, 290.4020.

1. Introduction

Steady-state diffuse reflectance spectroscopy is one of the simplest spectroscopic techniques for studying biological tissue. Light delivered to the tissue surface undergoes multiple elastic scattering and absorption, and part of it returns as diffuse reflectance carrying quantitative information about tissue structure and composition.

This technique can serve as a valuable supplement to standard histologic techniques. Histology entails the removal, fixation, sectioning, staining, and visual examination of a tissue sample under the microscope. Tissue removal is subject to sampling errors, particularly when the lesions are not visible to the eye. Also, the multiple-stage sample preparation process is time-consuming, labor intensive, and can introduce artifacts[1] that are due to cutting, freezing, and staining of the tissue. Most importantly, the result is largely qualitative in nature, even though quantitative information is available through techniques such as morphometry[2,3] and DNA ploidy analysis.[4]

Spectroscopy, in contrast, can provide information in real time, is not greatly affected by artifacts or sampling errors, and can provide quantitative information that is largely free of subjective interpretation. Because it does not require tissue removal, it can be conveniently used to examine extended tissue areas.

Several researchers have used diffuse reflectance spectroscopy to study biological tissues. To benefit fully from its advantages, a methodology is needed to connect the spectral features with the underlying biochemistry and morphology. Reports on a variety of human and animal tissues, both *in vivo* and *in vitro*, have been published. Semiempirical models have been used to measure blood content and hemoglobin (Hb) oxygen saturation in rat gastric mucosa[5] and rat pancreas.[6] Differences in the diffuse reflectance of rat brain were characterized empirically,[7] and empirical analysis was also employed to study human tissues *in vivo*, such as skin,[8] bladder,[9] and colon.[10,11] The results confirm that tissue reflectance provides valuable information, but the qualitative nature of the analyses limits the information obtained.

A few investigators have employed analytical models, often based on the diffusion approximation to the radiative transfer equation. Quantitative results

G. Zonios (zonios@helix.mgh.harvard.edu) is with the Wellman Laboratories of Photomedicine, BHX 630, Massachusetts General Hospital, Boston, Massachusetts 02114. L. T. Perelman, V. Backman, R. Manoharan, and M. S. Feld are with the George R. Harrison Spectroscopy Laboratory, Massachusetts Institute of Technology, Cambridge, Massachusetts 02139. J. Van Dam is with the Division of Gastroenterology, Brigham and Women's Hospital, Boston, Massachusetts 02115. M. Fitzmaurice is with the Department of Pathology, Case Western Reserve University, Cleveland, Ohio 44106.

Received 15 March 1999; revised manuscript received 12 July 1999.
0003-6935/99/316628-10$15.00/0

have been obtained in blood oximetry[12,13] and in the study of the optical properties of various animal tissues such as rat prostrate,[14] chicken breast,[15] and canine gut.[16] However, these models are mathematically complicated, making difficult the inversion of the measured spectra, which is needed to obtain the tissue optical parameters.

In the present study we employ an analytical method based on data collection with an optical fiber probe with fixed delivery and collection geometry. Data analysis is based on establishing a correspondence between the diffuse reflectance spectra and a physical tissue model composed of scatterers and absorbers with known optical properties. Analyzing spectra from this tissue model by using the analytical formulation, we develop a calibration algorithm that is simple to invert and accurately predicts the concentrations of the scatterers and absorbers. After the calibration is established, the algorithm is applied to tissue spectra. The composition of the physical tissue model is much simpler than that of actual tissue, providing insight into the nature of scattering and absorption in tissue by bypassing the large complexity associated with the origin and details of these tissue properties.

The present research is part of a series of studies applying spectral analysis to mucosal surfaces of tissues *in vivo*.[17,18] We study here adenomatous colon polyps, which are precursors of colon cancer. These polyps are a form of colonic dysplasia and are histologically similar to visually undetectable flat dysplasia; however, because they are readily detectable, we have chosen them as a test ground for this spectroscopic technique. We examine how the results of our analysis correlate with standard histological examination, how these results can be used for early detection of disease, and most importantly, how a spectroscopic tool can be applied *in vivo* to obtain information about tissue structure and composition.

2. Experimental Methods

Diffuse reflectance spectra were collected *in vivo* from adenomatous polyps on 13 patients undergoing routine colonoscopy, with informed consent. Multiexcitation fluorescence spectra were also collected at the same time; a detailed description of the instrumentation can be found elsewhere.[19] A xenon-arc flashlamp with an approximately 10-μs pulse duration and an average input energy of 4 J/pulse was used as a source of white light. An imaging spectrograph dispersed the collected light, and a gated diode array detector was employed for light detection in the 360–685-nm wavelength range. A 12-μs gate that was time synchronized with the lamp pulse was used to minimize background light from endoscopic illumination. The detector was controlled by a PC notebook computer in which the data were transferred and stored.

We delivered and collected the light using an optical fiber probe,[20,21] which was advanced through the accessory channel of the colonoscope and brought into contact with the tissue. The probe consisted of a central optical fiber for light delivery and six fibers for light collection arranged in a circle around the central fiber. All fibers had a 200-μm core diameter and a N.A. of 0.22, and they were packed tightly with no gap between them. The probe tip was fitted with a quartz shield approximately 1.5 mm in length and in diameter, which provided a fixed delivery and collection geometry with uniform circular delivery and collection spots in the form of overlapping cones with approximate radii of $r_d = 0.35$ mm and $r_c = 0.55$ mm, respectively. The tip was beveled at an angle of 17° to eliminate unwanted specular reflections from the shield–tissue interface.

The diffuse reflectance spectrum of a 20% by volume $BaSO_4$ powder suspension (which was determined to have a flat spectral response across the visible range, like solid $BaSO_4$) was used as a reference to take into account the spectral characteristics and the overall intensity of the xenon lamp. The probe was immersed in the suspension, and a reference diffuse reflectance spectrum was recorded prior to collection of each data set. Tissue spectra were calibrated by means of division by this reference spectrum, and diffuse reflectance was measured in units of this reference spectrum. Spectra were measured from a few different sites on every adenomatous polyp and from corresponding sites in the surrounding normal mucosa of the colon. Single-pulse excitation was used to avoid motion-related artifacts. The polyps were then removed and examined histologically, whereas the normal mucosal sites were not biopsied. Data that we present in this paper were collected on polyps characterized as adenomatous by histologic examination. Experimental methods related to the physical tissue model are discussed in Section 4.

3. Analytical Model

To model diffuse reflectance, we assumed biological tissue to be a homogeneous semi-infinite turbid medium with reduced scattering and absorption coefficients $\mu_s'(\lambda)$ and $\mu_a(\lambda)$, respectively (λ is the wavelength of light). Part of the incident light is absorbed in the tissue, whereas the nonabsorbed part is subject to multiple scattering and eventually emerges from the surface as diffuse reflectance. A certain fraction of this emerging light is collected by the probe, whereas the remaining part escapes undetected. The amount of the light collected depends on the optical properties $\mu_s'(\lambda)$ and $\mu_a(\lambda)$, as well as on the probe radius r_c. This radius serves as a scale length, enabling $\mu_s'(\lambda)$ and $\mu_a(\lambda)$ to be determined.

To model light collection by an optical probe, it is necessary to have knowledge of the spatial and the angular resolution of the diffuse reflectance on the surface of the tissue. As our starting point, we employ an expression derived by Farrell *et al.* who calculated the diffuse reflectance from a narrow beam of light incident on the surface of a semi-infinite turbid medium in the diffusion approximation.[22] They obtained the following expression for the diffuse reflec-

tance radial density $R(\lambda, r)$ at a distance r from the point of incidence:

$$R(\lambda, r) = \frac{z_0}{4\pi}\frac{\mu_s'}{\mu_s' + \mu_a}\left[\left(\mu + \frac{1}{r_1}\right)\frac{\exp(-\mu r_1)}{r_1^2} + \left(1 + \frac{4}{3}A\right)\left(\mu + \frac{1}{r_2}\right)\frac{\exp(-\mu r_2)}{r_2^2}\right], \quad (1)$$

with

$$\mu = [3\mu_a(\mu_a + \mu_s')]^{1/2}, \quad z_0 = \frac{1}{\mu_s' + \mu_a},$$

$$r_1 = (z_0^2 + r^2)^{1/2}, \quad r_2 = \left[z_0^2\left(1 + \frac{4}{3}A\right)^2 + r^2\right]^{1/2}.$$

The parameter A depends on the refractive index n of the medium ($A = 1$ for $n = 1$ and $A > 1$ for $n > 1$), but $R(\lambda, r)$ does not depend strongly on this parameter. A reasonable assumption for the average refractive index of colon tissue[23,24] is $n \cong 1.4$, so that[22] $A \cong 3.2$.

To find the total light collected by the probe, Eq. (1) must be integrated over the spatial extent of the light delivery and collection areas, characterized by radii r_d and r_c, respectively. Assuming the incident light intensity to be uniform over the entire delivery area, the diffuse reflectance $R_p(\lambda)$ collected by the probe is given by

$$R_p(\lambda) = \frac{1}{r_d^2}\int_0^{r_c} r dr \int_0^{2\pi} d\phi \int_0^{r_d} R(\lambda, |\mathbf{r} - \mathbf{r}'|) r' dr', \quad (2)$$

with $|\mathbf{r} - \mathbf{r}'| = (r^2 + r'^2 - 2rr' \cos\phi)^{1/2}$. The integrals in Eq. (2) can be evaluated numerically. However, in the spirit of obtaining a simple analytical expression for $R_p(\lambda)$, we assume point delivery of light and collection over a circular spot with an effective radius of $r_c' \simeq r_c$, obtaining the following expression:

$$R_p(\lambda) = 2\pi\int_0^{r_c'} R(r) r dr = \frac{\mu_s'}{\mu_s' + \mu_a}\left\{\exp(-\mu z_0) + \exp\left[-\left(1 + \frac{4}{3}A\right)\mu z_0\right] - z_0\frac{\exp(-\mu r_1')}{r_1'} - \left(1 + \frac{4}{3}A\right)z_0\frac{\exp(-\mu r_2')}{r_2'}\right\}, \quad (3)$$

with

$$r_1' = (z_0^2 + r_c'^2)^{1/2}, \quad r_2' = \left[z_0^2\left(1 + \frac{4}{3}A\right)^2 + r_c'^2\right]^{1/2}.$$

For a given probe geometry, there is an optimal value of r_c' that can be determined by one's calibrating Eq. (3) on a physical tissue model with known optical properties (Section 4). The advantage of one's using Eq. (3) is that it is much easier to invert than Eq. (2), which requires numerical integration.

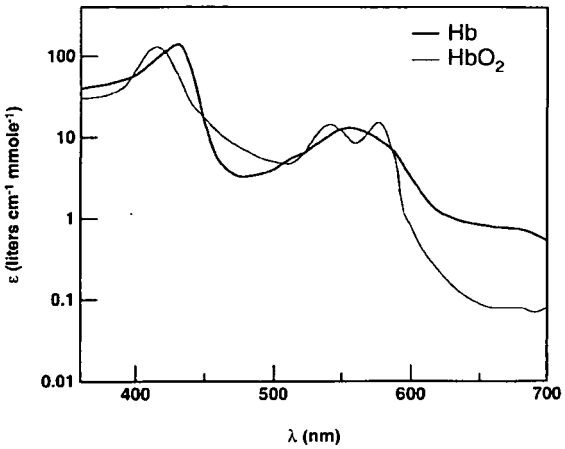

Fig. 1. Molar extinction coefficient spectra (per heme group) of the oxygenated (thin curve) and the deoxygenated (thick curve) Hb.[26] Note the characteristic peaks at 415, 542, and 577 nm [oxyhemoglobin (HbO_2)] and at 430 and 555 nm [deoxyhemoglobin (Hb)].

The parameter z_0 was calibrated in a similar way (Section 4) to correct for large values of the absorption coefficient ($\mu_a \simeq \mu_s'$), in which case it is known that there is a deviation from the diffusion approximation solution.[25] Finally, Eq. (3) is scaled by a constant factor R_0 that depends on the particular choice of the diffuse reflectance reference material (a 20% $BaSO_4$ suspension in our case, Section 2) and is determined by direct calibration with the tissue physical model.

Equation (3) can be used to analyze the diffuse reflectance spectra collected by the probe. From our study of the tissue spectra (discussed in Section 5), Hb appears to be the only significant light absorber in colon tissue in the visible range of the spectrum and is encountered in both oxygenated and deoxygenated forms. The light absorption properties of both forms have been well studied,[26] and their molar extinction coefficient spectra $\varepsilon_{HbO_2}(\lambda)$, $\varepsilon_{Hb}(\lambda)$ are shown in Fig. 1. Oxyhemoglobin (HbO_2) absorption presents a maximum at 415 nm and two secondary maxima at 542 and 577 nm, whereas deoxyhemoglobin has a maximum at 430 nm and only one secondary maximum at 555 nm. The total absorption coefficient $\mu_a(\lambda)$ is given by

$$\mu_a(\lambda) = \log_e 10\, c_{Hb}^*[\alpha\varepsilon_{HbO_2}(\lambda) + (1 - \alpha)\varepsilon_{Hb}(\lambda)], \quad (4)$$

where $\alpha = (c_{HbO_2})/(c_{HbO_2} + c_{Hb})$ is the Hb oxygen saturation parameter; c_{HbO_2} and c_{Hb} are the concentrations of oxy and deoxy Hb, respectively; and $c_{Hb}^* = c_{HbO_2} + c_{Hb}$ is the total concentration of Hb.

Determination of c_{Hb}^*, α, and $\mu_s'(\lambda)$ for both the physical tissue model spectra and the clinical spectra was performed in the following way. For a given reflectance spectrum $R_p(\lambda)$, initial values were assigned to c_{Hb}^* and α (typically $c_{Hb}^* = 0.0$ and $\alpha = 0.5$). Using the Hb molar extinction spectra of Fig. 1, we then numerically inverted Eq. (3) to find $\mu_s'(\lambda)$. The resulting $\mu_s'(\lambda)$ curve exhibited nonphysical Hb

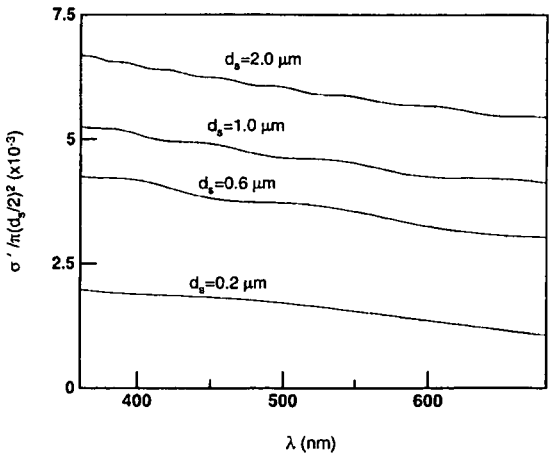

Fig. 2. Reduced scattering cross-section curves $\sigma'(\lambda, d_s)$ calculated by use of Mie theory for four different tissue scatterer diameters.

spectral peaks or valleys. This curve was smoothed with a moving window average of 7 nm. Using an iterative minimization routine,[27] we found the optimal values for c_{Hb}* and α by minimizing the difference between the experimental and the calculated $\mu_s'(\lambda)$ with the constraint that the derivative of $\mu_s'(\lambda)$ was everywhere negative. This ensured that the $\mu_s'(\lambda)$ curve exhibited a smooth spectral shape with no residual Hb spectral features. We established the success of this procedure by analyzing the reflectance spectra from the physical tissue model with known optical parameters (Section 4).

In general, $\mu_s'(\lambda)$ is the sum of contributions from the various tissue scatterers. Unfortunately, detailed information about these individual scatterers is not available. Therefore $\mu_s'(\lambda)$ was written as

$$\mu_s'(\lambda) = \rho_s \sigma'(\lambda), \quad (5)$$

with ρ_s being the effective scattering density and $\sigma'(\lambda)$ the effective reduced scattering cross section, i.e., the tissue scattering properties were modeled in an average way, as if tissue contained a single well-defined type of scatterer. In general, $\sigma'(\lambda)$ depends on the refractive index, shape, and size of the scatterer, as well as on the refractive index of the surrounding medium. For a homogeneous spherical scatterer of diameter d_s and relative refractive index n, $\sigma'(\lambda, d_s)$ can be evaluated numerically by use of Mie scattering theory.[28] In this study, the range of possible values for d_s was restricted to the range $0.35 < d_s < 1.5$ μm. This was done to obtain a scatterer size within a physically acceptable range. In addition, when $d_s > 1.5$ μm the slope of the scattering spectrum does not change significantly according to Mie theory.

Figure 2 shows several $\sigma'(\lambda, d_s)$ curves calculated in this way for various values of d_s. These curves are approximately straight lines, the slopes of which decrease[29,30] with increasing d_s. Using the Levenberg–Marquardt minimization method,[27] we fit the quantity $\rho_s\sigma'(\lambda, d_s)$ [with $\sigma'(\lambda, d_s)$ calculated by Mie theory] to the $\mu_s'(\lambda)$ curve derived from the clinical data. In this way, the scatterer size d_s and the scatterer density ρ_s were determined. In summary, for each tissue diffuse reflectance spectrum, four parameters were obtained: two absorption (c_{Hb}*, α) and two scattering (ρ_s, d_s) parameters.

In calculating the results of Fig. 2 and in analyzing the clinical data, we chose 1.4 and 1.36 as the values of the refractive indices of the scatterers and the surrounding medium, respectively, resulting in a relative refractive index of approximately 1.03. These values are consistent with those generally believed to be responsible for scattering in biological cells[30] and tissue in general.[23,24] The effective particle size d_s varied somewhat for different choices of the refractive indices, but the general trends in the spectral dependence of the reduced scattering curves were the same.

4. Physical Tissue Model

In this section we show that the approximate analytical expression, Eq. (3), provides a good representation of the data. We employ a physical tissue model with optical properties that span the actual range for colon tissue. We first establish that experimental spectra are accurately described by Eq. (3) by taking a series of spectra from the tissue physical model employing various values for the parameters (c_{Hb}*, α, ρ_s, d_s), evaluating Eq. (3) using these values, and comparing the predicted and the experimental spectra. We then demonstrate that, by the fitting of Eq. (3) to experimental data obtained using various values of Hb concentration, oxygen saturation, scatterer size, and scatterer density, the values of these parameters can be recovered with reasonable accuracy.

The physical tissue model samples consisted of mixtures of spherical microparticles that simulated tissue light scattering and Hb solutions that simulated absorption. The microparticles were polystyrene beads suspended in de-ionized water (Polysciences, Inc), with various diameters and densities. Hb solutions were prepared from lyophilized human Hb (Sigma, H0267), with various concentrations (0–250 mg/dl) and oxygen saturation values (0–100%). To vary the oxygen saturation, we used fresh human red blood cells,[31] and α was varied by our introducing a small amount of baking yeast,[31,32] which gradually converted Hb from its fully oxygenated to its fully deoxygenated state (diffuse reflectance owing to scattering by red blood cells was negligible). Scattering from the red blood cells (concentration ~20,000 mm^{-3}) was calculated to be approximately 2 orders of magnitude smaller than that by the polystyrene beads, so it was assumed to be negligible. Oxygen partial pressure (hence Hb oxygen saturation[31]) was monitored independently by means of an oxygen-sensitive microelectrode (Microelectrodes, Inc).

We calculated the scattering properties of the beads by using Mie theory.[28] The refractive index n_p of polystyrene was calculated with the expression[33]

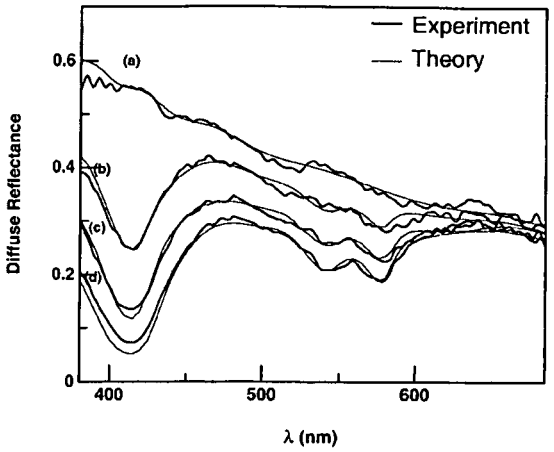

Fig. 3. Diffuse reflectance spectra measured on physical tissue models (thick curve) for four different HbO_2 concentrations: (a) 0.0 mg/dl, (b) 50 mg/dl, (c) 125 mg/dl, and (d) 250 mg/dl. The analytical model predictions by use of the same optical parameters are also shown (thin curve). As can be seen, the agreement between the analytical and the physical tissue model is good. Polystyrene beads with a 1.07-μm diameter and a density of 1.25×10^9 mm^{-3} were used, resulting in $\mu_s' \approx 1.7$–3.2 mm^{-1} across the spectrum.

$n_p = 1.5607 + 10{,}002/\lambda^2$ (λ in nanometers). Bead diameters ranged from 0.35 to 1.9 μm, and bead densities from 0.05 to 2.0×10^9 mm^{-3}. The spectral dependence of the reduced scattering coefficients of the beads was similar to that shown in Fig. 2, with the difference that for the beads the spectral slopes were generally larger because of the larger refractive index of polystyrene. Typical values for the μ_s' of the beads were in the range 0.5–3.0 mm^{-1}.

Because light absorption by polystyrene is negligible in the visible range, absorption was solely due to Hb. The size of the physical tissue model was approximately 3 cm × 3 cm × 0.5 cm, simulating the flat geometry of normal colon mucosa and underlying tissue layers. Additional geometries were investigated such as that of a cylinder with a 1-cm depth and a 0.5-cm diameter to simulate the geometry of a polyp, but no significant spectral differences were found because of the different geometry. The range of optical parameters was chosen based on previously reported independent measurements of colon tissue optical parameters performed *in vitro*.[17,34]

Figure 3 shows diffuse reflectance spectra obtained from the physical tissue model for several Hb concentrations ($\alpha = 1.0$, $\rho_s = 1.25 \times 10^9$ mm^{-3}, $d_s = 1.07$ μm). These spectra closely resemble the tissue spectra presented in Section 5 below. Similarly good results were obtained when the other parameters were varied. This indicates that our physical tissue model reproduces the features of actual tissue spectra well. On a quantitative level, Eq. (3) was found to predict accurately the physical tissue model spectra for tissue parameters in the physiological range of interest. This can be seen in Fig. 3 in which the spectra predicted by Eq. (3) for the known values of c_{Hb}^*, α, and μ_s' are shown as thin curves. In evaluating Eq. (3), the value of $r_c' = 0.45$ mm was used. This was determined to be the optimal value for r_c', and it was kept fixed throughout the subsequent data analysis. Similarly, the parameter z_0 was recalibrated to $z_0' = 1/(\xi\mu_a + \mu_s')$ with $\xi = 0.425 - 0.0425(\mu_s')/(\mu_a)$ for $(\mu_s')/(\mu_a) < 10$ and $\xi = 0$ for $(\mu_s')/(\mu_a) > 10$, which yielded a reasonable agreement between Eq. (3) and the physical tissue model spectra, even for large values of absorption. Finally, an overall intensity factor equal to 1.66 was used to scale Eq. (3). This factor, which was determined by direct comparison with the physical tissue model spectra, depends on the particular choice of the reference used to measure the diffuse reflectance (Section 2) and was kept fixed throughout the data analysis.

For Hb concentrations lower than 100 mg/dl, the deviation between the two models was always smaller than 10% over the entire wavelength range. The largest deviation occurred when absorption became comparable with scattering. This is shown in Fig. 3(d) near the peak of Hb absorption around 415 nm. The Hb concentration was in this case 250 mg/dl, which corresponds to an absorption coefficient of approximately 5 mm^{-1} at 415 nm.

The ability of the analytical model to determine accurately the parameter values of the physical tissue model was investigated over the full range of the four parameters. In this case, we employed Eq. (3) in an inverse manner, using the fitting procedure described in Section 3. Representative results are summarized in Table 1. As can be seen, in most cases the parameters of the physical tissue model can be recovered with an accuracy better than 10%. The results of this section establish that the experimental spectra are adequately described by Eq. (3) and that this expression can be used in an inverse manner to extract the parameters from the spectra with reasonable accuracy.

5. Results

Figure 4 shows typical diffuse reflectance spectra from one adenomatous polyp site and one normal mucosa site. Significant spectral differences are readily observable, especially in the short-wavelength region of the spectrum where the Hb absorption valley around 420 nm stands out as the prominent spectral feature. This valley is much more prominent in the adenomatous polyp spectrum, which also shows a continuous decrease in intensity starting from the red end (~700 nm) and moving toward the green region (~500 nm) of the spectrum, whereas in the same range the normal mucosa spectrum shows a steady increase in intensity. The secondary absorption dips of HbO_2 (542 and 577 nm) are much more prominent in the adenomatous polyp spectrum, indicating increased Hb presence. According to the model analysis, the normal mucosa spectrum was characterized by a Hb concentration of $c_{Hb}^* = 22.5 \pm 2.0$ mg/dl, whereas the corresponding value for the adenomatous polyp was approximately

Table 1. Comparison of the Parameters used in the Physical Tissue Model with Those Determined from Its Reflectance Spectra by Use of the Analytical Model[a]

Model Parameter	Physical Tissue Model	Analytical Model
Total Hb concentration c_{Hb}* (mg/dl)	0.0	0.01
(α = 1.0, ρ_s = 12.5 × 10^8 mm^{-3}, d_s = 1.07 μm)	10	9.2
	100	111
Hb oxygen saturation α	0.0	0.03
(c_{Hb}* = 50 mg/dl, ρ_s = 12.5 × 10^8 mm^{-3}, d_s = 1.07	0.5	0.54
μm)	1.0	0.97
Effective scatterer density ρ_s (×10^8 mm^{-3})	5.0	4.2
(c_{Hb}* = 50 mg/dl, α = 1.0, d_s = 1.07 μm)	10.0	10.8
	15.0	16.2
Effective scatterer size d_s (μm)	0.35	0.39
(c_{Hb}* = 50.0 mg/dl, α = 1.0, ρ_s = 12.5 × 10^8 mm^{-3})	1.07	1.15
	1.9	2.3

[a]Three typical values are shown for each model parameter.

6 times higher (c_{Hb}* = 165 ± 22 mg/dl). The Hb oxygen saturation was found to be 0.65 ± 0.05 and 0.55 ± 0.05, respectively.

Figure 5 shows the reduced scattering coefficients $\mu_s'(\lambda)$ calculated from the data shown in Fig. 4, along with the corresponding Mie theory curves that provide a good match. As can be seen, the curve for normal colon mucosa falls more rapidly with wavelength than does that for the adenomatous polyp curve. This is due to the different effective scattering sizes, d_s = 1.5 μm for the polyp and d_s = 0.35 μm for normal mucosa. The values for the scatterer densities were found to be ρ_s = 1.5 × 10^9 mm^{-3} and ρ_s = 1.3 × 10^8 mm^{-3} for the normal mucosa and the adenomatous polyp, respectively. The predictions of Eq. (3) with the Mie theory curves of Fig. 5 as input are shown in Fig. 4. The model accurately describes the data, despite the dramatic differences in spectral shape between the diffuse reflectance spectra measured on the two tissue types. The deviation between the data and the model is typically less than 10% over most of the wavelength range.

Figure 6 shows the calculated values of the four parameters for all tissue sites studied: (a) total Hb concentration c_{Hb}*, (b) Hb oxygen saturation α, (c) effective scatterer density ρ_s, and (d) effective scatterer size d_s. Adenomatous polyps were clearly characterized by an increased Hb concentration, whereas there were no observable differences in the Hb oxygen saturation. The effective scatterer density was in general lower in adenomatous polyps and the effective scatterer size larger, even though there was significant overlap of the distributions of these parameters between the two tissue types. Table 2 summarizes the results shown in Fig. 6 by giving the average values and the standard deviations for each parameter.

Figure 7 shows a plot of the effective scatterer size d_s versus the Hb concentration c_{Hb}*. These two parameters are shown together to illustrate and empha-

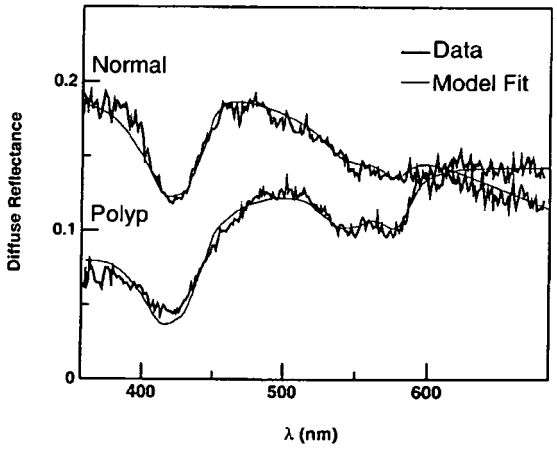

Fig. 4. Typical normal and adenomatous polyp spectra (thick curves) and modeled spectra (thin curves). Mie theory was used to approximate the reduced scattering coefficient for the model fits (Fig. 5).

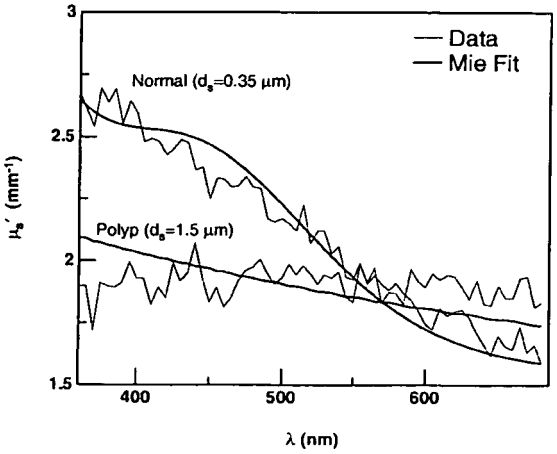

Fig. 5. Scattering spectra obtained from the data shown in Fig. 4 (thin curves) and the corresponding Mie theory spectra (thick curves). The effective scatterer sizes are indicated.

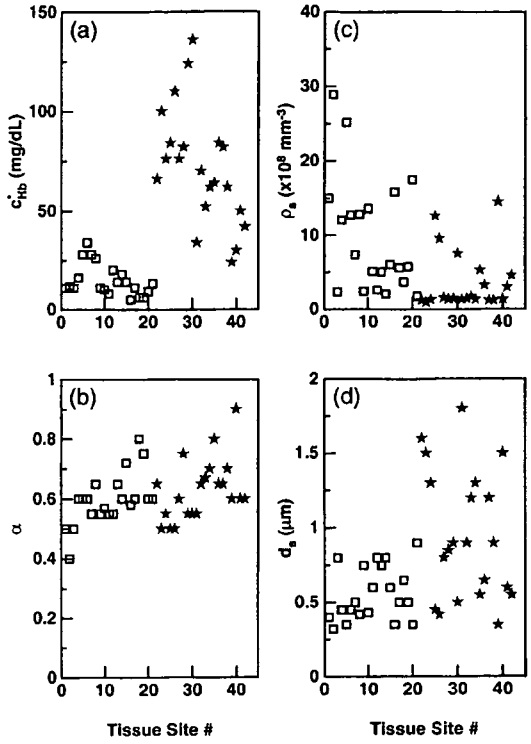

Fig. 6. Model parameters obtained from tissue data analysis: (a) total Hb concentration c_{Hb}*, (b) Hb oxygen saturation α, (c) effective scatterer density ρ_s, and (d) effective scatterer size d_s.

size the differences found in the scattering and the absorption properties of normal mucosa and adenomatous polyps in the colon. Note that the normal mucosa data tend to form a cluster, whereas the adenomatous polyp data are separated and characterized by a wider spread and irregular distribution in both the effective scatterer size and the Hb concentration.

6. Discussion

We have described a methodology that provides quantitative information about colon mucosal tissues *in vivo* on the basis of measurements of diffuse reflectance. The main components of this methodology are (a) data collection through an optical fiber probe with a fixed delivery and collection geometry,

Table 2. Average Values and Standard Deviations for the Model Parameters Obtained from Tissue Data Analysis

Model Parameter	Normal Mucosa	Adenomatous Polyp
Total Hb concentration c_{Hb}* (mg/dl)	13.6 ± 8.8	72.0 ± 29.2
Hb oxygen saturation α	0.59 ± 0.08	0.63 ± 0.10
Effective scatterer density ρ_s (×10^8 mm^{-3})	9.2 ± 7.5	3.5 ± 4.0
Effective scatterer size d_s (μm)	0.56 ± 0.18	0.94 ± 0.44

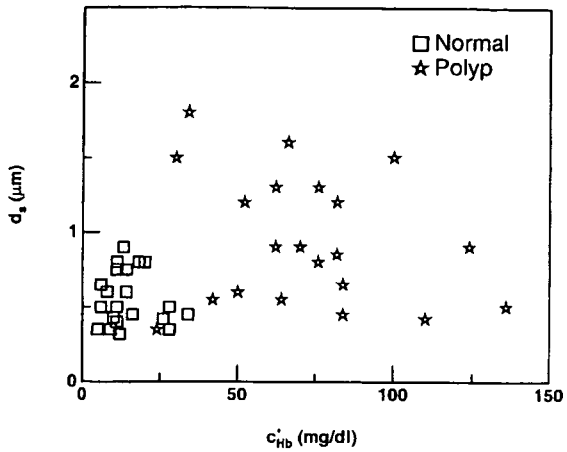

Fig. 7. Binary plot of total Hb concentration c_{Hb}* versus effective scatterer size d_s. Data from normal mucosa tend to form a well-defined cluster, whereas the adenomatous polyp data are marked by wider variation.

(b) an analytical model for data analysis that is based on light diffusion, and (c) a physical tissue model for validation and calibration of the analytical model.

Use of an optical probe with fixed geometry enables consistent data collection and the independent determination of the scattering and the absorption. Modeling of the probe geometry is facilitated through use of the parameter r_c', which also defines the probe's sensitivity to absorption. A probe with large r_c' renders the collected spectra more sensitive to tissue absorption as compared with a probe with a smaller r_c'. In Fig. 4 the secondary Hb absorption peaks are barely noticeable in the normal mucosa spectrum; a probe with larger r_c' would make these features more prominent.

It has been reported[35] that Eq. (1) is not quite correct because it omits the fluence term of the diffusion approximation. Therefore we investigated the fluence-corrected form of Eq. (1) and found that it does not differ from Eq. (1) by more than approximately 10% and that, for the range of optical parameters relevant to this study, addition of the fluence term does not improve the performance of our model in a significant way. We have therefore adopted for simplicity Eq. (1), as formulated by Farrell *et al.*,[22] as the starting point for our analysis.

In addition, it has been shown that the diffusion approximation is not valid for small source–detector separations and that the particular details of the scattering phase function affect the diffuse reflectance collected in a such a case.[36] The theoretical model applied in this study, based on Eq. (1) and an approximate integration over the probe light distribution, results in a simple analytic expression. We recognize that more rigorous solutions to the diffusion approximation exist and that a rigorous (numerical) interaction over the probe light distribution could, in principle, be performed. We considered these possibilities in the course of our study and de-

cided on our present model for two reasons: (a) within the range of parameters of interest, the more rigorous methods did not significantly improve the performance of the model, and (b) the simplicity of an analytical expression makes the model much more transparent and easy to implement. On the other hand, we did observe a discrepancy for relatively high values of the absorption coefficient, which led to the introduction of an empirical correction (Section 4) only in the case of highest absorption.

The analytical diffusion theory model is amenable to numerical inversion and successfully describes the tissue data after calibration on the physical tissue model composed of polystyrene beads and Hb. Other researchers have already used variants of the analytical model described here in the study of steady-state diffuse reflectance from tissues and physical tissue models in the IR range[31,32] and in the study of biological cell suspensions in the visible.[30] The present study is, to our knowledge, the first to apply the model in the visible range to *in vivo* data from human mucosal tissue measured with an optical fiber probe. By working in the visible rather than in the IR spectral range, we could restrict light penetration to the top one-half millimeter, i.e., in the mucosal layer where precancerous changes occur. Using the model, we have shown that it is possible to obtain quantitative information about the tissue studied, such as Hb concentration, Hb oxygen saturation, effective scatterer size, and effective scatterer density. The results show that diffuse reflectance provides a tool for quantitative analysis of mucosal tissue surfaces *in vivo*.

The fact that Hb is the only significant absorber in colon mucosa in the visible range of the spectrum is one of the key approximations made. Even though this assumption lacks direct confirmation, the fact that the data strongly exhibit the characteristic features of Hb absorption clearly indicates that Hb is a major absorber. In addition, we detected no evidence of other absorbers, and the spectra measured on the tissue physical model, with Hb as the only absorber, closely resemble the clinical tissue spectra. In a similar way, tissue scattering was modeled as being due to to homogeneous spherical scatterers with known refractive index. This approximation permits a quantitative characterization in terms of two basic parameters, the effective scatterer size and the effective scatterer density, which provide an estimate of the average scattering properties of the tissue.

Data analysis showed that adenomatous colon polyps were characterized by increased Hb concentration. It is known that tumors and cancerous tissues exhibit increased microvasculature, hence increased blood content.[37] It is also reported, by use of morphometry and vascular casting in combination with scanning electron microscopy techniques, that precancerous tissues such as adenomatous polyps of the colon are also characterized by increased microvascular volume.[3,38] Our results are in agreement with these reports in terms of observing the increased Hb concentration. Other reports associate increased microvascularity of the colon mucosa with Crohn's disease[39] and ulcerative colitis.[40] Even though we did not study these pathologic conditions, the technique employed would be suitable for the *in vivo* study of such diseases.

The Hb oxygen saturation was found to be approximately 60%, on average, for both normal mucosa and adenomatous polyps. This result is reasonable because the measurements were essentially performed in the capillary network of the mucosa where oxygen is transferred from Hb to tissue. Hb oxygen saturation drops within the capillaries from approximately 97% (arterial blood) to approximately 40% (venous blood)[41] with the measured values (approximately 60–70%) appropriately placed in the middle of this range. The fact that there were no differences observed between the two tissue types may be attributed to the fact that adenomatous polyp metabolism is not significantly altered so as to introduce changes in Hb oxygenation. On the other hand, tumors are often characterized by abnormally low Hb oxygenation,[42] which is probably related to the disturbed metabolism of such tissues. The technique presented here could be used *in vivo* for the study of tumors on the surface of hollow organs or for the study of other tissue types when knowledge of Hb saturation is needed.

Finally, we have observed an intrinsic differentiation in the scattering properties between the two tissue types studied. For adenomatous polyps, the average effective scattering size was larger and the average effective scatterer density was smaller as compared with normal mucosa. The range of effective scattering sizes was in good agreement with that reported for average scatterer sizes of biological cell suspensions.[34] The exact details of scattering origins in tissue are not well known. There are a number of hypotheses identifying contributions to scattering from various microstructures, both extracellular such as collagen fibers[43,44] and intracellular such as mitochondria[45] and cell nuclei.[18] One possible explanation for the scattering differences we observed could be that contributions to light scattering from intracellular structures are increased in adenomatous polyps because cells occupy a higher volume ratio. In addition, the submucosa, in which collagen is more densely packed,[46] is usually located too far away from the polyp surface to be able to affect the diffuse reflectance. This may explain the lower scatterer density in adenomatous polyps, provided that intracellular scatterers are larger than extracellular ones, on average. These hypotheses remain to be investigated by more detailed studies. Nevertheless, our observations could prove useful for the detection of precancerous conditions because these are usually characterized by cellular proliferation, hence increased volume occupied by cells in tissue.

In summary, we have demonstrated the potential of diffuse reflectance spectroscopy to obtain quantitative information about Hb content and information related to the tissue scatterers *in vivo* and in real time. We expect that further development of the

technique could increase the quantity, quality, and accuracy of the information obtained and render it a useful clinical tool.

We thank J. M. Crawford for helpful comments and L. Silveira, Jr., for assistance in collecting the clinical data. This research was supported by National Institutes of Health grants P41RR02594 and CA53717.

References

1. G. Zonios, R. Cothren, J. M. Crawford, M. Fitzmaurice, R. Manoharan, J. Van Dam, and M. S. Feld, "Spectral pathology," Ann. N. Y. Acad. Sci. **838,** 108–115 (1998).
2. T. J. Eide, "A morphometric analysis of dysplasia in small adenomas of the large intestine," Virchows Arch. A **410,** 119–124 (1986).
3. G. L. Tipoe and F. H. White, "Blood vessel morphometry in human colorectal lesions," Histol. Histopathol. **10,** 589–596 (1995).
4. S. S. Robey-Cafferty, A. K. el-Naggar, D. J. Grignon, K. R. Cleary, and J. Y. Ro, "Histologic parameters and DNA ploidy as predictors of survival in stage B adenocarcinoma of colon and rectum," Mod. Pathol. **3,** 261–266 (1990).
5. N. Sato, K. Takenobu, S. Motoaki, K. Sunao, A. Hiroshi, and B. Hagihara, "Measurement of hemoperfusion and oxygen sufficiency in gastric mucosa *in vivo*," Gastroenterology **76,** 814–819 (1979).
6. W. T. Knoefel, N. Kollias, D. W. Rattner, N. S. Nishioka, and A. L. Warshaw, "Reflectance spectroscopy of pancreatic microcirculation," J. Appl. Physiol. **80,** 116–123 (1996).
7. M. Ikeda and A. Matsushita, "Reflectance of rat brain structures mapped by an optical fiber technique," J. Neurosci. Methods **2,** 9–17 (1980).
8. R. Marchesini, M. Brambilla, C. Clemente, M. Maniezzo, A. E. Sichirollo, A. Testori, D. R. Venturoli, and N. Cascinelli, "*In vivo* spectrophotometric evaluation of neoplastic and non-neoplastic skin pigmented lesions. I. Reflectance measurements," Photochem. Photobiol. **53,** 77–84 (1991).
9. J. R. Mourant, I. J. Bigio, J. Boyer, R. L. Conn, T. Johnson, and T. Shimada, "Spectroscopic diagnosis of bladder cancer with elastic light scattering," Lasers Surg. Med. **17,** 350–357 (1995).
10. J. R. Mourant, I. J. Bigio, J. Boyer, T. M. Johnson, and J. Lacey, "Elastic scattering spectroscopy as a diagnostic for differentiating pathologies in the gastrointestinal tract: preliminary testing," J. Biomed. Opt. **1,** 192–199 (1996).
11. Z. Ge, K. T. Schomacker, and N. S. Nishioka, "Identification of colonic dysplasia and neoplasia by diffuse reflectance spectroscopy and pattern recognition techniques," Appl. Spectrosc. **52,** 833–839 (1998).
12. J. M. Schmitt, "Simple photon diffusion analysis of the effects of multiple scattering on pulse oximetry," IEEE Trans. Biomed. Eng. **38,** 1194–1203 (1991).
13. S. Takatani and J. Ling, "Optical oximetry sensors for whole blood and tissue," IEEE Eng. Med. Biol. Mag. **3,** 347–357 (1994).
14. M. R. Arnfield, J. Tulip, and M. S. McPhee, "Optical propagation in tissue with anisotropic scattering," IEEE Trans. Biomed. Eng. **35,** 372–381 (1988).
15. A. Kienle, L. Lilge, M. S. Patterson, R. Hibst, R. Steiner, and B. C. Wilson, "Spatially resolved absolute diffuse reflectance measurements for noninvasive determination of the optical scattering and absorption coefficients of biological tissue," Appl. Opt. **35,** 2304–2314 (1996).
16. S. Takatani and M. Graham, "Theoretical analysis of diffuse reflectance from a two-layer tissue model," IEEE Trans. Biomed. Eng. **26,** 656–664 (1979).
17. G. I. Zonios, R. M. Cothren, J. T. Arendt, J. Wu, J. Van Dam, J. M. Crawford, R. Manoharan, and M. S. Feld, "Morphological model of human colon tissue fluorescence," IEEE Trans. Biomed. Eng. **43,** 113–122 (1996).
18. L. T. Perelman, V. Backman, M. Wallace, G. Zonios, R. Manoharan, A. Nusrat, S. Shields, M. Seiler, C. Lima, T. Hamano, I. Itzkan, J. Van Dam, J. M. Crawford, and M. S. Feld, "Observation of periodic fine structure in reflectance from biological tissue: a new technique for measuring nuclear size distribution," Phys. Rev. Lett. **80,** 627–630 (1998).
19. R. A. Zangaro, L. Silveira, Jr., R. Manoharan, G. Zonios, I. Itzkan, R. R. Dasari, J. Van Dam, and M. S. Feld, "Rapid multiexcitation fluorescence spectroscopy system for *in vivo* tissue diagnosis," Appl. Opt. **35,** 5211–5219 (1996).
20. J. F. Brennan, G. I. Zonios, T. D. Wang, R. P. Rava, G. B. Hayes, R. R. Dasari, and M. S. Feld, "Portable laser spectrofluorimeter system for in vivo human tissue fluorescence studies," Appl. Spectrosc. **47,** 2081–2086 (1993).
21. R. M. Cothren, G. B. Hayes, J. R. Kramer, B. A. Sacks, C. Kittrell, and M. S. Feld, "A multifiber catheter with an optical shield for laser angiosurgery," Lasers Life Sci. **1,** 1–12 (1986).
22. T. J. Farrell, M. S. Patterson, and B. C. Wilson, "A diffusion theory model of spatially resolved, steady-state diffuse reflectance for the non-invasive determination of tissue optical properties," Med. Phys. **19,** 879–888 (1992).
23. F. A. Duck, *Physical Properties of Tissue: A Comprehensive Reference Book* (Academic, London, 1990), p. 62.
24. F. P. Bolin, L. E. Preuss, C. R. Taylor, and R. J. Ference, "Refractive index of some mammalian tissues using a fiber optic cladding method," Appl. Opt. **28,** 2297–2303 (1989).
25. A. Ishimaru, *Wave Propagation and Scattering in Random Media* (Academic, Orlando, Fla., 1978), Chap. 9.
26. O. W. van Assendelft, *Spectrophotometry of Haemoglobin Derivatives* (Thomas, Springfield, Ill., 1970), pp. 355–359.
27. W. H. Press, S. A. Teukolsky, W. T. Vetterling, and B. P. Flannery, *Numerical Recipes in C,* 2nd ed. (Cambridge U. Press, Cambridge, UK, 1992), pp. 681–699.
28. W. J. Wiscombe, "NCAR technical note," NCAR/TN-140+STR (National Center for Atmospheric Research, Boulder, Colo., 1979).
29. G. Zonios, "Diffuse reflectance spectroscopy of human colon tissue," Ph.D. dissertation (Department of Physics, Massachusetts Institute of Technology, Cambridge, Mass., 1998).
30. J. R. Mourant, J. P. Freyer, A. H. Hielscher, A. A. Eick, D. Shen, and T. M. Johnson, "Mechanisms of light scattering from biological cells relevant to noninvasive optical-tissue diagnostics," Appl. Opt. **37,** 3586–3593 (1998).
31. E. L. Hull and T. H. Foster, "Noninvasive near-infrared hemoglobin spectroscopy for *in vivo* monitoring of tumor oxygenation and response to oxygen modifiers," in *Optical Tomography and Spectroscopy of Tissue: Theory, Instrumentation, Model and Human Studies II,* B. Chance and R. R. Alfano, eds, SPIE Proc. **2979,** 355–364 (1997).
32. H. Liu, D. A. Boas, Y. Zhang, A. G. Yodh, and B. Chance, "Determination of optical properties and blood oxygenation in tissue using continuous NIR light," Phys. Med. Biol. **40,** 1983–1993 (1995).
33. E. Marx and G. W. Mulholland, "Size and refractive index determination of single polystyrene spheres," J. Res. Natl. Bur. Stand. **88,** 321–338 (1983).
34. R. Marchesini, E. Pignoli, S. Tomatis, S. Fumagalli, A. E. Sichirollo, S. Di Palma, M. Dal Fante, P. Spinelli, A. C. Croce, and G. Bottiroli, "*Ex vivo* optical properties of human colon tissue," Lasers Surg. Med. **15,** 351–357 (1994).
35. R. C. Haskell, L. O. Svaasand, T. Tsay, T. Feng, M. S. McAdams, and B. J. Tromberg, "Boundary conditions for the diffusion equation in radiative transfer," J. Opt. Soc. Am. A **11,** 2727–2741 (1994).

36. J. R. Mourant, J. Boyer, A. H. Hielscher, and I. J. Bigio, "Influence of the scattering phase function on light transport measurements in turbid media performed with small source-detector separations," Opt. Lett. **21,** 546–548 (1996).
37. R. K. Jain, "Determinants of tumor blood flow: a review," Cancer Res. **48,** 2641–2658 (1988).
38. S. A. Skinner, G. M. Frydman, and P. E. O'Brien, "Microvascular structure of benign and malignant tumors of the colon in humans," Digestive Diseases Sci. **40,** 373–384 (1995).
39. N. D. Carr, B. R. Pullan, and P. F. Schofield, "Microvascular studies in non-specific inflammatory bowel disease," Gut **27,** 542–549 (1986).
40. M. Tsujii, S. Kawano, S. Tsuji, I. Kobayashi, Y. Takei, K. Nagano, H. Fusamoto, T. Kamada, T. Ogihara, and N. Sato, "Colonic mucosal hemodynamics and tissue oxygenation in patients with ulcerative colitis: investigation by organ reflectance spectrophotometry," J. Gastroenterol. **30,** 183–188 (1995).
41. D. F. Horrobin, *Medical Physiology and Biochemistry* (Arnold, London, 1968), p. 384.
42. P. Vaupel, "Oxygen transport in tumors: characteristics and clinical implications," Adv. Exp. Med. Biol. **388,** 341–351 (1996).
43. A. G. Ferdman and I. V. Yannas, "Scattering of light from histologic sections: a new method for the analysis of connective tissue," J. Invest. Dermatol. **100,** 710–716 (1993).
44. I. S. Saidi, S. L. Jacques, and F. K. Tittel, "Mie and Rayleigh modeling of visible-light scattering in neonatal skin," Appl. Opt. **34,** 7410–7418 (1995).
45. B. Beauvoit, T. Kitai, and B. Chance, "Contribution of the mitochondrial compartments of the optical properties of the rat liver: a theoretical and practical approach," Biophys. J. **67,** 2501–2510 (1994).
46. H. J. Thomson, A. Busuttil, M. A. Eastwood, N. A. Smith, and R. A. Elton, "The submucosa of the human colon," J. Ultrastruct. Mol. Struct. Res. **96,** 22–30 (1986).

GASTROENTEROLOGY 2000;119:677–682

Endoscopic Detection of Dysplasia in Patients With Barrett's Esophagus Using Light-Scattering Spectroscopy

MICHAEL B. WALLACE,*,† LEV T. PERELMAN,† VADIM BACKMAN,† JAMES M. CRAWFORD,§ MARIANNE FITZMAURICE,‖ MAURICE SEILER,¶ KAMRAN BADIZADEGAN,# STEVEN J. SHIELDS,* IRVING ITZKAN,† RAMACHANDRA R. DASARI,† JACQUES VAN DAM,*,† and MICHAEL S. FELD†

*Division of Gastroenterology, Brigham and Women's Hospital, Harvard Medical School, Boston, Massachusetts; ¶Division of Gastroenterology, West Roxbury VA Medical Center, West Roxbury, Massachusetts; §Department of Pathology, Yale University School of Medicine, New Haven, Connecticut; ‖Department of Pathology, University Hospitals of Cleveland, Cleveland, Ohio; #Department of Pathology, Children's Hospital, Boston, Massachusetts; and †G. R. Harrison Spectroscopy Laboratory, Massachusetts Institute of Technology, Cambridge, Massachusetts

Background & Aims: **We conducted a study to assess the potential of light-scattering spectroscopy (LSS), which can measure epithelial nuclear enlargement and crowding, for in situ detection of dysplasia in patients with Barrett's esophagus.** *Methods:* **Consecutive patients with suspected Barrett's esophagus underwent endoscopy and systematic biopsy. Before biopsy, each site was sampled by LSS using a fiberoptic probe. Diffusely reflected white light was spectrally analyzed to obtain the size distribution of cell nuclei in the mucosal layer, from which the percentage of enlarged nuclei and the degree of crowding were determined. Dysplasia was assigned if more than 30% of the nuclei exceeded 10 μm and the histologic findings compared with those of 4 pathologists blinded to the light-scattering assessment. The data were then retrospectively analyzed to further explore the diagnostic potential of LSS.** *Results:* **Seventy-six sites from 13 patients were sampled. All abnormal sites and a random sample of nondysplastic sites were reviewed by the pathologists. The average diagnoses were 4 sites from 4 different patients as high-grade dysplasia (HGD), 8 sites from 5 different patients as low-grade dysplasia (LGD), 12 as indefinite for dysplasia, and 52 as nondysplastic Barrett's. The sensitivity and specificity of LSS for detecting dysplasia (either LGD or HGD) were 90% and 90%, respectively, with all HGD and 87% of LGD sites correctly classified. Decision algorithms using both nuclear enlargement and crowding further improved diagnostic accuracy, and accurately classified samples into the 4 histologic categories.** *Conclusions:* **LSS can reliably detect LGD and HGD in patients with Barrett's esophagus.**

The incidence of adenocarcinoma of the esophagus is increasing in the United States.[1] Almost 100% of cases occur in patients with Barrett's esophagus,[2] a condition in which metaplastic columnar epithelium replaces the normal squamous epithelium of the esophagus. Although periodic endoscopic surveillance of patients with Barrett's esophagus has been shown to detect carcinoma in its earlier stages,[3–5] surveillance has significant limitations. Dysplastic and early carcinomatous lesions arising in Barrett's esophagus are not visible macroscopically; therefore, surveillance requires extensive random biopsies of the esophagus and histologic examination of the excised tissue for dysplasia. Random biopsy is prone to sampling error and significantly increases the cost and risk of surveillance. Reliance on histology imposes a time delay between endoscopy and diagnosis, severely limiting the diagnostic accuracy of the endoscopic procedure. There also is significant interobserver disagreement between pathologists in diagnosing dysplasia.[6,7]

We are developing the use of reflected light to provide morphologic information about epithelial tissue without the need for tissue removal.[8,9] A previous publication[8] described the use of light-scattering spectroscopy (LSS) to determine the size distribution of epithelial cell nuclei in vitro and in vivo. We present the results of a prospective validation study of LSS to identify dysplasia at the time of endoscopy in a large cohort of patients with Barrett's esophagus, in which nuclear enlargement is used as a measure of dysplasia. In addition, we explore the use of decision algorithms that employ both nuclear enlargement and increased surface density, which is a measure of crowding, to further improve classification accuracy.

Abbreviations used in this paper: HGD, high-grade dysplasia; IND, indefinite for dysplasia; LGD, low-grade dysplasia; LIF, laser-induced fluorescence; LSS, light-scattering spectroscopy; NDB, nondysplastic Barrett's (esophagus); ROC, receiver operating characteristic.

0016-5085/00/$10.00
doi:10.1053/gast.2000.16511

Materials and Methods

The study was approved by the institutional review boards of the Brigham and Women's Hospital, West Roxbury VA Medical Center, and the Massachusetts Institute of Technology. After informed consent, consecutive patients undergoing surveillance endoscopy for a diagnosis of Barrett's esophagus or suspected carcinoma of the esophagus were evaluated by systematic biopsy. In surveillance patients, biopsy specimens were taken in 4 quadrants, every 2 cm of endoscopically visible Barrett's mucosa. In patients with suspected adenocarcinoma, biopsy specimens for this study were taken from the Barrett's mucosa adjacent to the tumor.

The methods used to collect and analyze reflectance signals from epithelial tissue have been described previously.[8] A schematic diagram of the system used to perform LSS is shown in Figure 1. Immediately before biopsy, the reflectance spectrum from that site was collected using an optical fiber probe. The probe was inserted into the accessory channel of the endoscope and brought into gentle contact with the mucosal surface of the esophagus. It delivered a weak pulse of white light to the tissue and collected the diffusely reflected light. The probe tip sampled tissue over a circular spot approximately 1 mm^2 in area. The pulse duration was 50 milliseconds, and the wavelength range was 350–650 nm. The optical probe caused a slight indentation at the tissue surface that remained for 30–60 seconds. Using this indentation as a target, the site was then carefully biopsied, and the sample was submitted for histologic examination. This insured that the site studied spectroscopically matched the site evaluated histologically.

The reflected light was spectrally analyzed, and the spectra were stored in a computer. The spectra consist of a large background from submucosal tissue, on which is superimposed a small (2%–3%) component that is oscillatory in wavelength because of scattering by cell nuclei in the mucosal layer. The amplitude of this component is related to the surface density of epithelial nuclei (number of nuclei per unit area). Because the area of tissue probed is fixed at 1 mm^2, this parameter is a measure of nuclear crowding. The number of oscillations over the wavelength range is related to nuclear size. The larger the nuclei, the larger the number of oscillations they produce.[8]

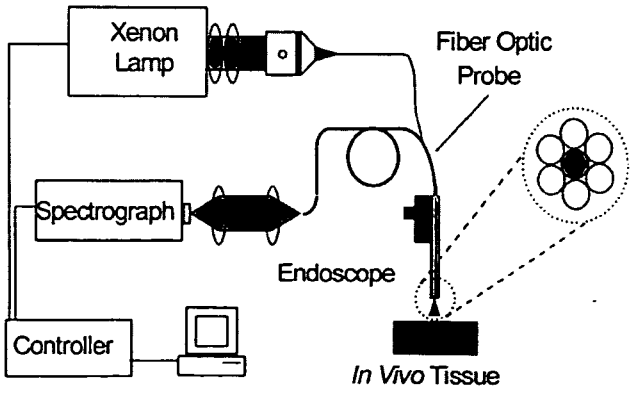

Figure 1. Schematic diagram of the LSS system.

Tissue is classified as dysplastic when an increased population of enlarged nuclei is detected.

The biopsy samples were evaluated by 4 gastrointestinal pathologists (J.M.C., M.F., M.S., and K.B.) from 4 different institutions. The histologic diagnosis of dysplasia in Barrett's epithelium was made using published criteria adapted to Barrett's epithelium,[10,11] using the following scoring system: 1, nondysplastic Barrett's (NDB); 2, indefinite for dysplasia (IND); 3, low-grade dysplasia (LGD); 4, high-grade dysplasia (HGD); and 5, invasive carcinoma. One pathologist examined all biopsy specimens, and then a subset of all abnormal specimens (indefinite or dysplasia) plus a random selection of normal specimens were examined by all 4 pathologists. The pathologists were blinded to the spectroscopic diagnosis and the diagnoses of the other pathologists. The spectroscopic diagnosis was compared with 2 pathologic diagnoses: the "average diagnosis" and the "consensus diagnosis." The average diagnosis followed the method of Riddell et al.[10] The mean score of all 4 pathologists was computed and then converted to discrete diagnoses by assigning the following values[10]: 1–1.74, NDB; 1.75–2.49, IND; 2.5–3.24, LGD; and >3.25, HGD. The consensus diagnosis was the diagnosis for which at least 3 pathologists reported the same result. When this method was used, samples for which fewer than 3 pathologists agreed were excluded.

Analysis of the spectra provided the distribution of nuclei as a function of size, from which nuclear enlargement and surface density could be extracted. For prospective evaluation, a single classification criterion was established based on unblinded analysis of an initial "modeling set" of 8 samples and consultation with the study pathologists. A site was classified as dysplasia if more than 30% of the nuclei were enlarged, with "enlarged" defined as exceeding a 10-μm threshold diameter, and classified as nondysplasia otherwise. Using this criterion, all subsequent samples were prospectively analyzed, employing both the consensus and average pathology diagnoses as comparison standards, with dysplasia defined as LGD or HGD and nondysplasia defined as NDB or IND.

After all samples were prospectively analyzed, the diagnostic potential of LSS was further evaluated for the entire data set, using the average diagnoses as the standard. First, the optimal definition of "enlarged" was established by varying the threshold diameter on the stored data from 8 to 14 μm in 2-μm steps, using the criterion that at least 30% of the nuclei be enlarged for dysplasia (either LGD or HGD). The resulting values of sensitivity and specificity for each diameter were then used to construct a receiver operating characteristic (ROC) curve.[12] The threshold diameter associated with the point closest to the left upper corner of the ROC plot (corresponding to a sensitivity and specificity of 100%) was taken to be the optimum value and used in subsequent analysis.

LSS was also used to classify samples by histologic grade (NDB, IND, LGD, or HGD) and thus assess interobserver agreement. For this, logistic regression was used.[13] At each site, the multivariate model was used to assign probabilities for each of the 4 histologic grades as a function of the 2 param-

eters. The site was classified as the histologic grade that had the highest probability.

The interobserver variability between each pathologist and the average diagnosis of the other 3 pathologists, and between LSS and the mean pathology score (of all 4 pathologists), were then calculated using the kappa (κ) statistic. Both the average and consensus diagnoses were used as comparison standards. Descriptive terms (poor, moderate, excellent) were assigned to numerical values of κ values according to the scheme proposed by Landis and Koch.[14] Although 3 samples were diagnosed as invasive carcinoma by 1 pathologist, none of the samples were considered invasive carcinoma by either the average or consensus diagnoses. Because the original classification scheme, based on a mean pathology score by Riddell et al.,[10] did not include a classification for invasive carcinoma, these samples were considered to be diagnosed by the single pathologist as HGD for the purpose of the κ calculation. For the consensus diagnosis, only samples for which a consensus was reached were considered.

All statistical analyses were performed using SAS software V6.12 (SAS Institute, Cary, NC) and STATA software V5.0 (Stata Corp., College Station, TX). The percentages of enlarged nuclei among the 4 categories from NDB to HGD were compared using the Mantel–Haenszel test for trend.[15]

Results

Endoscopy with LSS was performed in 49 patients, 43 for surveillance of Barrett's esophagus and 6 for suspected adenocarcinoma of the esophagus. The clinical characteristics of the patients are listed in Table 1. Based on a single pathologist's evaluation, all abnormal sites (indefinite or dysplasia) plus a random selection of nondysplastic sites were evaluated by all 4 pathologists. The resulting study set consisted of 76 biopsy sites from 13 patients. Four sites from 4 separate patients were classified by the pathologists as HGD. Eight sites from 5 separate patients were classified as LGD. All randomly selected samples diagnosed as nondysplastic by the first pathologist were also diagnosed as nondysplastic by the average and consensus methods of all 4 study pathologists. The pathologic diagnoses, as determined by the average and consensus methods, are listed in Table 2.

Table 1. Clinical Characteristics of Patients With Barrett's Esophagus in the Study Set

Total no. of patients	13
Mean age, *yr* (range)	69 (48–81)
Sex (M/F)	12/1[a]
Mean length of Barrett's, *cm* (range)	7 (2–15)
Asymptomatic surveillance	8
Evaluation of suspected carcinoma	6

[a]The predominance of men reflects the underlying population of the Veterans Administration Hospital and the demographic distribution of Barrett's esophagus.

Table 2. Summary of Histologic Diagnoses of the Study Set

Histologic diagnosis	Average method	Consensus method[a]
NDB	52 (68)	52 (85)
IND	12 (16)	2 (3)
LGD	8 (11)	6 (10)
HGD	4 (5)	1 (2)

NOTE. Results are number of samples with percentage in parenthesis.
[a]No consensus among 3 pathologists for 15 samples.

Figure 2 plots the surface density and percentage of enlarged nuclei, as measured by LSS for each of the 76 samples in the study set, using 10 μm as the threshold diameter for "enlarged." The average histologic diagnosis for each sample is also indicated. Nondysplastic samples tend to cluster at low values of nuclear enlargement and surface density, whereas the samples diagnosed as HGD exhibit the largest values of both (Figure 2). Both LSS parameters were correlated with the histologic grade of dysplasia (R^2 = 0.82 for percentage of enlarged nuclei; R^2 =0.59 for nuclear surface density). The mean values of enlarged nuclei measured for NDB, IND, LGD, and HGD were 6%, 28%, 41%, and 53%, respectively ($P <$ 0.001 for trend).

The initial 8 samples were used as a modeling set to determine the optimal threshold for classifying samples as dysplasia. The ensuing 68 samples were then used as a validation set, employing the criterion for dysplasia that at least 30% of the nuclei be larger than 10 μm (dashed line in Figure 2). The sensitivity and specificity of the resulting LSS diagnoses were 90% and 90%, respectively, with the average histologic diagnoses used as the standard, and 83% and 96%, respectively, with the consensus diagnoses used.

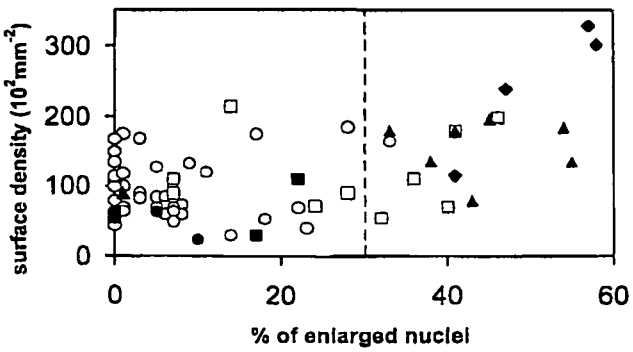

Figure 2. Percentage of enlarged (≥10 μm) nuclei and nuclear surface density (number of nuclei per 100 μm^2), as determined by LSS, for each of the 76 biopsy sites of the study set. The average histologic diagnoses are indicated: NDB (*circles*), IND (*squares*), LGD (*triangles*), and HGD (*diamonds*). *Filled symbols* denote samples diagnosed as dysplasia. *Shaded symbols* denote the 8 samples of the modeling set. *Dashed line* indicates the dysplasia/nondysplasia threshold used in the prospective evaluation.

Table 3. Interobserver Agreement Between Individual Pathologists and the Average Diagnosis of the 3 Other Pathologists and Agreement Between the Multivariate LSS Model and the Average Diagnosis of All 4 Pathologists

	κ	% Agreement
Pathologist 1 vs. colleagues	0.31	66
Pathologist 2 vs. colleagues	0.22	62
Pathologist 3 vs. colleagues	0.34	65
Pathologist 4 vs. colleagues	0.37	65
Spectroscopy vs. pathology, average diagnoses	0.57	80
Spectroscopy vs. pathology, consensus diagnoses	0.63	90

LSS also reliably categorized tissue sites into the 4 histologic categories (NDB, IND, LGD, and HGD). Interobserver agreement between LSS and the average and consensus pathologic diagnoses, and between the individual pathologists and the average diagnosis of their 3 colleagues, is shown in Table 3. The κ score showed poor agreement between individual pathologists and the average of their colleagues, and moderate agreement between LSS and the average and consensus diagnosis of the 4 pathologists.

Discussion

Our study demonstrates a new, minimally invasive method that can accurately and reliably classify dysplasia in patients with Barrett's esophagus. The diagnosis is based on LSS to measure nuclear crowding and enlargement, which are 2 criteria used by pathologists to diagnose mucosal dysplasia.[10,11] The method is sensitive and specific for detecting both LGD and HGD, and we are developing algorithms that will allow the diagnosis to be rendered in real time.

This method has significant advantages over current biopsy-dependent techniques. It is minimally invasive, requiring endoscopy but not tissue biopsy to make a diagnosis. It can provide an immediate diagnosis. Thus, multiple sites in the esophagus can be examined rapidly without tissue removal. Because of the high sensitivity and specificity, LSS can be used to survey a much larger number of sites in the esophagus than is feasible with random biopsy. This may reduce the sampling error and cost of random biopsy surveillance, increasing the yield. Complete elimination of sampling error will only occur with methods that can examine the entire mucosal surface at risk. Spectroscopic methods using fiberoptic probes are not capable of efficiently sampling the entire mucosal surface but are an important, if not essential, first step toward developing large-field imaging devices. The method uses white light, delivered through small optical fibers, and is compatible with endoscopic techniques. This study has shown the method to be reliable, in the sense that it can provide information that is in good agreement with the findings of pathology, as measured by the average or consensus diagnoses. We believe that this is because LSS provides an objective, quantifiable measure of dysplasia.

Quantitative measures of mucosal nuclei and DNA have been shown to correlate well with dysplasia and the natural history of dysplasia and esophageal cancer. The presence of increased nuclear DNA or "aneuploidy" in excised Barrett's tissue has been shown in some studies to be associated with the presence of dysplasia[16–18] and progression to carcinoma,[19,20] although other studies did not find a significant association.[21–23] Unlike in vivo LSS, ploidy analysis requires tissue excision and, like all random biopsy techniques, is prone to sampling error.

Other optical methods of detecting dysplasia in Barrett's esophagus have been described. Laser-induced fluorescence (LIF) spectroscopy at endoscopy is believed to measure the abnormal concentrations of certain endogenous fluorophores such as porphyrins in dysplastic and malignant tissue. Panjehpour et al.[24,25] and others[26,27] found LIF to be sensitive for the detection of diffuse HGD and adenocarcinoma, but insensitive for focal HGD and LGD.

Vital dyes have been used to identify dysplasia in the uterine cervix and Barrett's esophagus. Canto et al.[28] showed that methylene blue may enhance the detection of Barrett's epithelium and dysplasia at endoscopy. Lastly, Falk et al.[29] showed that a nonendoscopic method using an abrasive balloon to collect cytologic specimens had a sensitivity of 80% for detecting HGD or carcinoma, but only 25% for LGD. Thus, the methods currently available have significant limitations of sampling error, insensitivity for low-grade and focal high-grade dysplasia, poor interobserver agreement in the diagnosis, and delay in rendering a diagnosis.

To minimize the potential for artifacts caused by active esophagitis, all patients with a history of reflux symptoms or esophagitis were aggressively treated with antiacid therapy before endoscopy. This problem was also minimized by the fact that LSS samples the tissue to a depth of only 100–200 μm. Thus, isolated enlarged nuclei located in the base of the crypts, as is typically seen in esophagitis, were undersampled.

The variability in the diagnosis of dysplasia is both a clinical problem and a limitation of studies using pathologic diagnosis as a gold standard, including the present one. We attempted to minimize this by using the eval-

uations of 4 pathologists from 4 separate institutions, and basing the diagnosis on an average as well as a consensus of their independent diagnoses. The interobserver agreement among the 4 pathologists was similar to that of other expert gastrointestinal pathologists.[6] The optical probe we used to measure reflectance spectra via an endoscope samples approximately 1 mm^2 of tissue at each site. Thus, the overall amount of tissue sampled spectroscopically, even with multiple measurements, was small, and it is possible that other regions of dysplasia were missed by sampling error. The probe area is also smaller than the surface of the tissue that was biopsied. Thus, it is possible that sampling error between the probe and the biopsy occurred. The likelihood of this error is low because the dysplasia seen in all but one specimen was seen throughout the biopsied area. The one specimen with only focal dysplasia within the biopsied tissue was the one that was "mis"classified by spectroscopy as "nondysplastic" but by histology as LGD. We believe sampling error may have caused this misclassification. Larger probes can also be developed, and imaging systems capable of surveying large fields of mucosa, similar in concept to those developed for LIF spectroscopy,[30,31] are also possible.

In addition to its use in diagnosing dysplasia in Barrett's esophagus, LSS has potential applications to the diagnosis of mucosal dysplasia in multiple other tissues, including ulcerative colitis, hereditary colon carcinoma, and mucosal dysplasia syndromes in organs outside the gastrointestinal tract such as lung, cervix, and oropharynx. Because of its high sensitivity and specificity, LSS could be used to guide biopsy to regions of dysplasia, which may increase the yield and decrease sampling error of random biopsy. The technique could also be used to direct endoscopic therapies such as tissue ablation with laser light, cryotherapy, or photodynamic therapy. Studies evaluating LSS in other forms of mucosal dysplasia, and the ability of LSS to predict the progression to HGD and cancer, are underway.

References

1. Blot W, Devesa SS, Kneller R, Fraumeni J. Rising incidence of adenocarcinoma of the esophagus and gastric cardia. JAMA 1991;265:1287–1289.
2. Antonioli D. The esophagus. In: Henson D, Alobores-Saavdera J, eds. The pathology of incipient neoplasia. Philadelphia: Saunders, 1993:64–83.
3. Streitz JM Jr, Andrews CW Jr, Ellis FH Jr. Endoscopic surveillance of Barrett's esophagus. Does it help? J Thorac Cardiovasc Surg 1993;105:383–387.
4. Peters JH, Clark GW, Ireland AP, Chandrasoma P, Smyrk TC, DeMeester TR. Outcome of adenocarcinoma arising in Barrett's esophagus in endoscopically surveyed and nonsurveyed patients. J Thorac Cardiovasc Surg 1994;108:813–821.
5. Lerut T, Coosemans W, Van Raemdonck D, Dillemans B, De Leyn P, Marnette JM, Geboes K. Surgical treatment of Barrett's carcinoma. Correlations between morphologic findings and prognosis. J Thorac Cardiovasc Surg 1994;107:1059–1065.
6. Reid BJ, Haggitt RC, Rubin CE, Roth G, Surawicz CM, Van Belle G, Lewin K, Weinstein WM, Antonioli DA, Goldman H, MacDonald W, Owen D. Observer variation in the diagnosis of dysplasia in Barrett's esophagus. Hum Pathol 1988; 19:166–178.
7. Petras RE, Sivak MV, Rice TW. Barrett's esophagus. A review of the pathologists role in diagnosis and management. Pathol Annu 1991;26:1–32.
8. Perelman LT, Backman V, Wallace M, Zonios G, Manoharan R, Nusrat A, Shields S, Seiler M, Lima C, Hamano T, Itzkan I, VanDam J, Crawford JM, Feld M. Observation of periodic fine structure in reflectance from biological tissue: a new technique for measuring nuclear size distribution. Phys Rev Lett 1998;80: 627–630.
9. Zonios G, Perelman LT, Backman V, Manoharan R, Fitzmaurice M, Van Dam J, Feld MS. Diffuse reflectance spectroscopy of human adenomatous colon polyps. Appl Optics 1998 (in press).
10. Riddell R, Goldman H, Ransohoff D, Appelman HD, Fenoglio CM, Haggitt RC, Ahren C, Correa P, Hamilton SR, Morson BC, Sommers SC, Yardley JH. Dysplasia in inflammatory bowel disease: standardization classification with provisional clinical implications. Hum Pathol 1983;14:931–968.
11. Haggitt RC. Barrett's esophagus, dysplasia, and adenocarcinoma. Hum Pathol 1994;25:982–993.
12. Rosner B. Fundamentals of biostatistics. Boston: Duxbury, 1995:521–539.
13. Kleinbaum DG, Kupper LL, Muller KE, Nizam A. Applied regression analysis and other multivariable methods. 3rd ed. Pacific Grove, CA: Duxbury, 1998.
14. Landis J, Koch G. The measurement of observer agreement for categorical data. Biometrics 1977;33:159–174.
15. Mantel N, Haenzel W. Statistical aspects of the analysis of data from retrospective studies of disease. J Natl Cancer Inst 1959; 22:719–748.
16. Haggitt RC, Reid BJ, Rabinovitch PS, Rubin CE. Barrett's esophagus. Correlation between mucin histochemistry, flow cytometry, and histologic diagnosis for predicting increased cancer risk. Am J Pathol 1988;131:53–61.
17. Reid BJ, Haggitt RC, Rubin CE, Rabinovitch PS. Barrett's esophagus. Correlation between flow cytometry and histology in detection of patients at risk for adenocarcinoma. Gastroenterology 1987;93:1–11.
18. Montgomery EA, Hartmann DP, Carr NJ, Holterman DA, Sobin LH, Azumi N. Barrett's esophagus with dysplasia. Flow cytometric DNA analysis of routine, paraffin-embedded mucosal biopsies. Am J Clin Pathol 1996;106:298–304.
19. James PD, Atkinson M. Value of DNA image cytometry in the prediction of malignant change in Barrett's oesophagus. Gut 1989;30:899–905.
20. Reid BJ, Blount PL, Rubin CE, Levine DS, Haggitt RC, Rabinovitch PS. Flow-cytometric and histological progression to malignancy in Barrett's esophagus: prospective endoscopic surveillance of a cohort. Gastroenterology 1992;102:1212–1219.
21. Fennerty MB, Sampliner RE, Way D, Riddell R, Steinbronn K, Garewal HS. Discordance between flow cytometric abnormalities and dysplasia in Barrett's esophagus. Gastroenterology 1989; 97:815–820.
22. Sciallero S, Giaretti W, Bonelli L, Geido E, Rapallo A, Conio M, Ravelli P, Lombardo L, Briglia R, Lapertosa G, Aste H. DNA content analysis of Barrett's esophagus by flow cytometry. Endoscopy 1993;25:648–651.
23. Menke-Pluymers MB, Mulder AH, Hop WC, van Blankenstein M, Tilanus HW. Dysplasia and aneuploidy as markers of malignant degeneration in Barrett's oesophagus. The Rotterdam Oesophageal Tumour Study Group. Gut 1994;35:1348–1351.

24. Panjehpour M, Overholt BF, Vo-Dinh T, Haggitt RC, Edwards DH, Buckley FP III. Endoscopic fluorescence detection of high-grade dysplasia in Barrett's esophagus. Gastroenterology 1996;111: 93–101.
25. Panjehpour M, Overholt BF, Schmidhammer JL, Farris C, Buckley PF, Vo-Dinh T. Spectroscopic diagnosis of esophageal cancer: new classification model, improved measurement system. Gastrointest Endosc 1995;41:577–581.
26. Vo-Dinh T, Panjehpour M, Overholt BF. Laser-induced fluorescence for esophageal cancer and dysplasia diagnosis. Ann N Y Acad Sci 1998;838:116–122.
27. von Holstein CS, Nilsson AM, Andersson-Engels S, Willen R, Walther B, Svanberg K. Detection of adenocarcinoma in Barrett's oesophagus by means of laser induced fluorescence. Gut 1996; 39:711–716.
28. Canto MI, Setrakian S, Petras RE, Blades E, Chak A, Sivak MV Jr. Methylene blue selectively stains intestinal metaplasia in Barrett's esophagus. Gastrointest Endosc 1996;44:1–7.
29. Falk GW, Chittajallu R, Goldblum JR, Biscotti CV, Geisinger KR, Petras RE, Birgisson S, Rice TW, Richter JE. Surveillance of patients with Barrett's esophagus for dysplasia and cancer with balloon cytology. Gastroenterology 1997;112:1787–1797.
30. Wang TD, Van Dam J, Crawford JM, Preisinger EA, Wang Y, Feld MS. Fluorescence endoscopic imaging of human colonic adenomas. Gastroenterology 1996;111:1182–1191.
31. Wang T, Wang Y, Crawford J, Itzkan I, Feld M, Van Dam J. Fluorescence endoscopic imaging for the detection of colonic dysplasia. Gastrointest Endosc 1999;49:447–455.

Received January 7, 1999. Accepted April 26, 2000.

Address requests for reprints to: Jacques Van Dam, M.D., Ph.D., Stanford University Medical Center, 300 Pasteur Drive, Room H1121, Stanford, California 94305-5202.

Supported by National Institutes of Health grants P41RR02594 and CA53717; a grant from the American College of Gastroenterology (to M.B.W.); and in part by a generous grant from Albert Reidy and the Wilmington Arena Authority (to J.V.D.).

The authors thank Dr. Asthma Nusrat for her insightful contributions to this study.

CLAIMS

1. A system for obtaining characteristics of tissue of an organ, the system comprising:

a probe configured to scan the tissue of the organ, the probe comprising:

an illumination optics system configured to illuminate at least one portion of the tissue of the organ with collimated light, and

a receiving system configured to receive light backscattered by at least one portion as a result of the illumination;

at least one spectrometer configured to generate at least one spectrum from the received light;

an imaging unit configured to obtain at least one image of the at least one portion;

an analysis unit configured to analyze the at least one spectrum to provide at least one characteristic of the at least one portion; and

a user interface configured to present to a user information comprising the at least one image in association with at least one visual representation of the at least one characteristic, wherein the information is used to determine whether to take a tissue sample from the at least one portion.

2. The system of claim 1, wherein the analysis unit is further configured to determine a correspondence between the at least one image and the at least one characteristic.

3. The system of claim 1, wherein the collimated light comprises polarized collimated light.

4. The system of claim 1, further comprising a probe control unit for controlling operation of the probe.

5. The system of claim 1, wherein the information comprises the at least one image superimposed with the at least one visual representation of the at least one characteristic.

6. The system of claim 1, wherein the information is presented as at least one of a color map and a pseudocolor map.

7. The system of claim 1, wherein the at least one image comprises at least one two-dimensional image.

8. The system of claim 1, wherein the at least one characteristic is used to detect at least one abnormal morphological change in the at least one portion.

9. The system of claim 5, wherein the at least one abnormal morphological change comprises a degree of dysplasia at the at least one portion.

10. The system of claim 1, wherein the receiving system is configured to receive a portion of the received light with a predetermined angular distribution.

11. The system of claim 1, wherein the probe is positioned at a distance within a range of distances from the at least one portion.

12. The system of claim 11 wherein the at least one characteristic is independent of the distance.

13. The system of claim 1, wherein the imaging unit is configured to obtain the at least one image of the at least one portion substantially simultaneously with a time when the probe scans the least one portion.

14. The system of claim 1, wherein the at least one characteristic comprises at least one of nuclear density, nuclear size distribution and chromatin density at the at least one portion.

15. The system of claim 1, wherein the at least one characteristic comprises at least one morphological properly of tissue of the at least one portion.

16. The system of claim 1, wherein the at least one characteristic comprises at least one properly of tissue beneath an epithelial layer at the at least one portion.

17. The system of claim 1, wherein the at least one characteristic comprises at least one density of collagen matrix, concentration of hemoglobin and oxygen saturation of hemoglobin at the at least one portion.

18. The system of claim 1, wherein the illumination optics system is moveable with respect to a main axis of the probe.

19. The system of claim 1, wherein the illumination optics system is configured to at least one rotate, tilt, pivot and translate with respect to a main axis of the probe.

20. The system of claim 1, wherein the organ comprises an organ from at least one of gastrointestinal tract, reproductive tract and respiratory tract.

21. The system of claim 1, wherein the organ comprises at least one of an esophagus, colon, pancreas, biliary duct, cervix, stomach, small intestine, large intestine and rectum.

22. A method of spectral analysis of light reflected from tissue of at least one organ, the method comprising:

obtaining at least one image collected from the at least one site of the tissue of the at least one organ;

processing reflected light to obtain at least one spectrum, wherein the reflected light is backscattered from the at least one site when the at least one site is illuminated with collimated light;

analyzing the at least one spectrum to obtain at least one characteristic of the at least one site;

determining at least one indicator of at least one abnormal change at the at least one site based on the at least one characteristic; and

displaying to a user the at least one image in association and the at least one indicator to enable the user to determine whether to take a sample of tissue from the at least one site.

23. The method of claim 16, wherein the least one image comprises at least one video image.

24. The method of claim 22, wherein the displaying comprises displaying to the user the at least one video image superimposed with the at least one indicator.

25. The method of claim 22, wherein analyzing the at least one spectrum comprises extracting at least one parallel polarization spectrum and at least one perpendicular polarization spectrum from the at least one spectrum.

26. The method of claim 25, further comprising subtracting the at least one parallel polarization spectrum from the at least one parallel perpendicular spectrum to obtain the at least one characteristic that comprises at least one of nuclear density, nuclear size distribution and chromatin density at the at least one site.

27. The method of claim 25, further comprising combining the at least one perpendicular polarization spectrum and the at least one parallel polarization spectrum to obtain the at least one characteristic that comprises at least one of density of collagen matrix, concentration of hemoglobin and oxygen saturation of hemoglobin at the at least one site.

28. The method of claim 22, wherein the collimated light comprises polarized collimated light.

29. The method of claim 22, wherein analyzing the at least one spectrum comprises obtaining a total diffuse reflectance spectrum to obtain at least one characteristic of at least one layer beneath a surface layer at the at least one site.

30. The method of claim 22, wherein the at least one characteristic of the at least one layer comprises at least one reduced scattering coefficient.

31. The method of claim 30, further comprising determining a degree of dysplasia at the at least one site based on the at least one reduced scattering coefficient, wherein a value of the at least one reduced scattering coefficient inversely correlates with the degree of dysplasia.

32. The method of claim 22, wherein the organ comprises an organ from at least one of gastrointestinal tract, reproductive tract and respiratory tract.

33. A device for obtaining characteristics of tissue, the device comprising:

a probe coupled to an endoscopic unit and configured to scan the tissue, wherein the probe is moveable with respect to a main axis of the endoscopic unit, the probe comprising:

an illumination optics unit configured to illuminate at least one portion of the tissue with polarized collimated light, and

a receiving unit configured to receive light backscattered by at least one portion as a result of the illumination;

at least one spectrometer configured to generate at least one spectrum from the received light;

an imaging unit configured to obtain at least one image of the at least one portion;

an analysis unit configured to analyze the at least one spectrum to provide at least one characteristic of the at least one portion; and

a user interface configured to present to a user information comprising the at least one image in association with at least one visual representation of the at least one characteristic, wherein the information is used to determine whether to take a tissue sample from the at least one portion.

34. The device of claim 33, further comprising a probe control unit for controlling operation of the probe.

35. The device of claim 33, wherein the tissue comprises tissue of an organ from at least one of gastrointestinal tract, reproductive tract and respiratory tract.

36. A system for obtaining characteristics of tissue, the device comprising:

a device coupled to an endoscopic unit and configured to scan the tissue, wherein the device is moveable with respect to the endoscopic unit, the device comprising:

an illumination optics unit configured to illuminate at least one portion of the tissue with polarized collimated light, and

a receiving unit configured to receive light backscattered by at least one portion as a result of the illumination;

at least one spectrometer configured to generate at least one spectrum from the received light;

an imaging unit configured to obtain at least one image of the at least one portion;

an analysis unit configured to analyze the at least one spectrum to provide at least one characteristic of the at least one portion; and

a user interface configured to present to a user information comprising the at least one image in association with at least one visual representation of the at least one characteristic, wherein the information is used to determine whether to take a tissue sample from the at least one portion.

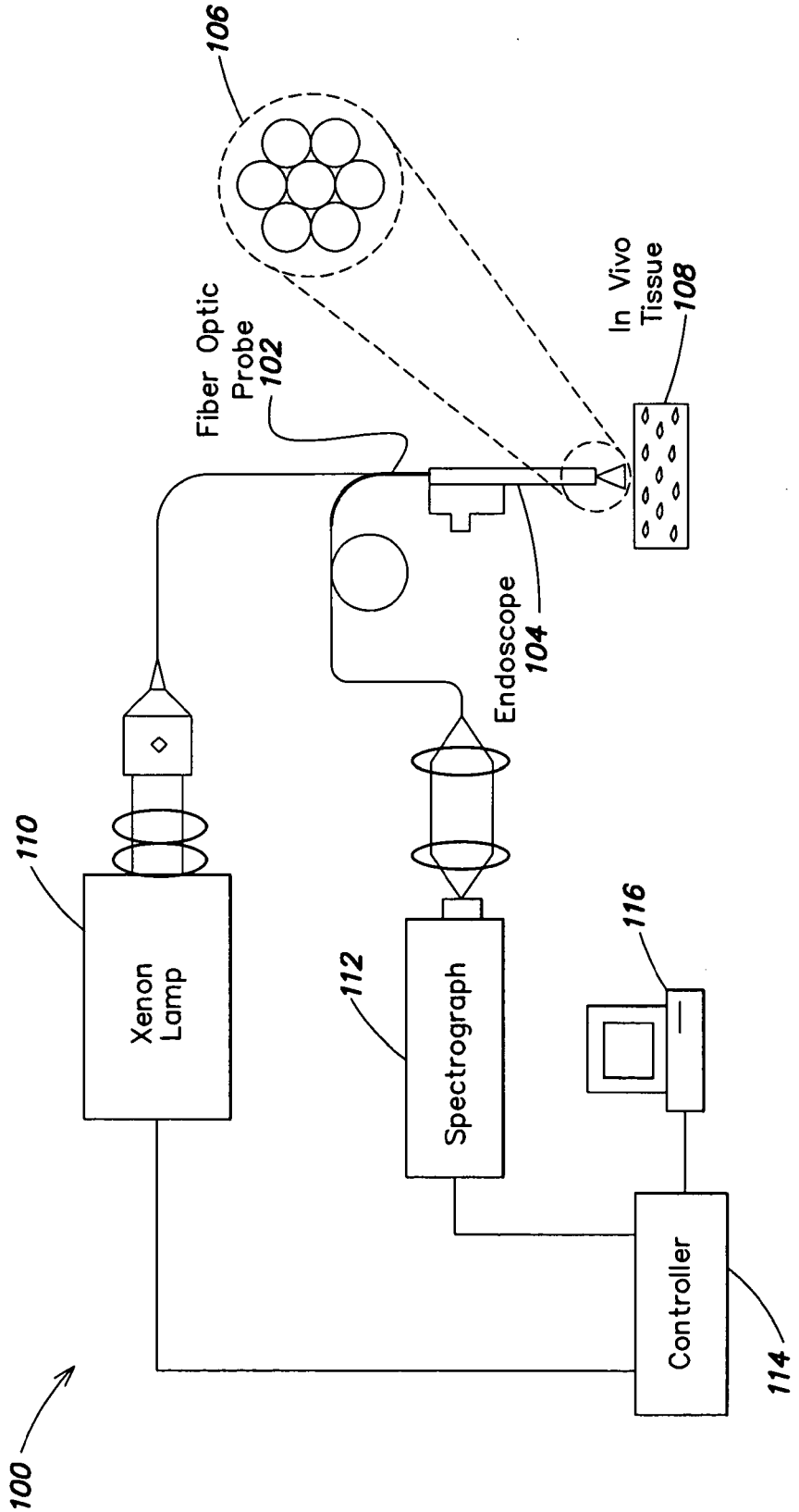
106
Fiber Optic Probe 102
In Vivo Tissue 108
Endoscope 104
110
Xenon Lamp
112
Spectrograph
116
Controller
114
100

FIG. 1

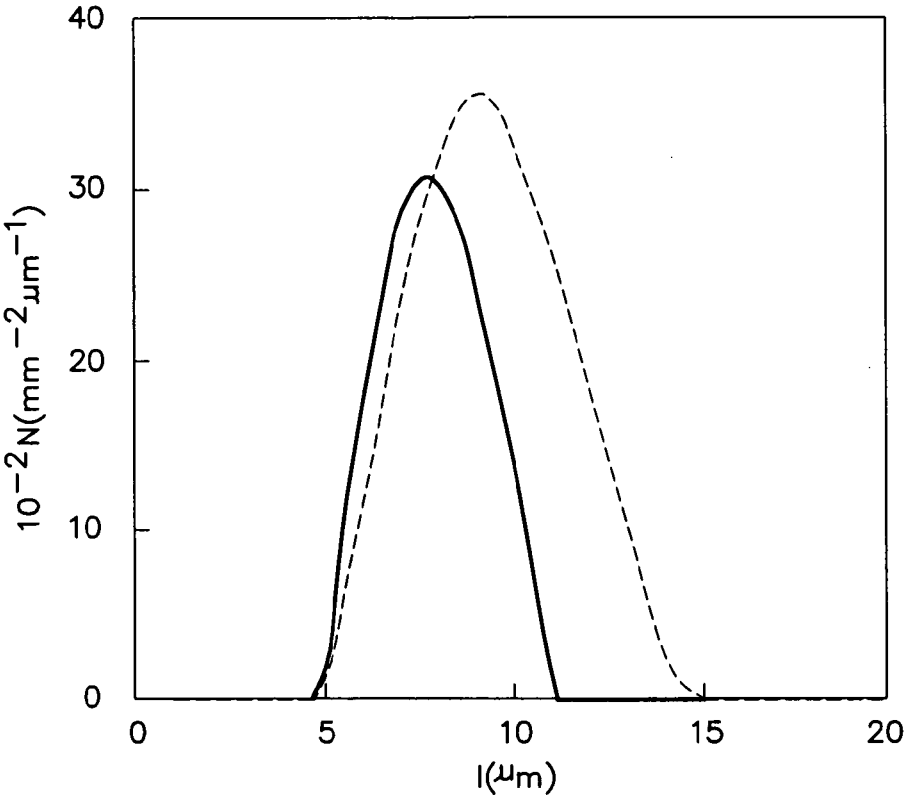

FIG. 2

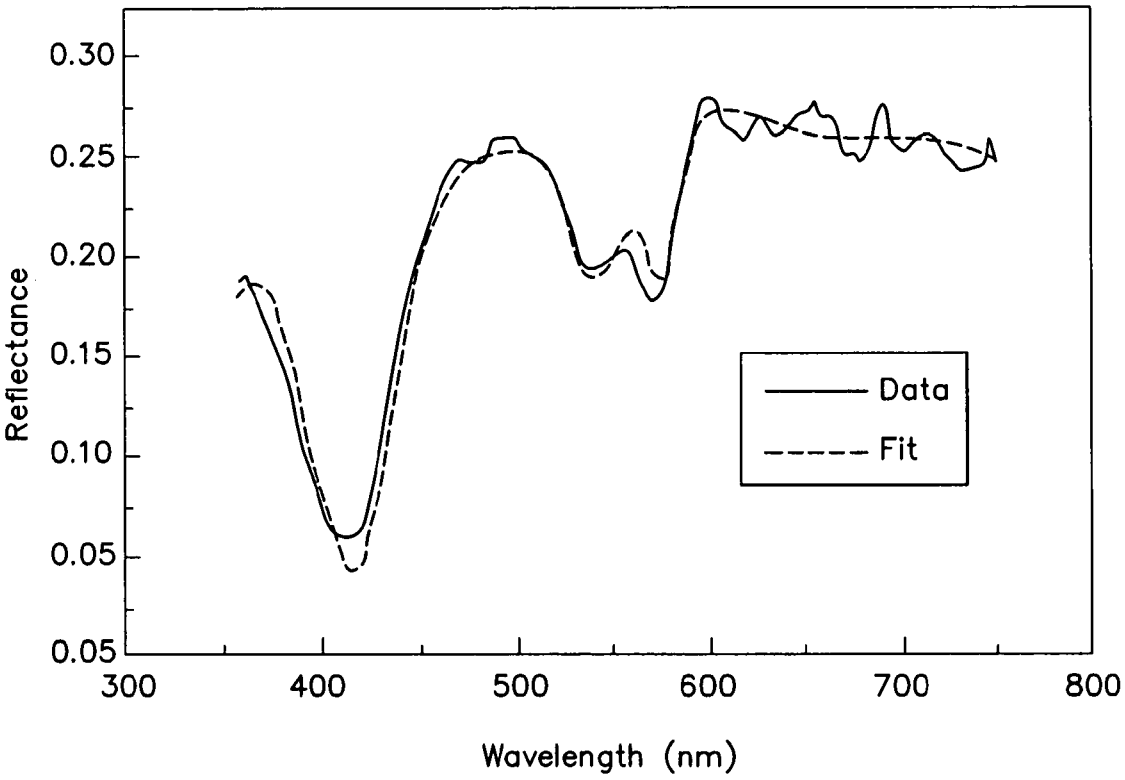
0.30
0.25
0.20
0.15
0.10
0.05
0.05
Reflectance
300
400
500
600
700
800
Wavelength (nm)
Data
Fit

FIG. 3

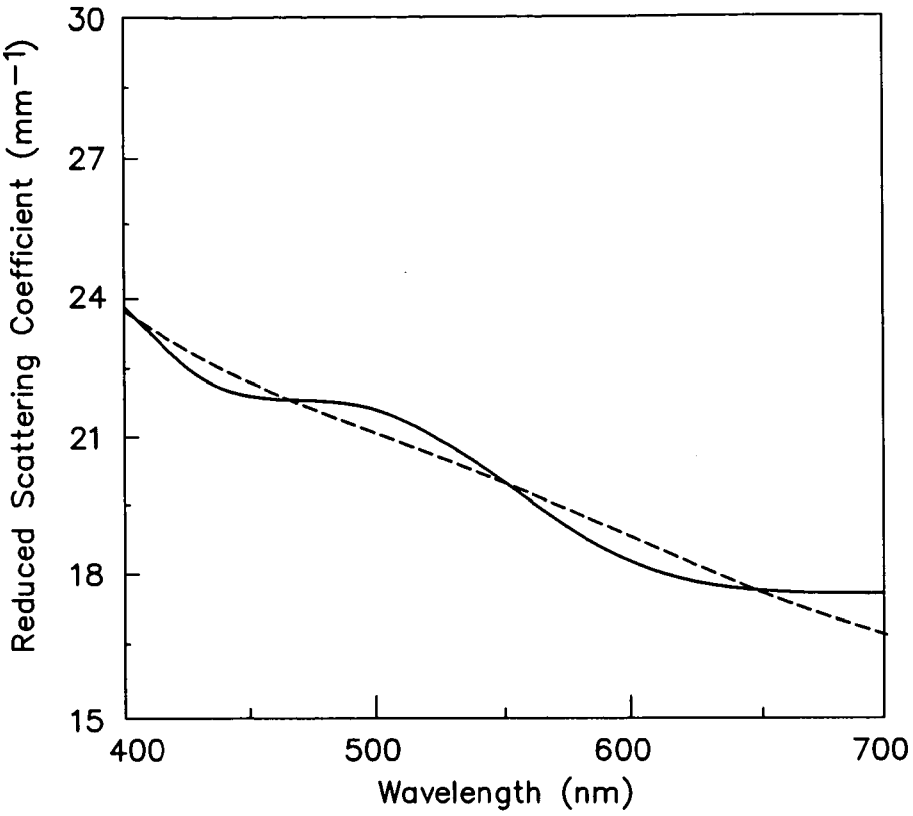
30
27
24
21
18
15
Reduced Scattering Coefficient (mm−1)
400
500
600
700
Wavelength (nm)

FIG. 4A

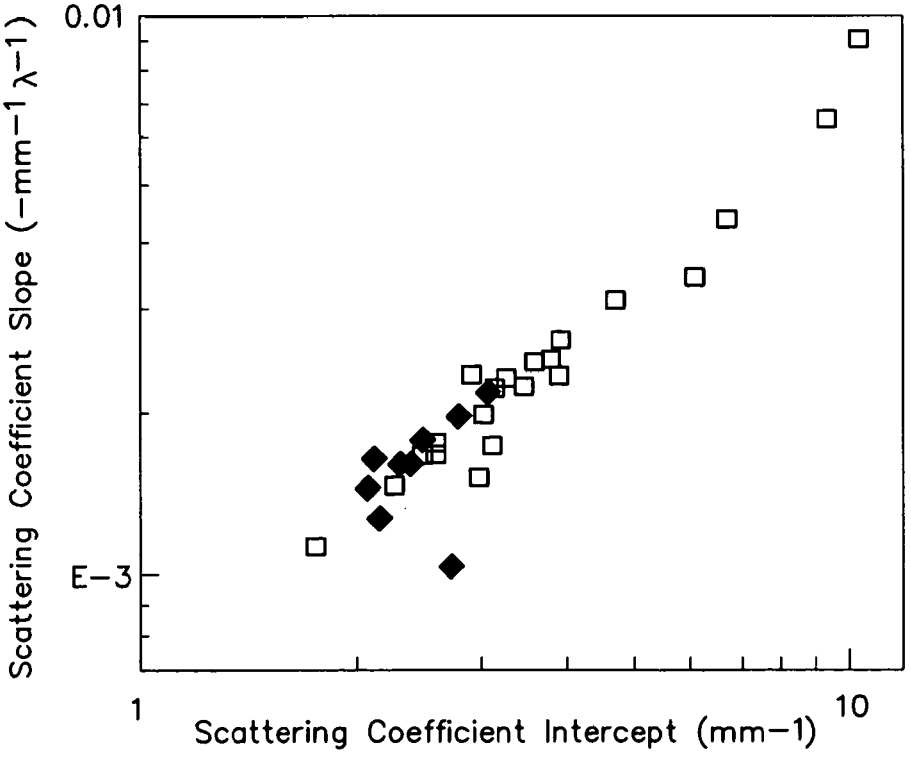
0.01
E−3
Scattering Coefficient Slope (−mm−1 λ−1)
1
10
Scattering Coefficient Intercept (mm−1)

FIG. 4B

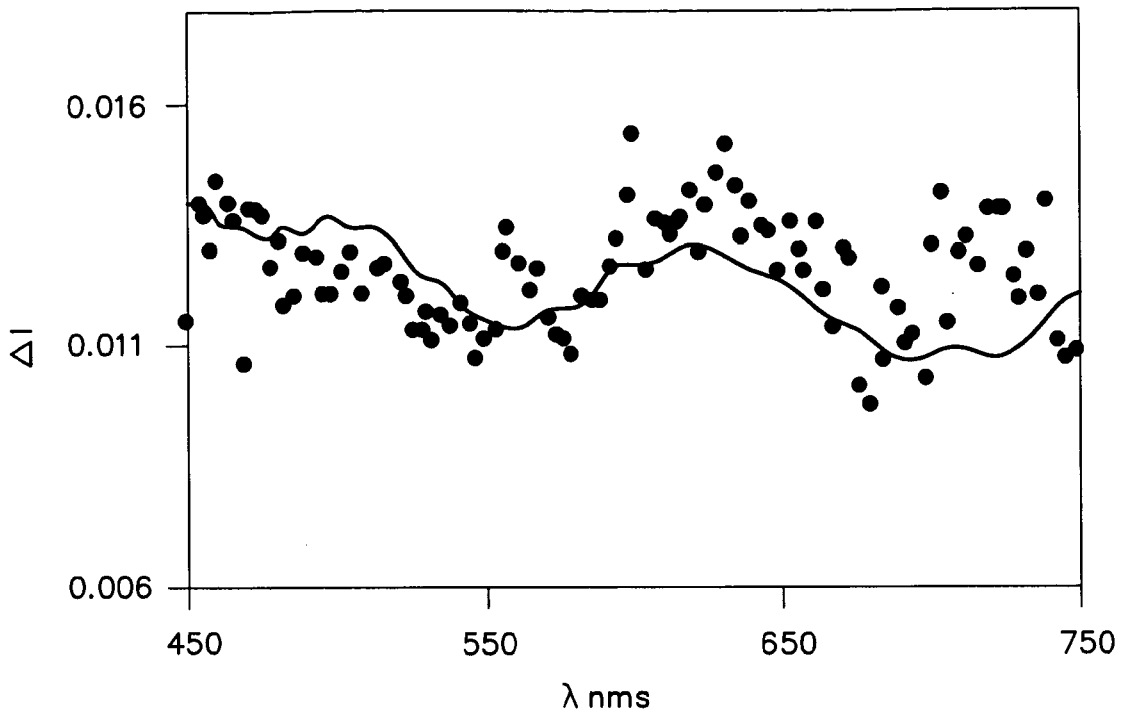
0.016
0.011
0.006
ΔI
450
550
650
750
λ nms

FIG. 5A

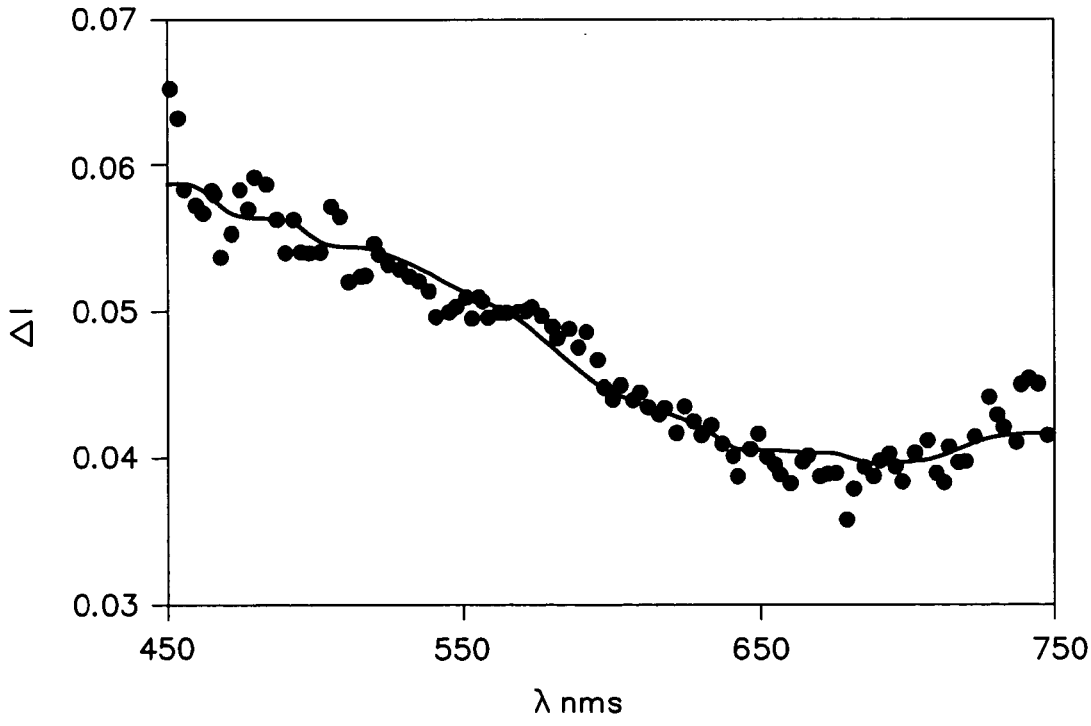
0.07
0.06
0.05
0.04
0.03
ΔI
450
550
650
750
λ nms

FIG. 5B

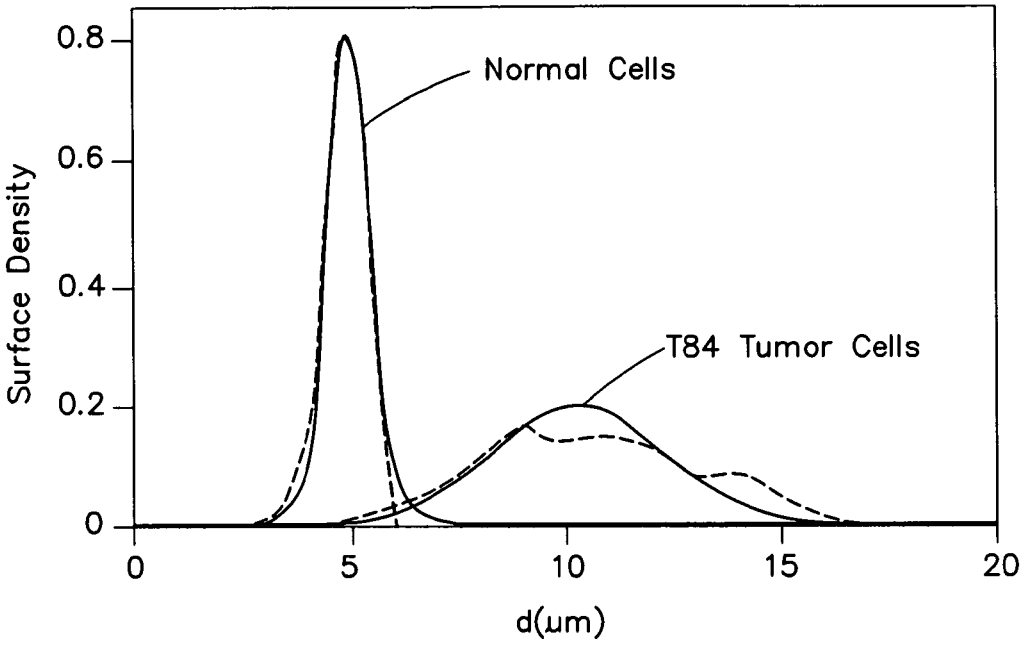
0.8
0.6
0.4
0.2
0
Surface Density
Normal Cells
T84 Tumor Cells
0
5
10
15
20
d(μm)

FIG. 5C

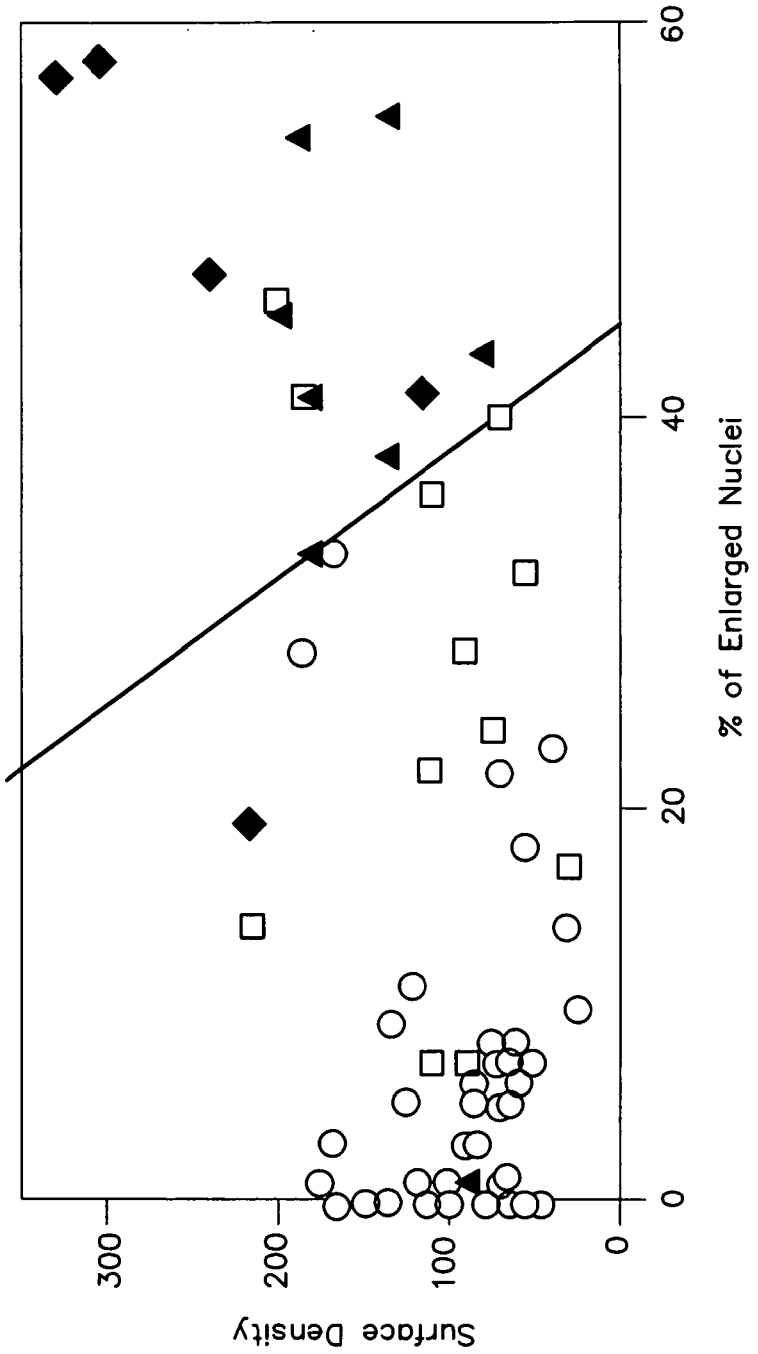

FIG. 6

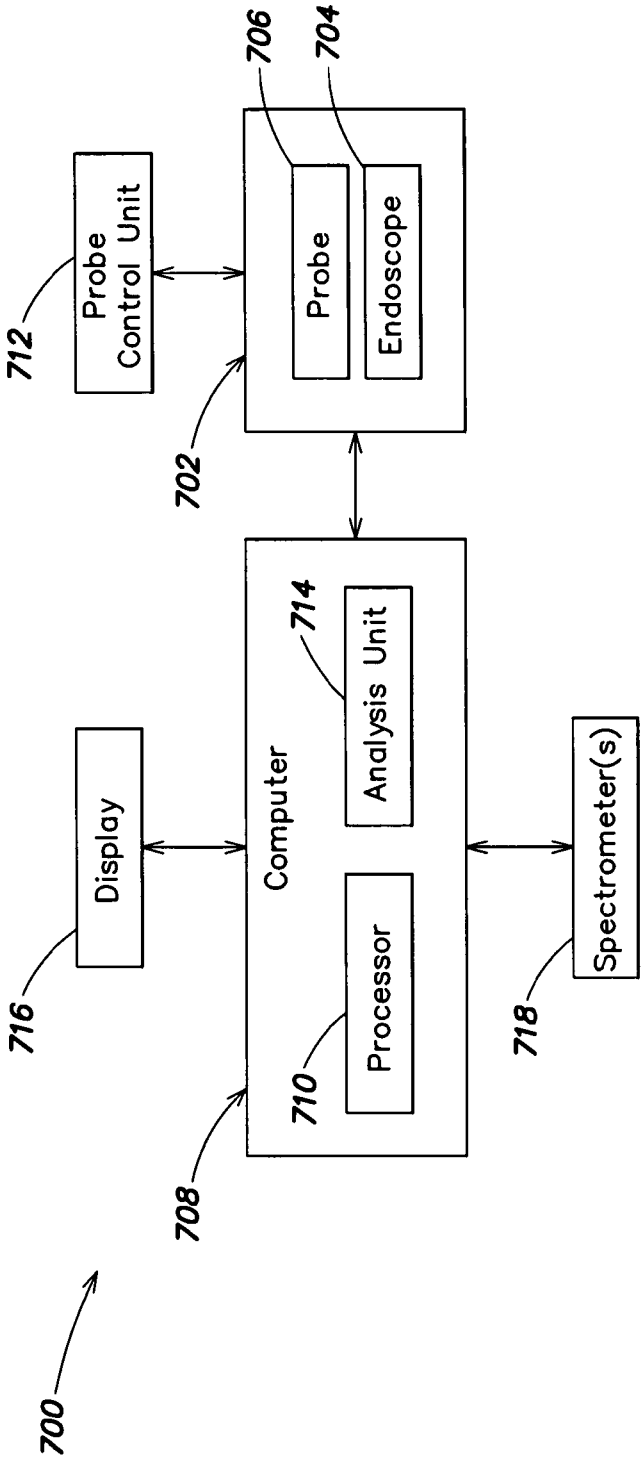
706
704
Probe
Endoscope
Probe Control Unit
712
702
714
Analysis Unit
Computer
Display
Processor
Spectrometer(s)
716
710
718
708
700

FIG. 7

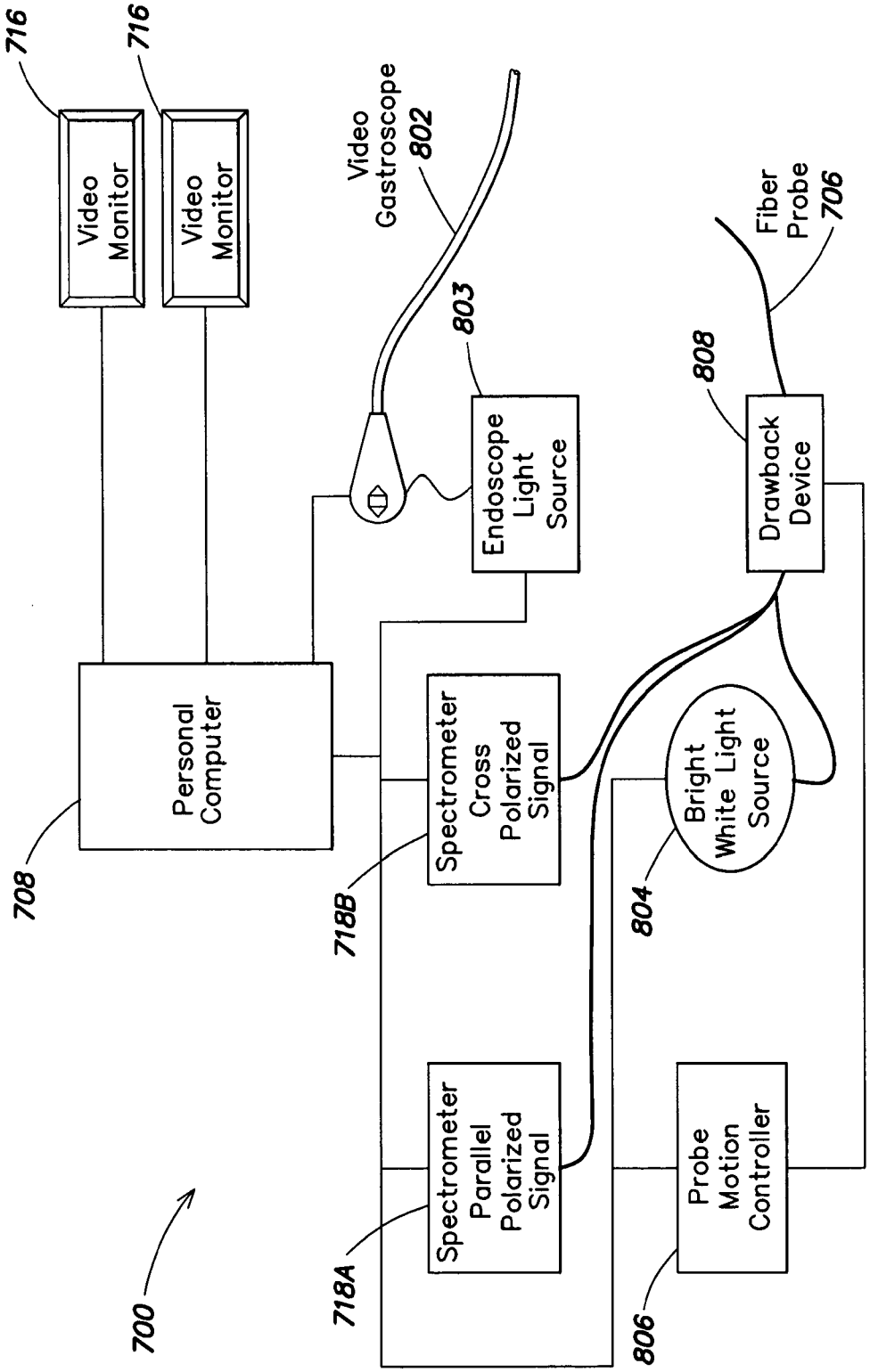
716
716
Video Monitor
Video Monitor
Video Gastroscope
802
803
Endoscope Light Source
Fiber Probe
706
808
Drawback Device
Personal Computer
708
Spectrometer Cross Polarized Signal
718B
Bright White Light Source
804
Spectrometer Parallel Polarized Signal
718A
Probe Motion Controller
806
700

FIG. 8

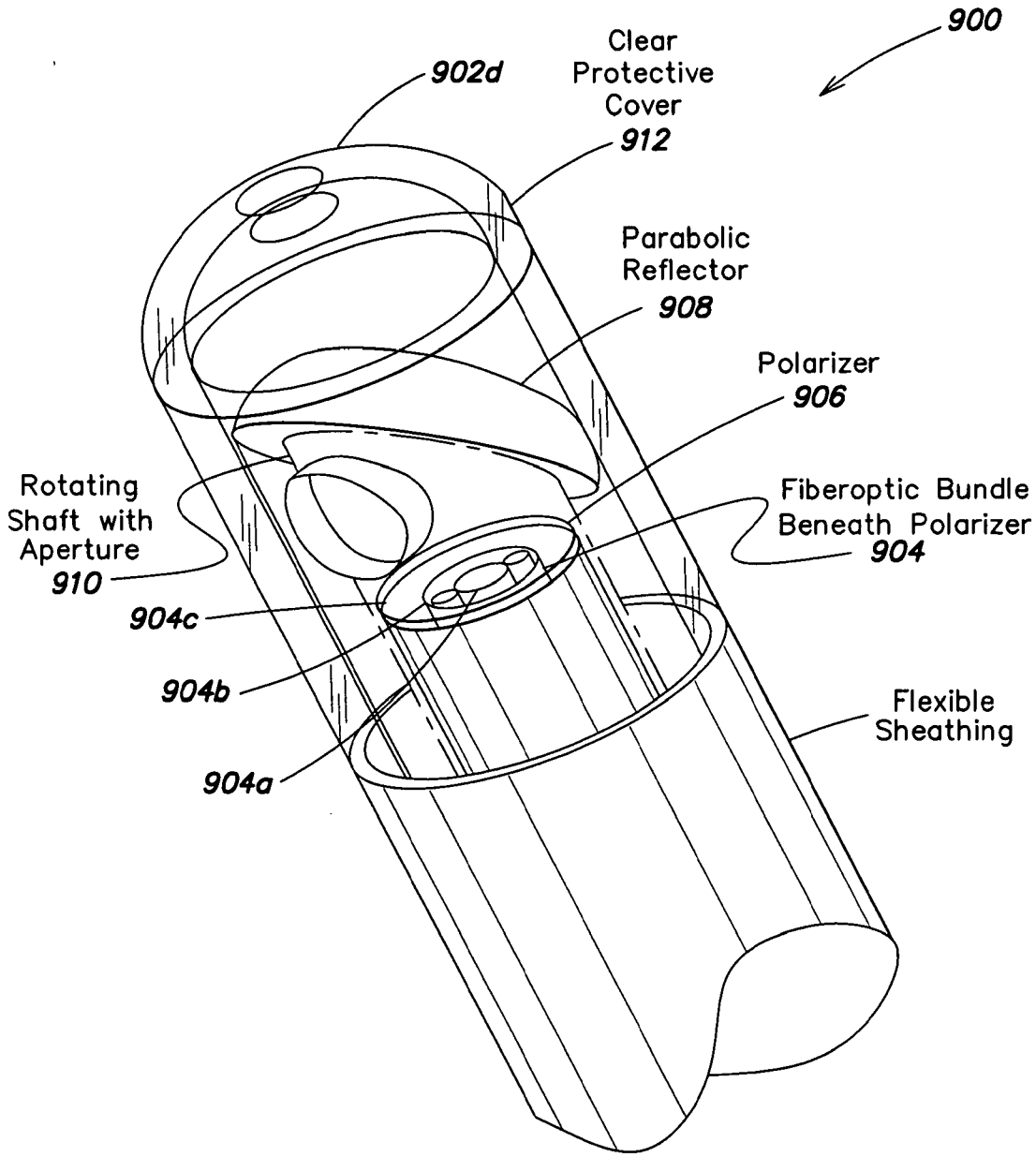
900
902d
Clear
Protective
Cover
912
Parabolic
Reflector
908
Polarizer
906
Rotating
Shaft with
Aperture
910
Fiberoptic Bundle
Beneath Polarizer
904
904c
904b
904a
Flexible
Sheathing

FIG. 9

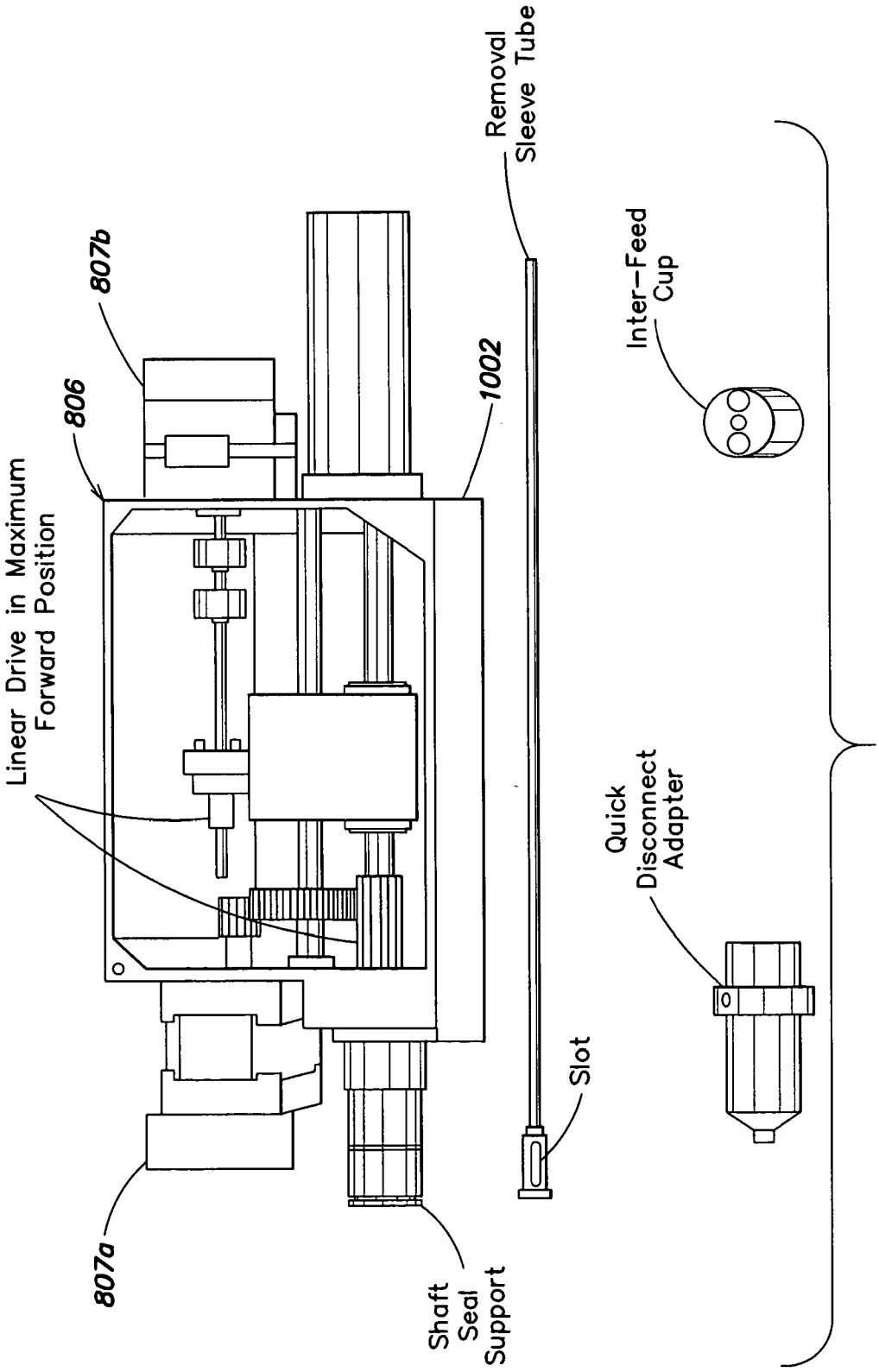
Removal Sleeve Tube
807b
806
1002
Inter-Feed Cup
Linear Drive in Maximum Forward Position
Quick Disconnect Adapter
Slot
807a
Shaft Seal Support

FIG. 10

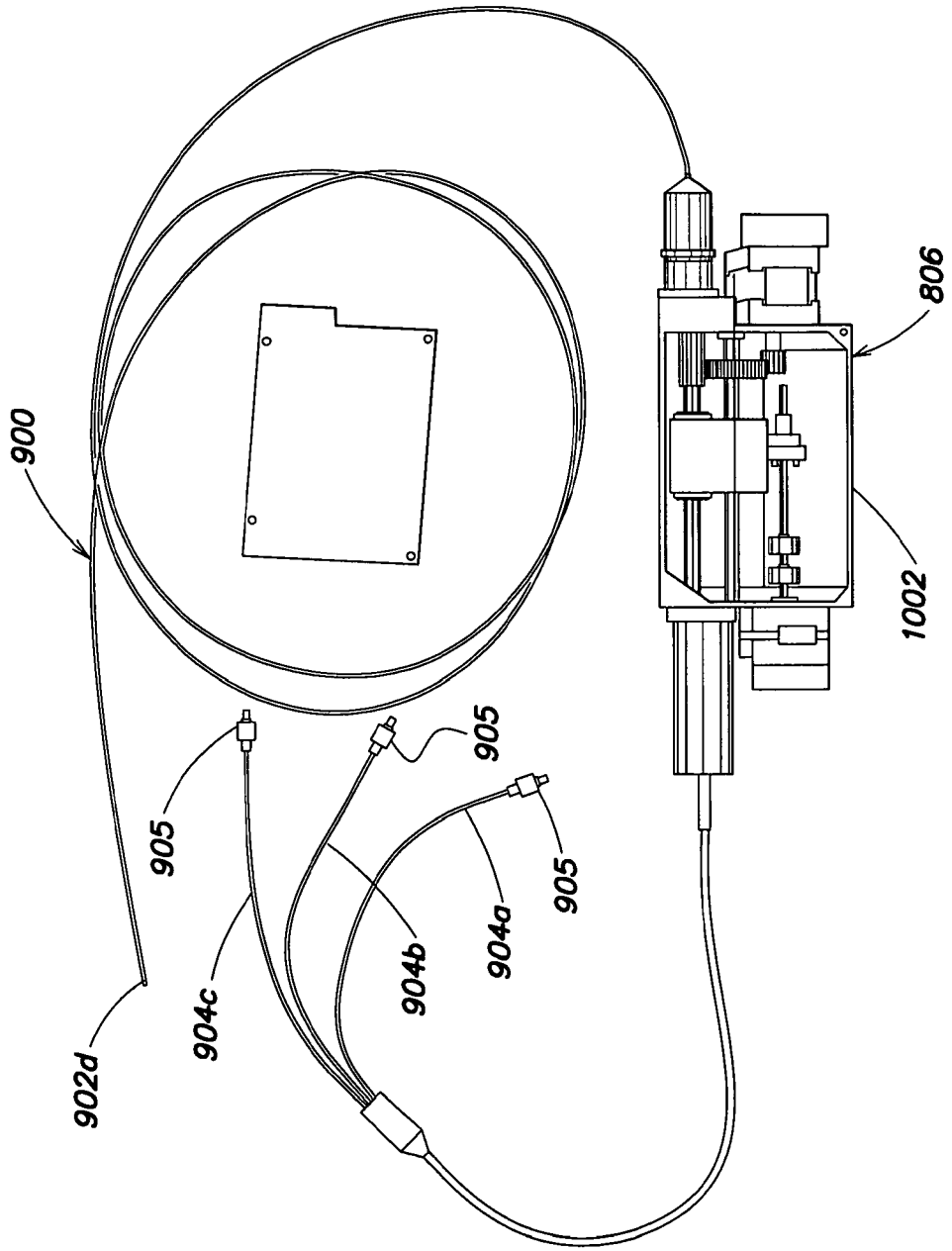

FIG. 11

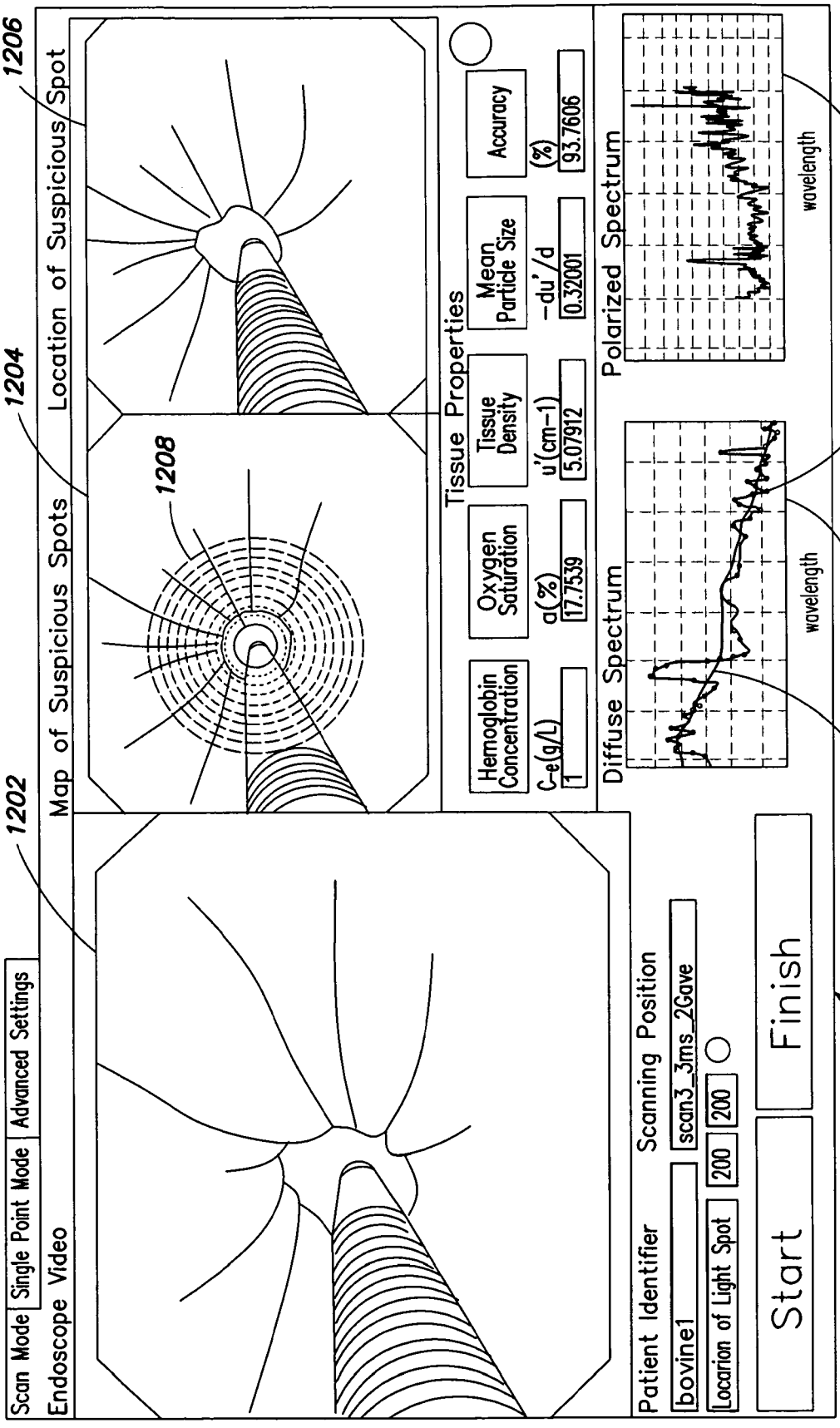
Scan Mode
Single Point Mode
Advanced Settings
Endoscope Video
Map of Suspicious Spots
Location of Suspicious Spot
Tissue Properties
Hemoglobin Concentration
C-e(g/L)
1
Oxygen Saturation
a(%)
17.7539
Tissue Density
u'(cm-1)
5.07912
Mean Particle Size
-du'/d
0.32001
Accuracy
(%)
93.7606
Diffuse Spectrum
wavelength
Polarized Spectrum
wavelength
Patient Identifier
bovine1
Scanning Position
scan3_3ms_2Gave
Locarion of Light Spot
200
200
Start
Finish
1200
1202
1204
1206
1208
1214
1215
1216
1218

FIG. 12

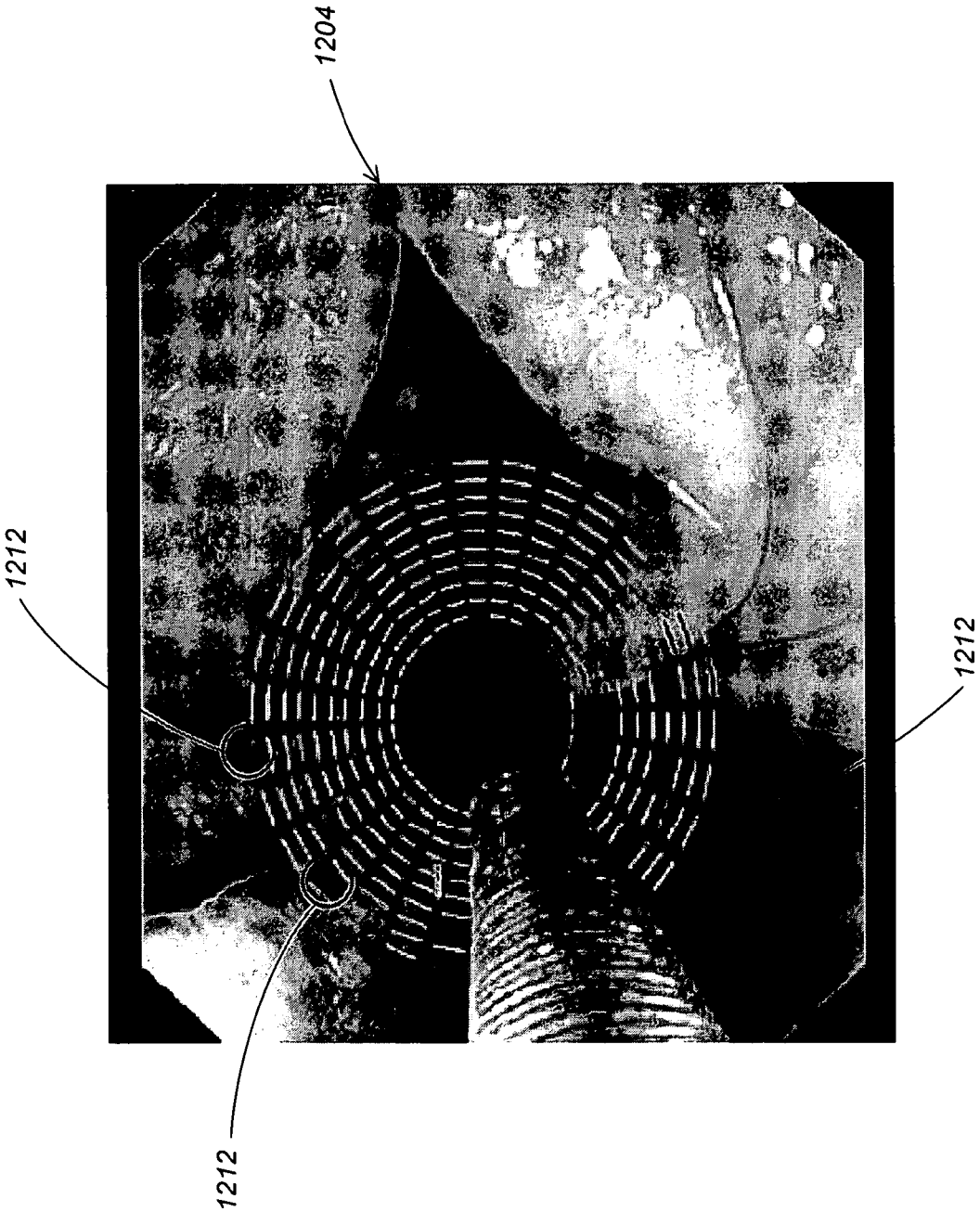

FIG. 13

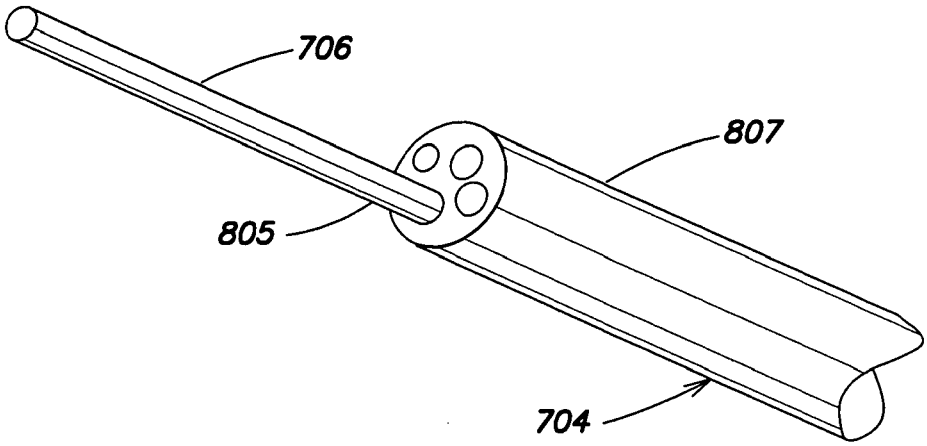

FIG. 14A

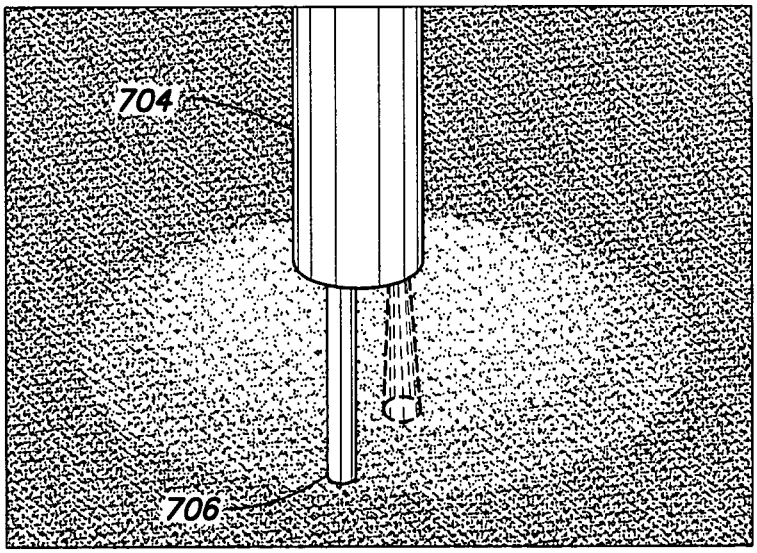

FIG. 14B

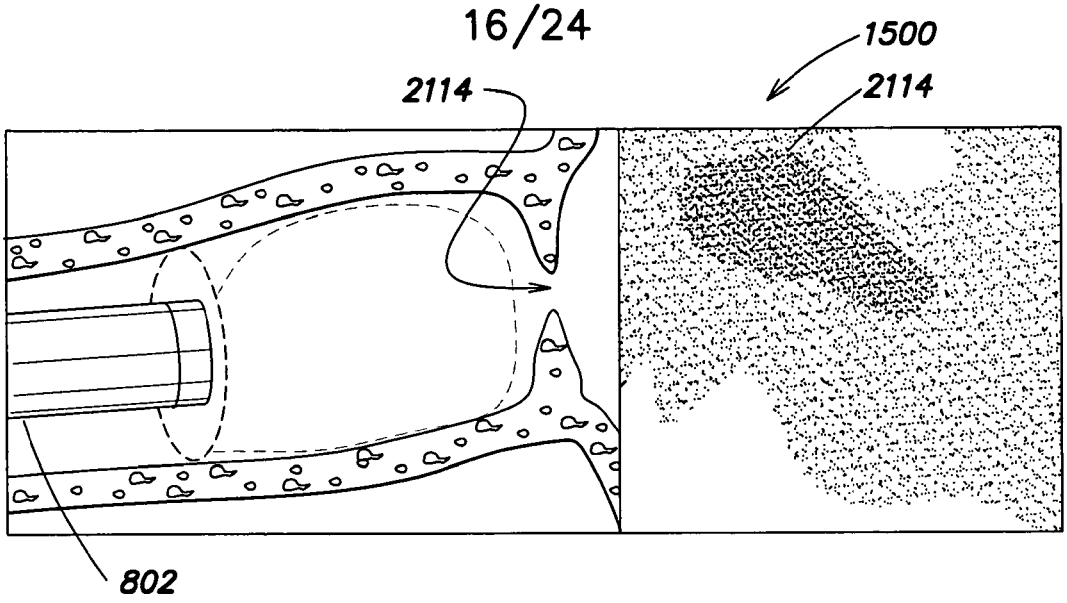

FIG. 15A

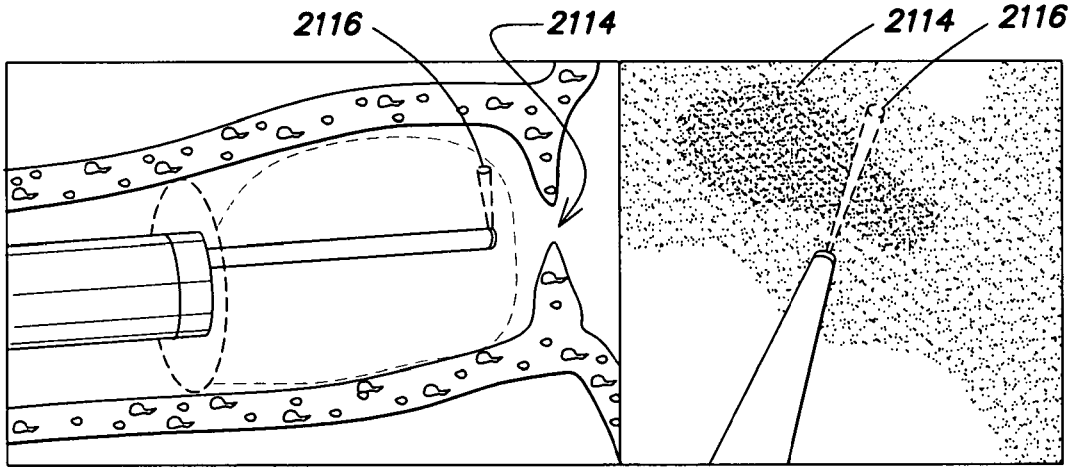

FIG. 15B

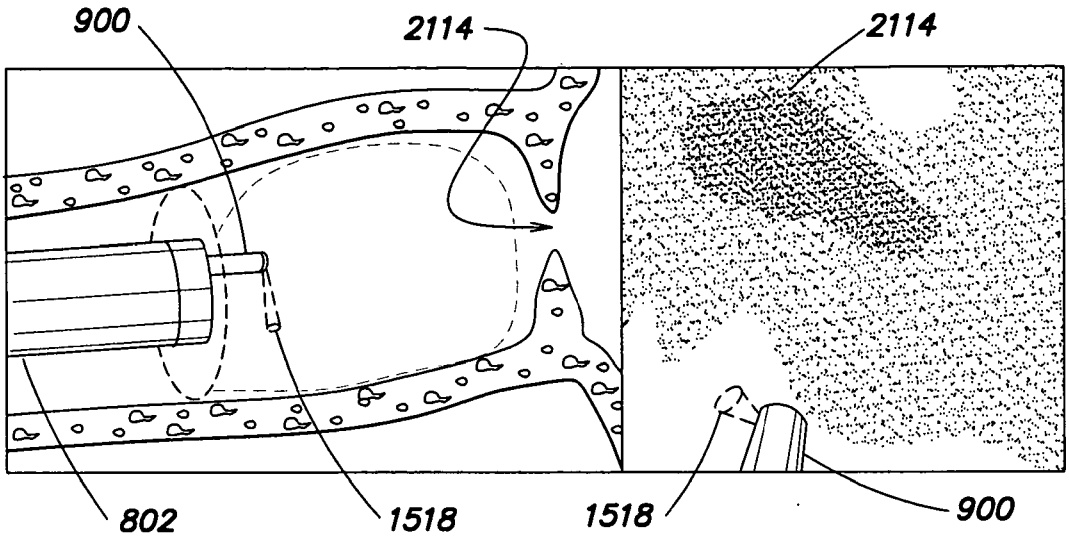

FIG. 15C

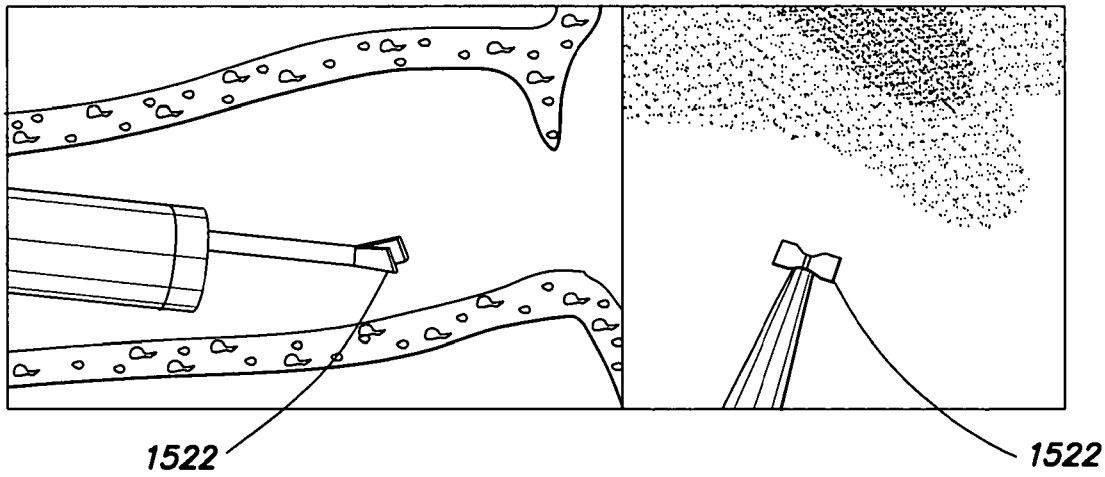

FIG. 15D

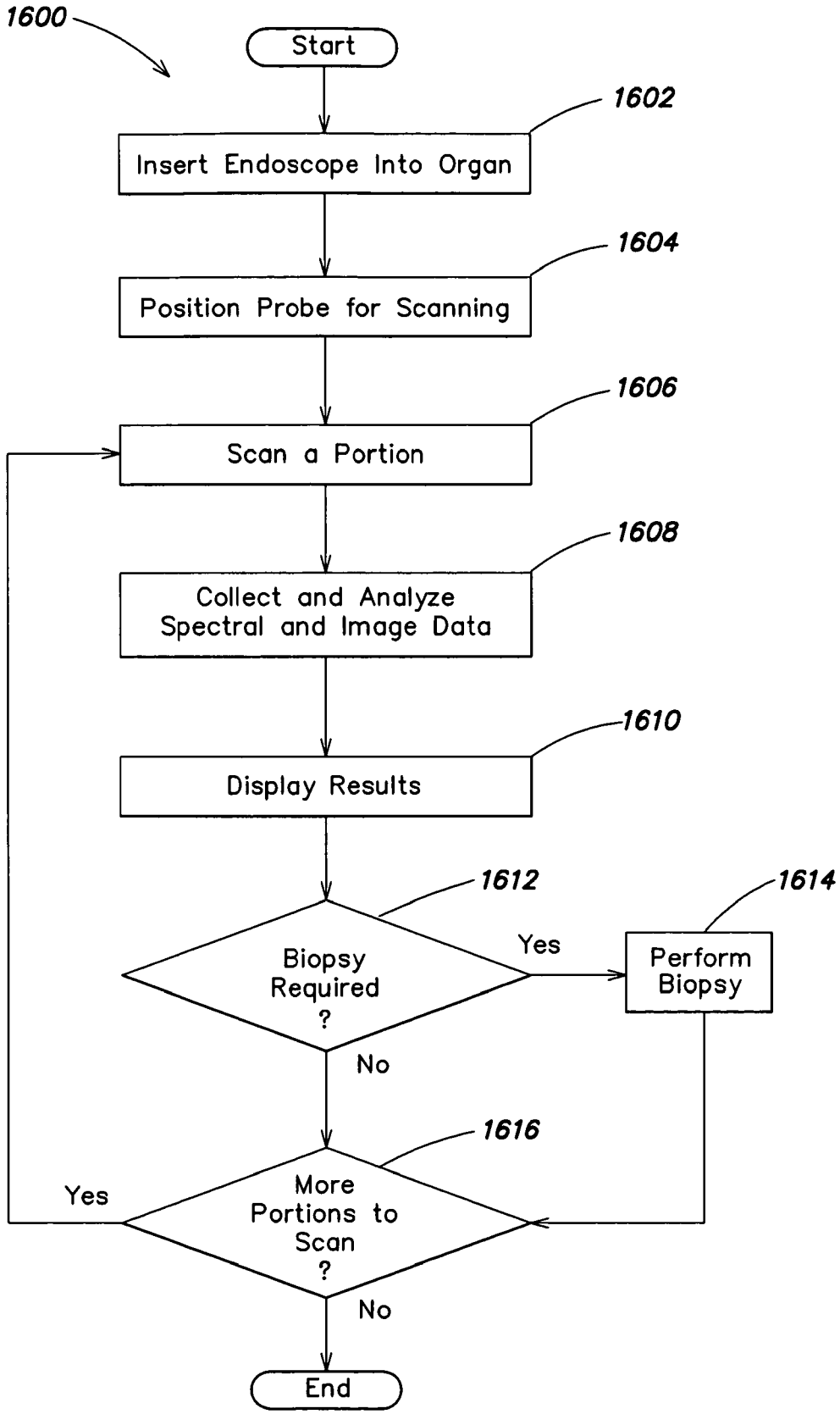
1600
Start
1602
Insert Endoscope Into Organ
1604
Position Probe for Scanning
1606
Scan a Portion
1608
Collect and Analyze Spectral and Image Data
1610
Display Results
1612
Biopsy Required ?
Yes
1614
Perform Biopsy
No
1616
More Portions to Scan ?
Yes
No
End

FIG. 16

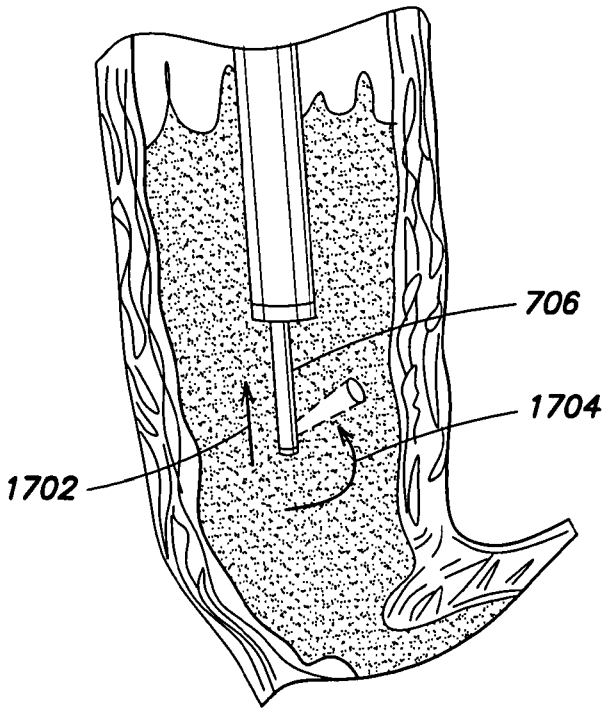

FIG. 17A

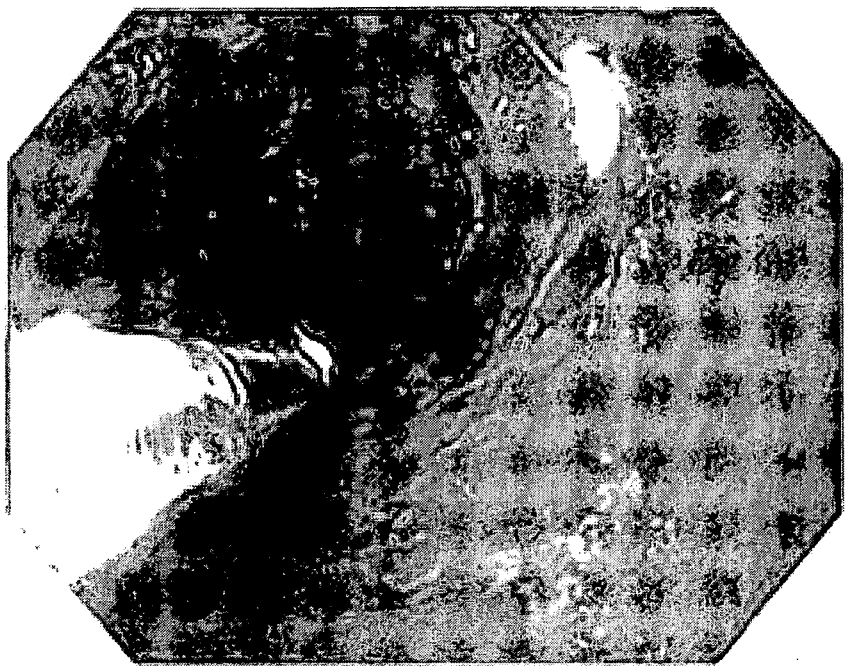

FIG. 17B

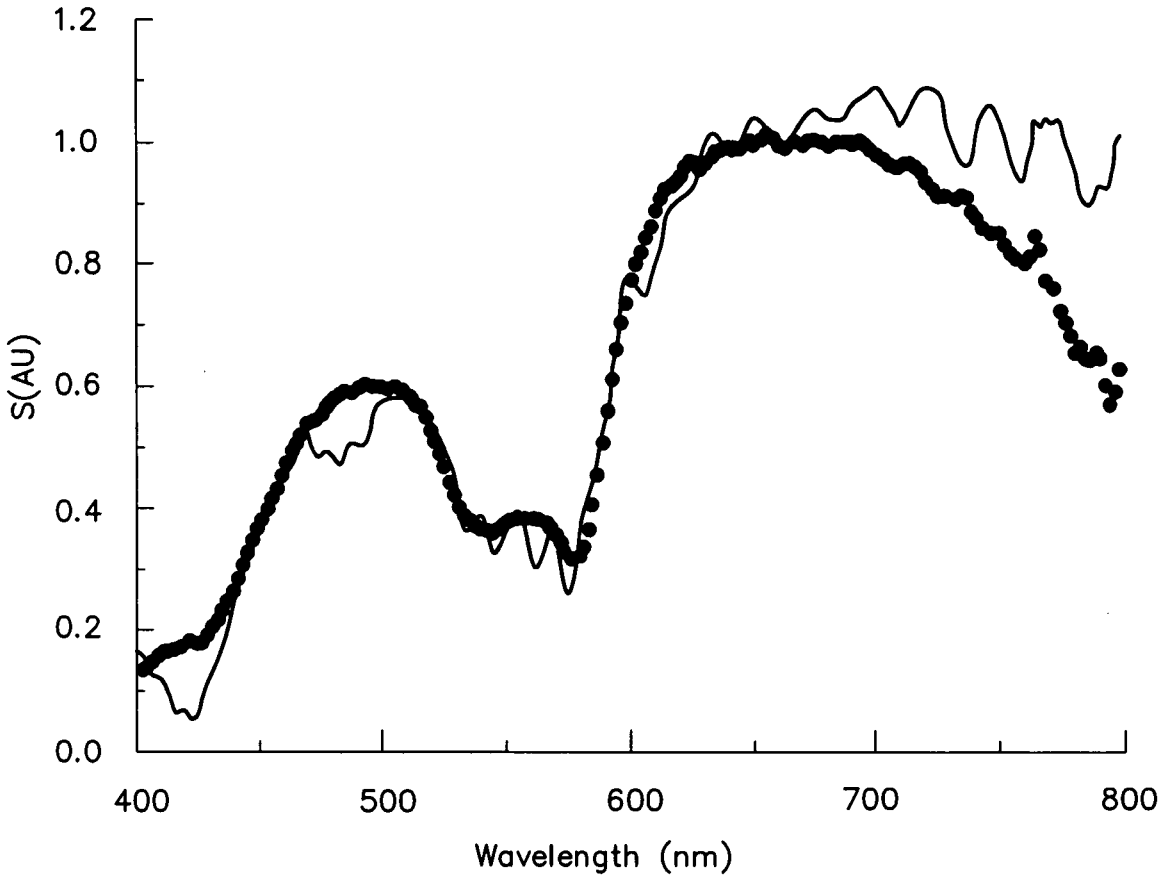

FIG. 18A

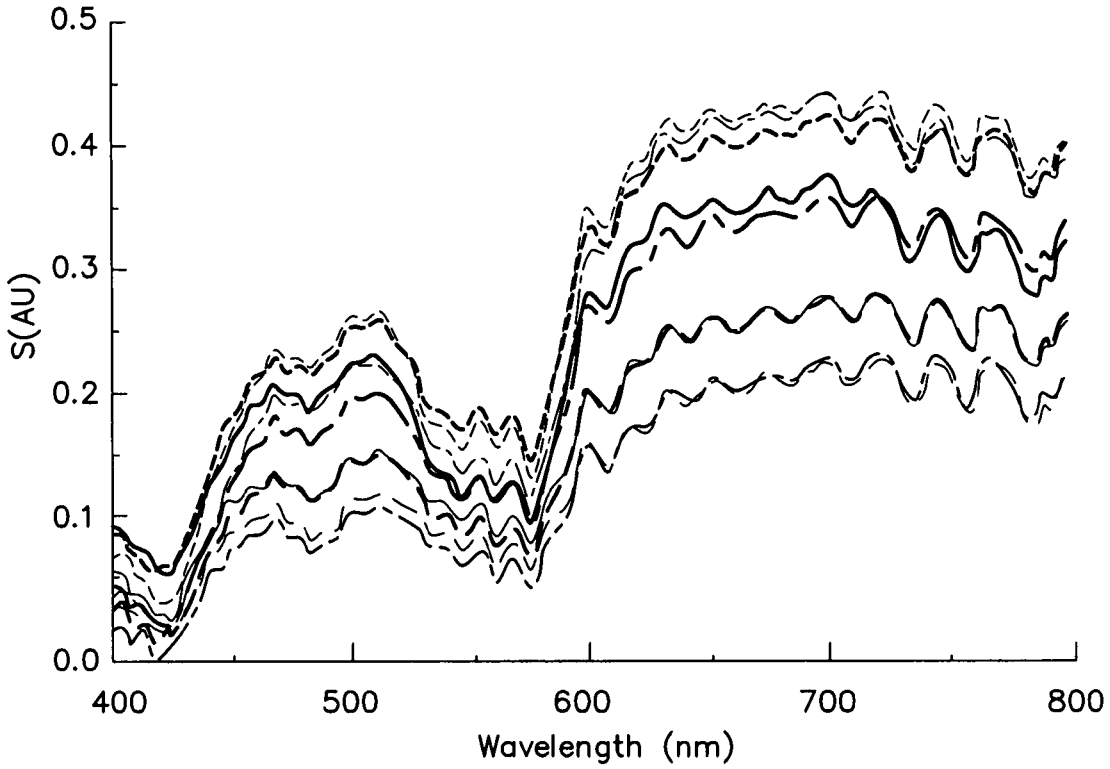

FIG. 18B

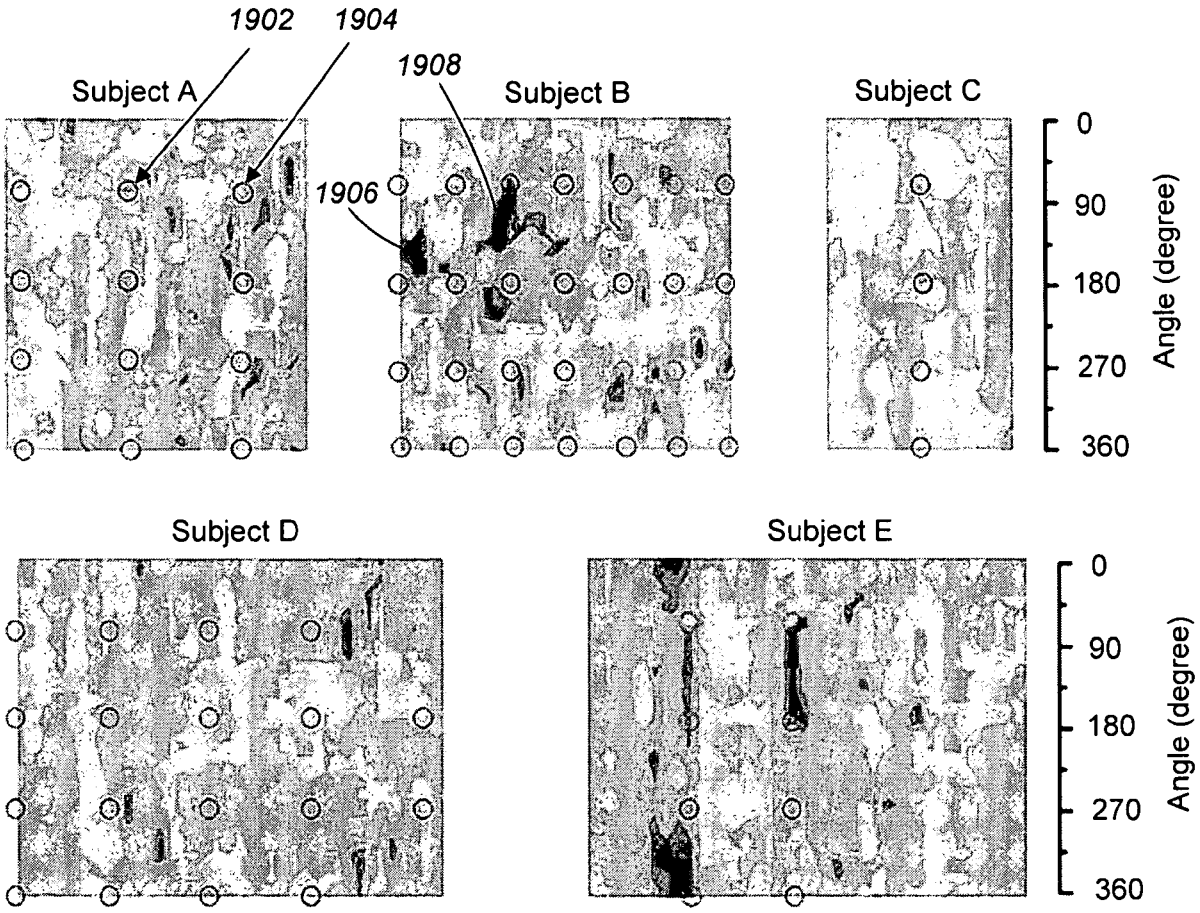

FIG. 19A

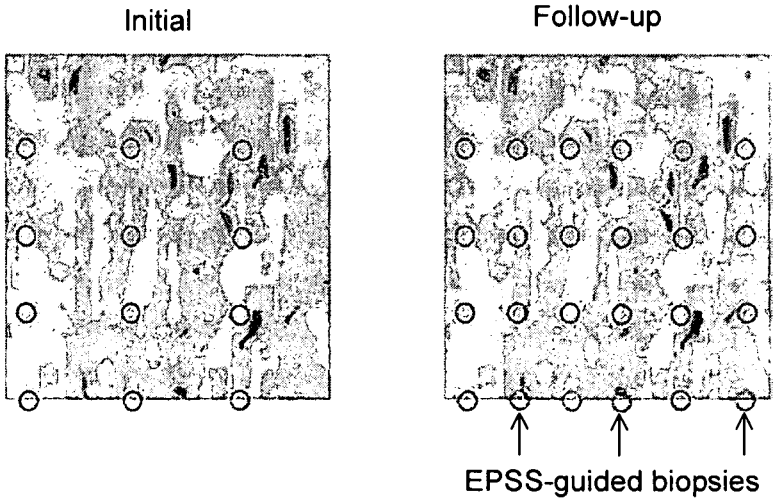

FIG. 19B

FIG. 20

INTERNATIONAL SEARCH REPORT

International application No
PCT/US2010/000166

A. CLASSIFICATION OF SUBJECT MATTER
INV. A61B5/00
ADD.

According to International Patent Classification (IPC) or to both national classification and IPC

B. FIELDS SEARCHED

Minimum documentation searched (classification system followed by classification symbols)
A61B

Documentation searched other than minimum documentation to the extent that such documents are included in the fields searched

Electronic data base consulted during the international search (name of data base and, where practical, search terms used)
EPO-Internal, INSPEC, WPI Data

C. DOCUMENTS CONSIDERED TO BE RELEVANT

Category*	Citation of document, with indication, where appropriate, of the relevant passages	Relevant to claim No.
X Y	WO 03/059150 A2 (NEOGUIDE SYSTEMS INC [US]; BELSON AMIR [US]) 24 July 2003 (2003-07-24) the whole document	1,2, 4-13, 18-21 3,14-17, 33-36
Y	WO 00/42912 A1 (MASSACHUSETTS INST TECHNOLOGY [US]; BACKMAN VADIM [US]; DASARI RAMANCH) 27 July 2000 (2000-07-27) the whole document	3,14-17, 33-36
X	US 2008/267472 A1 (DEMOS STAVROS G [US]) 30 October 2008 (2008-10-30) the whole document	1,2, 4-13, 18-21

-/--

[X] Further documents are listed in the continuation of Box C.

[X] See patent family annex.

* Special categories of cited documents :

"A" document defining the general state of the art which is not considered to be of particular relevance

"E" earlier document but published on or after the international filing date

"L" document which may throw doubts on priority claim(s) or which is cited to establish the publication date of another citation or other special reason (as specified)

"O" document referring to an oral disclosure, use, exhibition or other means

"P" document published prior to the international filing date but later than the priority date claimed

"T" later document published after the international filing date or priority date and not in conflict with the application but cited to understand the principle or theory underlying the invention

"X" document of particular relevance; the claimed invention cannot be considered novel or cannot be considered to involve an inventive step when the document is taken alone

"Y" document of particular relevance; the claimed invention cannot be considered to involve an inventive step when the document is combined with one or more other such documents, such combination being obvious to a person skilled in the art.

"&" document member of the same patent family

Date of the actual completion of the international search	Date of mailing of the international search report
9 April 2010	07/05/2010

Name and mailing address of the ISA/	Authorized officer
European Patent Office, P.B. 5818 Patentlaan 2 NL – 2280 HV Rijswijk Tel. (+31-70) 340-2040, Fax: (+31-70) 340-3016	Abraham, Volkhard

INTERNATIONAL SEARCH REPORT

International application No
PCT/US2010/000166

C(Continuation). DOCUMENTS CONSIDERED TO BE RELEVANT

Category*	Citation of document, with indication, where appropriate, of the relevant passages	Relevant to claim No.
A	US 6 485 413 B1 (BOPPART STEPHEN A [US] ET AL) 26 November 2002 (2002-11-26) column 2, line 29 - column 3, paragraph 27 figures 1-28	1,33,36
A	US 2007/274650 A1 (TEARNEY GUILLERMO J [US] ET AL TEARNEY GUILLERMO J [US] ET AL) 29 November 2007 (2007-11-29) paragraph [0016] - paragraph [0020] figures 1-29	1,33,36

INTERNATIONAL SEARCH REPORT

International application No.
PCT/US2010/000166

Box No. II Observations where certain claims were found unsearchable (Continuation of item 2 of first sheet)

This international search report has not been established in respect of certain claims under Article 17(2)(a) for the following reasons:

1. [X] Claims Nos.: 22-32
because they relate to subject matter not required to be searched by this Authority, namely:

Rule 39.1(iv) PCT - Method for treatment of the human or animal body by surgery

2. [ ] Claims Nos.:
because they relate to parts of the international application that do not comply with the prescribed requirements to such an extent that no meaningful international search can be carried out, specifically:

3. [ ] Claims Nos.:
because they are dependent claims and are not drafted in accordance with the second and third sentences of Rule 6.4(a).

Box No. III Observations where unity of invention is lacking (Continuation of item 3 of first sheet)

This International Searching Authority found multiple inventions in this international application, as follows:

1. [ ] As all required additional search fees were timely paid by the applicant, this international search report covers all searchable claims.

2. [ ] As all searchable claims could be searched without effort justifying an additional fees, this Authority did not invite payment of additional fees.

3. [ ] As only some of the required additional search fees were timely paid by the applicant, this international search report covers only those claims for which fees were paid, specifically claims Nos.:

4. [ ] No required additional search fees were timely paid by the applicant. Consequently, this international search report is restricted to the invention first mentioned in the claims; it is covered by claims Nos.:

Remark on Protest

[ ] The additional search fees were accompanied by the applicant's protest and, where applicable, the payment of a protest fee.

[ ] The additional search fees were accompanied by the applicant's protest but the applicable protest fee was not paid within the time limit specified in the invitation.

[ ] No protest accompanied the payment of additional search fees.

INTERNATIONAL SEARCH REPORT

Information on patent family members

International application No
PCT/US2010/000166

Patent document cited in search report	Publication date	Patent family member(s)	Publication date
WO 03059150 A2	24-07-2003	AU 2002360767 A1	30-07-2003
		CA 2472197 A1	24-07-2003
		CN 1617687 A	18-05-2005
		EP 1469777 A2	27-10-2004
		JP 2005514144 T	19-05-2005
		US 2003167007 A1	04-09-2003
WO 0042912 A1	27-07-2000	AU 3351000 A	07-08-2000
		CA 2359643 A1	27-07-2000
		CN 1341004 A	20-03-2002
		EP 1148811 A1	31-10-2001
		JP 2002535027 T	22-10-2002
		NZ 513116 A	31-10-2003
		US 2002171831 A1	21-11-2002
		US 6404497 B1	11-06-2002
US 2008267472 A1	30-10-2008	WO 2009009414 A2	15-01-2009
US 6485413 B1	26-11-2002	NONE	
US 2007274650 A1	29-11-2007	EP 1986562 A2	05-11-2008
		JP 2009537024 T	22-10-2009
		WO 2007149601 A2	27-12-2007

专利名称(译)	内窥镜偏振多光谱光散射扫描方法		
公开(公告)号	EP2389099A1	公开(公告)日	2011-11-30
申请号	EP2010704237	申请日	2010-01-22
[标]申请(专利权)人(译)	佩雷尔曼LEVŧ		
申请(专利权)人(译)	佩雷尔曼，LEV T.		
当前申请(专利权)人(译)	佩雷尔曼，LEV T.		
[标]发明人	PERELMAN LEV T		
发明人	PERELMAN, LEV T.		
IPC分类号	A61B5/00		
CPC分类号	A61B5/0062 A61B5/0066 A61B5/0071 A61B5/0075 A61B5/0084		
优先权	61/147074 2009-01-23 US		
外部链接	Espacenet		

摘要(译)

用于早期检测各种器官组织中癌前病变和其他异常变化的方法和系统。该系统包括内窥镜扫描与光散射光谱学的组合，并且改进了可能以其他方式未被检测到的异常的检测。该系统可以包括探针，该探针收集与探针距扫描组织的距离无关的质量数据。在内窥镜检查期间，使用偏振多光谱光散射扫描对器官的组织进行成像，并且以允许检测组织中的异常形态和生物化学变化的方式将结果呈现给用户。可以在进行内窥镜检查时进行是否进行活组织检查的确定，从而提供引导的活组织检查。可以快速扫描器官的整个表面，并以减少的时间延迟分析扫描结果。